

Microscopic Black Holes and Cosmic Shells

A THESIS
SUBMITTED TO THE FACULTY OF THE GRADUATE SCHOOL
OF THE UNIVERSITY OF MINNESOTA
BY

Ramin G. Daghigh

IN PARTIAL FULFILLMENT OF THE REQUIREMENTS
FOR THE DEGREE OF
DOCTOR OF PHILOSOPHY

March, 2022

© Ramin G. Daghigh 2022
ALL RIGHTS RESERVED

Microscopic Black Holes and Cosmic Shells

by Ramin G. Daghigh

Under the supervision of J. I. Kapusta

ABSTRACT

In the first part of this thesis the relativistic viscous fluid equations describing the outflow of high temperature matter created via Hawking radiation from microscopic black holes are solved numerically for a realistic equation of state. We focus on black holes with initial temperatures greater than 100 GeV and lifetimes less than 6 days. The spectra of direct photons and photons from π^0 decay are calculated for energies greater than 1 GeV. We calculate the diffuse gamma ray spectrum from black holes distributed in our galactic halo. However, the most promising route for their observation is to search for point sources emitting gamma rays of ever-increasing energy. We also calculate the spectra of all three flavors of neutrinos arising from direct emission from the fluid at the neutrino-sphere and from the decay of pions and muons from their decoupling at much larger radii and smaller temperatures for neutrino energies between 1 GeV and the Planck energy. The results for neutrino spectra may be applicable for the last few hours and minutes of the lifetime of a microscopic black hole. In the second part of this thesis the combined field equations of gravity and a scalar field are studied. When a potential for a scalar field has two local minima there arise spherical shell-type solutions of the classical field equations due to gravitational attraction. We establish such solutions numerically in a space which is asymptotically de Sitter. It generically arises when the energy scale characterizing the scalar field potential is much less than the Planck scale. It is shown that the mirror image of the shell appears in the other half of the Penrose diagram. The configuration is smooth everywhere with no physical singularity.

Acknowledgements

I would like to express my deep appreciation to Joseph Kapusta for his guidance and insight throughout this research. With his kindness and patience, he surpassed the role of adviser. He is and will be a role model and a mentor throughout my life. I would also like to express my deep appreciation to Yutaka Hosotani for his contributions in this thesis. Finally, I would like to thank my wife, Paula, for her patience during the years of graduate school.

Dedication

To Paula, Nader, Eghbaleh and Hamoon.

Table of Contents

| | |
|--|------------|
| Abstract | i |
| Acknowledgements | ii |
| Dedication | iii |
| List of Figures | vi |
| 1 Introduction | 1 |
| 1.1 Microscopic Black Holes | 3 |
| 1.2 Cosmic Shells | 6 |
| 2 High Temperature Matter and Particle Spectra from Microscopic Black Holes | 9 |
| 2.1 Hawking Radiation | 9 |
| 2.2 Relativistic Viscous Fluid Equations | 11 |
| 2.3 Equation of State and Transport Coefficients | 13 |
| 2.4 Numerical Solution and Scaling | 16 |
| 2.5 Onset of Free-Streaming | 23 |
| 2.6 Photon Emission | 28 |
| 2.6.1 Direct photons | 28 |
| 2.6.2 π^0 decay photons | 29 |
| 2.6.3 Instantaneous and integrated photon spectra | 30 |

| | | |
|----------|--|-----------|
| 2.7 | Observability of Gamma Rays | 32 |
| 2.7.1 | Diffuse spectra from the galactic halo | 32 |
| 2.7.2 | Point source systematics | 35 |
| 2.8 | Neutrino Emission | 38 |
| 2.8.1 | Directly Emitted Neutrinos | 39 |
| 2.8.2 | Neutrinos from Pion Decay | 43 |
| 2.8.3 | Neutrinos from Muon Decay | 44 |
| 2.9 | Comparison of Neutrino Sources | 47 |
| 2.10 | Observability of the Neutrino Flux | 53 |
| 3 | Cosmic Shells | 56 |
| 3.1 | Shell Solutions in Static Coordinates | 56 |
| 3.2 | Numerical Analysis of the Nonlinear Regime | 66 |
| 3.3 | Global Structure of the Space-Time and Solutions | 70 |
| 3.4 | False Vacuum Decay | 78 |
| 4 | Summary | 80 |
| | Appendix A. Numerical Calculations | 84 |
| | References | 88 |

List of Figures

| | | |
|-----|---|----|
| 2.1 | Entropy density as a function of temperature, excluding neutrinos and gravitons. It is assumed that the QCD phase transition is first order and the EW phase transition is second order. | 14 |
| 2.2 | The value of $u = v\gamma$ at one-tenth the Schwarzschild radius as determined by numerical solution. The physical applicability of the numerical solution begins at radii greater than r_S | 18 |
| 2.3 | The radial dependence of u for three different Hawking temperatures. The curves begin at $r_S/10$ and terminate when the local temperature reaches 10 MeV. | 19 |
| 2.4 | The radial dependence of T for three different Hawking temperatures. The curves begin at $r_S/10$ and terminate when the local temperature reaches 10 MeV. | 20 |
| 2.5 | The radial dependence of s for three different Hawking temperatures. The curves begin at $r_S/10$ and terminate when the local temperature reaches 10 MeV. | 21 |
| 2.6 | The radial dependence of the entropy flow for three different Hawking temperatures. The curves begin at $r_S/10$ and terminate when the local temperature reaches 10 MeV. | 22 |
| 2.7 | Free-streaming of particles at freeze-out surface. | 23 |
| 2.8 | The rate for $\pi\pi$ scattering and for the bremsstrahlung reaction $ee \rightarrow ee\gamma$ are compared to the local volume expansion rate. The Hawking temperature is 10 TeV. | 24 |

| | | |
|------|--|----|
| 2.9 | The freeze-out or free-streaming radius as a function of the Schwarzschild radius for three different freeze-out temperatures. | 27 |
| 2.10 | The instantaneous gamma ray spectrum for three different Hawking temperatures assuming $T_f = 140$ MeV. | 31 |
| 2.11 | Same as figure 9 but with $T_f = 100$ MeV. | 32 |
| 2.12 | The time-integrated gamma ray spectrum starting from the indicated Hawking temperature. Here $T_f = 140$ MeV. | 33 |
| 2.13 | The flux of diffuse gamma rays coming from our galactic halo. The normalization is $\dot{\rho}_0 = 1 \text{ pc}^{-3} \text{ yr}^{-1}$. The halo is assumed to be spherically symmetric, $q = 1$; the results for a flattened halo with $q = 2$ are very similar. | 35 |
| 2.14 | The average gamma ray energy as a function of the remaining lifetime of the black hole. The times spanned correspond to approximately $400 \text{ GeV} < T_H < 200 \text{ TeV}$ | 37 |
| 2.15 | The instantaneous direct neutrino spectra emerging from the fluid with neutrino-sphere located at $T_\nu = 100$ GeV compared to the direct Hawking radiation. Also shown are neutrinos arising from pion, direct muon and indirect muon decays at a decoupling temperature of $T_f = 100$ MeV. Here the black hole temperature is $T_H = 1$ TeV. All curves are for one flavor of neutrino or anti-neutrino. | 48 |
| 2.16 | Same as figure 2.15 but with $T_H = 1$ TeV. | 49 |
| 2.17 | The instantaneous direct neutrino spectra emerging from the fluid with neutrino-sphere located at $T_\nu = 100$ GeV compared to the direct Hawking radiation. Both curves are for one flavor of neutrino or anti-neutrino. | 50 |
| 2.18 | Same as figure 2.17 but with $T_H = 110$ GeV. | 51 |
| 2.19 | Same as figure 2.17 but with $T_H = 120$ GeV. | 52 |

| | | |
|------|---|----|
| 2.20 | The time integrated neutrino spectra emerging from a microscopic black hole. Here the calculation begins when the black hole temperature is $T_0 = 1$ TeV. Either the direct Hawking radiation of neutrinos or the direct neutrino emission from a neutrino-sphere at a temperature of 100 GeV should be used. All curves are for one species of neutrino or anti-neutrino. | 53 |
| 2.21 | Same as figure 2.20 but with $T_0 = 10$ TeV. | 54 |
| 3.1 | The potential $V[\phi]$ | 57 |
| 3.2 | Schematic behavior of $\phi(r)$ | 61 |
| 3.3 | Schematic behavior of $H(r)$ | 62 |
| 3.4 | $\phi(r)$ of a solution with $f/m_{\text{P}} = 1.40 \times 10^{-3}$, $\Delta f/f = 0.002$, $\lambda = 0.01$. ϕ and r are in the units of m_{P} and l_{P} , respectively. The maximum value of ϕ is smaller than $f_2 \sim 0.0014 \cdot m_{\text{P}}$ | 64 |
| 3.5 | $H(r)$ of a solution with $f/m_{\text{P}} = 1.40 \times 10^{-3}$, $\Delta f/f = 0.002$, $\lambda = 0.01$. $H(r)$ decreases in two steps in the shell region. $H(r)$ in the de Sitter space ($= 1 - r^2/a^2$) is plotted in a dotted line. | 66 |
| 3.6 | $p(r)$ of a solution with $f/m_{\text{P}} = 1.40 \times 10^{-3}$, $\Delta f/f = 0.002$, $\lambda = 0.01$. $p(r)$ decreases in two steps, from 1 to 0.6256, in the shell region. | 67 |
| 3.7 | The energy density T_{00} for a shell solution with $f/m_{\text{P}} = 1.40 \times 10^{-3}$, $\Delta f/f = 0.002$, $\lambda = 0.01$. T_{00} and r are in the units of m_{P}^4 and l_{P} , respectively. The energy density is localized in the two shells over the de Sitter background. | 68 |
| 3.8 | The radial pressure T_{11} for a shell solution with $f/m_{\text{P}} = 1.40 \times 10^{-3}$, $\Delta f/f = 0.002$, $\lambda = 0.01$. T_{11} and r are in the units of m_{P}^4 and l_{P} , respectively. The pressure is higher and constant between the two shells. | 69 |
| 3.9 | A solution with double bounces with $f/m_{\text{P}} = 1.40 \times 10^{-3}$, $\Delta f/f = 0.002$, $\lambda = 0.01$. A solution with multiple bounces appears at a smaller shell radius than a solution with a single bounce. | 70 |

| | | |
|------|--|----|
| 3.10 | The f -dependence of the shell solutions. $\lambda = 0.01$ and $\Delta f/f = 0.002$ are fixed. R , r_H , and a are the radius of the shell, the horizon length where $H(r)$ vanishes, and the horizon length in the de Sitter space, respectively. The ratios of various pairs are plotted. Circles, squares, and diamonds correspond to data points obtained. | 71 |
| 3.11 | Penrose diagram of the de Sitter space. | 74 |
| 3.12 | Global structure of the shell solution in the conformal coordinates. The mirror image appears in the other hemisphere. | 77 |
| A.1 | $4\pi r^2 T^{0r}/L$ as a function of r/r_s for a black hole temperature of 10 TeV. The curve begins at r_s and terminates when the local temperature reaches $T = m_e$ | 87 |

Chapter 1

Introduction

Black holes can be created in the collapse of a star which was originally 10 to 20 times the mass of the sun. There is strong evidence that there are huge black holes of about 1 million solar masses near the center of galaxies. Another possibility are primordial black holes of almost arbitrarily small mass which were created in the early universe. Depending on the time of the formation of primordial black holes in the early universe, they can have a wide range of masses. The black holes which were formed at the the Planck time (10^{-43} s) would have the Planck mass (10^{-5} g), and those were formed at 1 s would be as massive as 10^5 solar masses. It was shown by Hawking in 1974 that a black hole radiates thermally with a temperature that is inversely proportional to its mass. This phenomenon, which is called Hawking radiation, becomes important for black holes with small enough mass. In fact, primordial black holes with a mass less than about 10^{15} g have already evaporated within the lifetime of the universe, which is 10^{10} yrs. The size of such black holes is less than 10^{-16} m, making them microscopic. Primordial black holes with an initial mass a little more than 10^{15} g are evaporating at the present time at a rate which makes it possible to detect them. In the first part of this thesis we study the particle spectra emitted from primordial microscopic black holes in the last 6 days of their existence. We assume that at very high black hole temperatures the particles emitted from black hole via Hawking radiation will scatter from each other enough to create

a shell of thermalized matter surrounding these black holes. This shell of hot matter will change the emergent spectrum from microscopic black holes. More particles with lower average energy will be emitted out of the thermalized matter compared to fewer particles with higher average energy emitted directly via Hawking radiation. This phenomenon is similar to the photosphere of stars. Because of the photosphere the temperature on the outer surface of a star is much lower than the temperature at the core of the star. In this thesis we show that the most promising route for the observation of microscopic black holes is to search for point sources emitting gamma rays of ever-increasing energy. A black hole with a temperature above 100 GeV and a Schwarzschild radius less than 10^{-4} fm will get brighter on a time scale of 6 days and then disappear. Such an observation would be remarkable, possibly unique, because astrophysical sources of gamma rays normally cool at late times. This would directly reflect the increasing Hawking temperature as the black hole explodes and disappears. Since the highest temperatures in the present universe exist in the vicinity of microscopic black holes, by studying the emergent spectrum from these black holes we can learn about the physics at very high temperatures which is not achievable in terrestrial experiments. Observation of microscopic black holes will shed light on the biggest problems in physics today. By studying and observing microscopic black holes we will be able to test the physics above the electroweak scale and beyond the four dimensional Standard Model.

It is possible that the source of the dark energy in our universe is a scalar field. Therefore, it is important to study the solutions to the combined field equations of gravity and a scalar field. In the second part of this thesis we report the discovery of static shell-like solutions to the combined field equations of gravity and a scalar field with a potential which has two non-degenerate minima. The absolute minimum of the potential is the true vacuum and the other minimum is the false vacuum. Both inside and outside of the shells are de Sitter space and their radii are comparable to the size of the horizon of the universe. The shells are spherical and very thin compared to their radii. The energy density in the shells is much higher than the energy density of

the de Sitter space inside and outside of the shells. If anything like these structures exist in nature they most likely would have been created in the early universe and are therefore cosmological. We know of no other way to produce them.

In chapter 2 of this thesis we present the work done in collaboration with J. Kapusta which can be found in [1] and [2]. In chapter 3 we present the work done in collaboration with Y. Hosotani, J. Kapusta and T. Nakajima which can be found in [3].

1.1 Microscopic Black Holes

Hawking radiation from black holes [4] is of fundamental interest because it is a phenomenon arising out of the union of general relativity and quantum mechanics, a situation that could potentially be observed. It is also of great interest because of the temperatures involved. A black hole with mass M radiates thermally with a Hawking temperature $T_H = m_P^2/8\pi M$ where $m_P = G^{-1/2} = 1.22 \times 10^{19}$ GeV is the Planck mass. (Units are $\hbar = c = k_B = 1$.) In order for the black hole to evaporate rather than accrete it must have a temperature greater than that of the present-day blackbody radiation of the universe of 2.7 K = 2.3×10^{-4} eV. This implies that M must be less than 1% of the mass of the Earth.

Such small black holes most likely would have been formed primordially; there is no other mechanism known to form them. As the black hole radiates, its mass decreases and its temperature increases until T_H becomes comparable to the Planck mass, at which point the semiclassical calculation breaks down and the regime of full quantum gravity is entered. Only in two other situations are such enormous temperatures achievable: in the early universe and in central collisions of heavy nuclei like gold or lead. Even then only about $T = 500$ MeV is reached at the RHIC (Relativistic Heavy Ion Collider) just completed at Brookhaven National Laboratory and $T = 1$ GeV is expected at the LHC (Large Hadron Collider) at CERN to be completed in 2006. Supernovae and newly formed neutron stars only reach temperatures of a few tens

of MeV. To set the scale from fundamental physics, we note that the spontaneously broken chiral symmetry of QCD gets restored in a phase transition or rapid crossover at a temperature around 170 MeV, while the spontaneously broken gauge symmetry in the electroweak sector of the standard model gets restored in a phase transition or rapid crossover at a temperature around 100 GeV. The fact that temperatures of the latter order of magnitude will never be achieved in a terrestrial experiment should motivate us to study the fate of microscopic black holes during the final days, hours and minutes of their lives when their temperatures have risen to 100 GeV and above. In this thesis we shall focus on Hawking temperatures greater than 100 GeV. The fact that microscopic black holes have not yet been observed [5] should not be viewed as a deterrent, but rather as a challenge for the new millennium!

There is some uncertainty over whether the particles scatter from each other after being emitted, perhaps even enough to allow a fluid description of the wind coming from the black hole. Let us examine what might happen as the black hole mass decreases and the associated Hawking temperature increases.

When $T_H \ll m_e$ (electron mass) only photons, gravitons, and neutrinos will be created with any significant probability. These particles will not significantly interact with each other, and will freely propagate away from the black hole with energies of order T_H . Even when $T_H \approx m_e$ the Thomson cross section is too small to allow the photons to scatter very frequently in the rarified electron-positron plasma around the black hole. This may change when $T_H \approx 100$ MeV when muons and charged pions are created in abundance. At somewhat higher temperatures hadrons are copiously produced and local thermal equilibrium may be achieved, although exactly how is an unsettled issue. Are hadrons emitted directly by the black hole? If so, they will be quite abundant at temperatures of order 150 MeV because their mass spectrum rises exponentially (Hagedorn growth as seen in the Particle Data Group tables [6]). Because they are so massive they move nonrelativistically and may form a very dense equilibrated gas around the black hole. But hadrons are composites of quarks and gluons, so perhaps quark and gluon jets are emitted instead? These jets must decay

into the observable hadrons on a typical proper length scale of 1 fm and a typical proper time scale of 1 fm/c. This was first studied by MacGibbon and Webber [7] and MacGibbon and Carr [8]. Subsequently Heckler [9] argued that since the emitted quarks and gluons are so densely packed outside the event horizon they are not actually fragmenting into hadrons in vacuum but in something more like a quark-gluon plasma, so perhaps they thermalize. He also argued that QED bremsstrahlung and pair production were sufficient to lead to a thermalized QED plasma when T_H exceeded 45 GeV [10]. These results are somewhat controversial and need to be confirmed. The issue really is how to describe the emission of wave packets via the Hawking mechanism when the emitted particles are (potentially) close enough to be mutually interacting. A more quantitative treatment of the particle interactions on a semiclassical level was carried out by Cline, Mostoslavsky and Servant [11]. They solved the relativistic Boltzmann equation with QCD and QED interactions in the relaxation-time approximation. It was found that significant particle scattering would lead to a photosphere though not perfect fluid flow.

Rather than pursuing the Boltzmann transport equation Kapusta applied relativistic viscous fluid equations to the problem assuming sufficient particle interaction [12]. It was found that a self-consistent description emerges of a fluid just marginally kept in local thermal equilibrium, and that viscosity is a crucial element of the dynamics. The fluid description has been used to calculate the particle spectra emitted in heavy ion collisions and has been very successful in this application [13]. The purpose of this thesis is a more extensive analysis of these equations and their observational consequences.

The plan of the second chapter of this thesis is as follows. In Sec. 2.1 we give a brief review of Hawking radiation sufficient for our uses. In Sec. 2.2 we give the set of relativistic viscous fluid equations necessary for this problem along with the assumptions that go into them. In Sec. 2.3 we suggest a relatively simple parametrization of the equation of state for temperatures ranging from several MeV to well over 100

GeV. We also suggest a corresponding parametrization of the bulk and shear viscosities. In Sec. 2.4 we solve the equations numerically, study the scaling behavior of the solutions, and check their physical self-consistency. In Sec. 2.5 we estimate where the transition from viscous fluid flow to free-streaming takes place. In Sec. 2.6 we calculate the instantaneous and time-integrated spectra of high energy photons from the two dominant sources: direct and neutral pion decay. In Sec. 2.7 we study the diffuse gamma ray spectrum from microscopic black holes distributed in our galactic halo. We also study the systematics of gamma rays from an individual black hole, should we be so fortunate to observe one. In Sec. 2.8 we calculate the instantaneous and time-integrated spectra of high energy neutrinos from the three dominant sources: direct, pion decay and muon decay. In Sec. 2.9 we compare the spectra from all neutrino sources graphically. We also compare our results with the spectra of neutrinos emitted directly as Hawking radiation without any subsequent interactions. In Sec. 2.10 we study the possibility of observing neutrinos from a microscopic black hole directly.

1.2 Cosmic Shells

Gravitational interactions, which are inherently attractive for ordinary matter, can produce soliton-like objects even when they are strictly forbidden in flat space. They are possible as a consequence of the balance between repulsive and attractive forces. One such example is a monopole or dyon solution in the pure Einstein-Yang-Mills theory in the asymptotically anti-de Sitter space [14, 15, 16]. In the pure Yang-Mills theory in flat space there can be no static solution at all [17] but once gravitational interaction is included there arise particle like solutions [18]. Whereas all solutions are unstable in the asymptotically flat or de Sitter space, there appear a continuum of stable monopole and dyon solutions in the asymptotically anti-de Sitter space. The stable solutions are cosmological in nature; their size is typically of order $|\Lambda|^{-1/2}$ where Λ is the cosmological constant.

The possibility of false vacuum black holes has also been explored. Suppose that the potential in a scalar field theory has two minima, one corresponding to the true vacuum and the other to the false vacuum. If the universe is in the false vacuum, a bubble of the true vacuum is created by quantum tunneling which expands with accelerated velocity. The configuration is called a bounce [19]. Now flip the configuration [20]. The universe is in the true vacuum with potential $V = 0$ and the inside of a sphere is excited to the false vacuum with $V > 0$. Is such a de Sitter lump in Minkowski space possible? If the lump is too small it would be totally unstable. The energy localized inside the lump can dissipate to spatial infinity. If the lump is big enough the Schwarzschild radius becomes larger than the lump radius so that the lump is inside a black hole. The energy cannot escape to infinity. It looks like a soliton in Minkowski space. However, as a black hole it is a dynamical object. The configuration is essentially time dependent. This false vacuum black hole configuration, however, does not solve the static field equations at the horizon. It has been recently proven that there can be no such everywhere-regular black hole solution [21, 22]. Rather, false vacuum lumps in flat space evolve dynamically [23, 24, 25].

The purpose of this part of thesis is to report new solutions to the coupled equations of gravity and scalar field theory which display a spherically symmetric shell structure [26]. We demonstrate that such a structure appears when the potential for a scalar field has two local minima and the space is asymptotically de Sitter. In the examples we present, both the inside and outside of the shells are de Sitter space with the same cosmological constant. The structure becomes possible only when the energy scale of the scalar field potential becomes small compared with the Planck scale. While such shell structures might not be easy to create in the present universe, it is quite plausible that they could have been created during a phase transition early in the universe [23]. A similar configuration has been investigated in Ref. [27].

The plan of the third chapter of this thesis is as follows. In Sec. 3.1 we precisely state the problem, solve the field equations in those regions of space-time where they can be linearized, and sketch the solution in the nonlinear shell region in static

coordinates. In Sec. 3.2 we solve the nonlinear equations in the shell region and display the dependence on the parameters of the theory. In Sec. 3.3 we extend the solution from static coordinates, which have a coordinate singularity, to other coordinate systems that do not, thereby displaying the existence and character of the solution throughout the full space-time manifold. In Sec. 3.4 we study the stability of the classical solution to quantum fluctuations. Finally in chapter 4 we will conclude and summarize both parts of this thesis.

Chapter 2

High Temperature Matter and Particle Spectra from Microscopic Black Holes

2.1 Hawking Radiation

There are at least two intuitive ways to think about Hawking radiation from black holes. One way is vacuum polarization. Particle-antiparticle pairs are continually popping in and out of the vacuum, usually with no observable effect. In the presence of matter, however, their effects can be observed. This is the origin of the Lamb effect first measured in atomic hydrogen in 1947. When pairs pop out of the vacuum near the event horizon of a black hole one of them may be captured by the black hole and the other by necessity of conservation laws will escape to infinity with positive energy. The black hole therefore has lost energy - it radiates. Due to the general principles of thermodynamics applied to black holes it is quite natural that it should radiate thermally. An intuitive argument that is more quantitative is based on the uncertainty principle. Suppose that we wish to confine a massless particle to the vicinity of a black hole. Given that the average momentum of a massless particle at temperature T is

approximately πT , the uncertainty principle requires that confinement to a region the size of the Schwarzschild diameter places a restriction on the minimum value of the temperature

$$\pi T \cdot 2r_S > 1/2. \quad (2.1)$$

The minimum is actually attained for the Hawking temperature. The various physical quantities are related as $r_S = 2M/m_{\text{P}}^2 = 1/4\pi T_H$.

The number of particles of spin s emitted with energy E per unit time is given by the formula

$$\frac{dN_s}{dEdt} = \frac{\Gamma_s}{2\pi} \frac{1}{\exp(E/T_H) - (-1)^{2s}}. \quad (2.2)$$

All the computational effort really goes into calculating the absorption coefficient Γ_s from a relativistic wave equation in the presence of a black hole. Integrating over all particle species yields the luminosity

$$L = -\frac{dM}{dt} = \alpha(M) \frac{m_{\text{P}}^4}{M^2} = 64\pi^2 \alpha(T_H) T_H^2. \quad (2.3)$$

Here $\alpha(M)$ is a function reflecting the species of particles available for creation in the gravitational field of the black hole. It is generally sufficient to consider only those particles with mass less than T_H ; more massive particles are exponentially suppressed by the Boltzmann factor. Then

$$\alpha = 2.011 \times 10^{-8} \left[3700N_0 + 2035N_{1/2} + 835N_1 + 95N_2 \right] \quad (2.4)$$

where N_s is the net number of polarization degrees of freedom for all particles with spin s and with mass less than T_H . The coefficients for spin 1/2, 1 and 2 were computed by Page [28] and for spin 0 by Sanchez [29]*. In the standard model $N_0 = 4$ (Higgs boson), $N_{1/2} = 90$ (three generations of quarks and leptons), $N_1 = 24$ [SU(3)×SU(2)×U(1) gauge theory], and $N_2 = 2$ (gravitons). This assumes T_H is greater than the temperature for the electroweak gauge symmetry restoration.

*In [1] the coefficient for spin 0 particles was taken as 4200. In Eq. (2.4) we have reduced this value to 3700 which results in a small correction of 0.7% in the numerical value of $\alpha(T_H > 100 \text{ GeV})$. We thank Harald Anlauf for providing us with this more accurate coefficient

Numerically $\alpha(T_H > 100 \text{ GeV}) = 4.4 \times 10^{-3}$. Starting with a black hole of temperature T_H , the time it takes to evaporate or explode is

$$\Delta t = \frac{m_{\text{P}}^2}{3\alpha(T_H)(8\pi T_H)^3}. \quad (2.5)$$

This is also the characteristic time scale for the rate of change of the luminosity of a black hole with temperature T_H .

At present a black hole will explode if $T_H > 2.7 \text{ K}$ and correspondingly $M < 4.6 \times 10^{25} \text{ g}$ which is approximately 1% of the mass of the Earth. More massive black holes are cooler and therefore will absorb more matter and radiation than they radiate, hence grow with time. Taking into account emission of gravitons, photons, and neutrinos a critical mass black hole today has a Schwarzschild radius of 68 microns and a lifetime of 2×10^{43} years.

2.2 Relativistic Viscous Fluid Equations

The relativistic imperfect fluid equations describing a steady-state, spherically symmetric flow with no net baryon number or electric charge and neglecting gravity (see below) are $T^{\mu\nu}{}_{;\nu} = \text{black hole source}$. The nonvanishing components of the energy-momentum tensor in radial coordinates are [30]

$$\begin{aligned} T^{00} &= \gamma^2(P + \epsilon) - P + v^2 \Delta T_{\text{diss}} \\ T^{0r} &= v\gamma^2(P + \epsilon) + v\Delta T_{\text{diss}} \\ T^{rr} &= v^2\gamma^2(P + \epsilon) + P + \Delta T_{\text{diss}} \end{aligned} \quad (2.6)$$

representing energy density, radial energy flux, and radial momentum flux, respectively, in the rest frame of the black hole. Here v is the radial velocity with γ the corresponding Lorentz factor, $u = v\gamma$, ϵ and P are the local energy density and pressure, and

$$\Delta T_{\text{diss}} = -\frac{4}{3}\eta\gamma^2 \left(\frac{du}{dr} - \frac{u}{r} \right) - \zeta\gamma^2 \left(\frac{du}{dr} + \frac{2u}{r} \right), \quad (2.7)$$

where η is the shear viscosity and ζ is the bulk viscosity. A thermodynamic identity gives $Ts = P + \epsilon$ for zero chemical potentials, where T is temperature and s is entropy density. There are two independent differential equations of motion to solve for the functions $T(r)$ and $v(r)$. These may succinctly written as

$$\begin{aligned}\frac{d}{dr} (r^2 T^{0r}) &= 0 \\ \frac{d}{dr} (r^2 T^{rr}) &= 0.\end{aligned}\tag{2.8}$$

An integral form of these equations is sometimes more useful since it can readily incorporate the input luminosity from the black hole. The first represents the equality of the energy flux passing through a sphere of radius r with the luminosity of the black hole:

$$4\pi r^2 T^{0r} = L.\tag{2.9}$$

The second follows from integrating a linear combination of the differential equations. It represents the combined effects of the entropy from the black hole together with the increase of entropy due to viscosity:

$$4\pi r^2 u s = 4\pi \int_{r_0}^r dr' r'^2 \frac{1}{T} \left[\frac{8}{9} \eta \left(\frac{du}{dr'} - \frac{u}{r'} \right)^2 + \zeta \left(\frac{du}{dr'} + \frac{2u}{r'} \right)^2 \right] + \frac{L}{T_H}.\tag{2.10}$$

The term L/T_H arises from equating the entropy per unit time lost by the black hole $-dS_{\text{bh}}/dt$ with that flowing into the matter. Using the area formula for the entropy of a black hole, $S_{\text{bh}} = m_{\text{P}}^2 \pi r_S^2 = 4\pi M^2/m_{\text{P}}^2$, and identifying $-dM/dt$ with the luminosity, the entropy input from the black hole is obtained.

The above pair of equations are to be applied beginning at some radius r_0 greater than the Schwarzschild radius r_S , that is, outside the quantum particle production region of the black hole. The radius r_0 at which the imperfect fluid equations are first applied should be chosen to be greater than the Schwarzschild radius, otherwise the computation of particle creation by the black hole would be invalid. It should not be too much greater, otherwise particle collisions would create more entropy than is accounted for by the equation above. The energy and entropy flux into the fluid come

from quantum particle creation by the black hole at temperature T_H . Gravitational effects are of order r_S/r , hence negligible for $r > (5 - 10)r_S$.

2.3 Equation of State and Transport Coefficients

Determination of the equation of state as well as the two viscosities for temperatures ranging from MeV to TeV and more is a formidable task. Here we shall present some relatively simple parametrizations that seem to contain the essential physics. Improvements to these can certainly be made, but probably will not change the viscous fluid flow or the observational consequences very much.

The hot shell of matter surrounding a primordial black hole provides a theoretical testing ground rivaled only by the big bang itself. To illustrate this we have plotted a semi-realistic parametrization of the equation of state in figure 2.1. Gravitons and neutrinos are not included. We assume a second order electroweak phase transition at a temperature of $T_{EW} = 100$ GeV. Above that temperature the standard model has 101.5 effective massless bosonic degrees of freedom (as usual fermions count as 7/8 of a boson). We assume a first order QCD phase transition at a temperature of $T_{QCD} = 170$ MeV. The number of effective massless bosonic degrees of freedom changes from 47.5 just above this critical temperature (u, d, s quarks and gluons) to 7.5 just below it (representing the effects of all the massive hadrons in the Particle Data Group tables) [31]. Below 30 MeV only electrons, positrons, and photons remain, and finally below a few hundred keV only photons survive in any appreciable number. The explicit parametrization shown in figure 2.1 is as follows:

$$s(T) = \frac{4\pi^2}{90} T^3 \begin{cases} 101.5, & T_{EW} \leq T, \\ 56.5 + 45 e^{-(T_{EW}-T)/T}, & T_{QCD} \leq T < T_{EW}, \\ 2 + 3.5 e^{-m_e/T} + 27.25 e^{-(T_{QCD}-T)/T}, & T < T_{QCD}. \end{cases} \quad (2.11)$$

It may very well be that there are no true thermodynamic phase transitions in the standard model but only rapid crossovers from one phase to the other. None of our

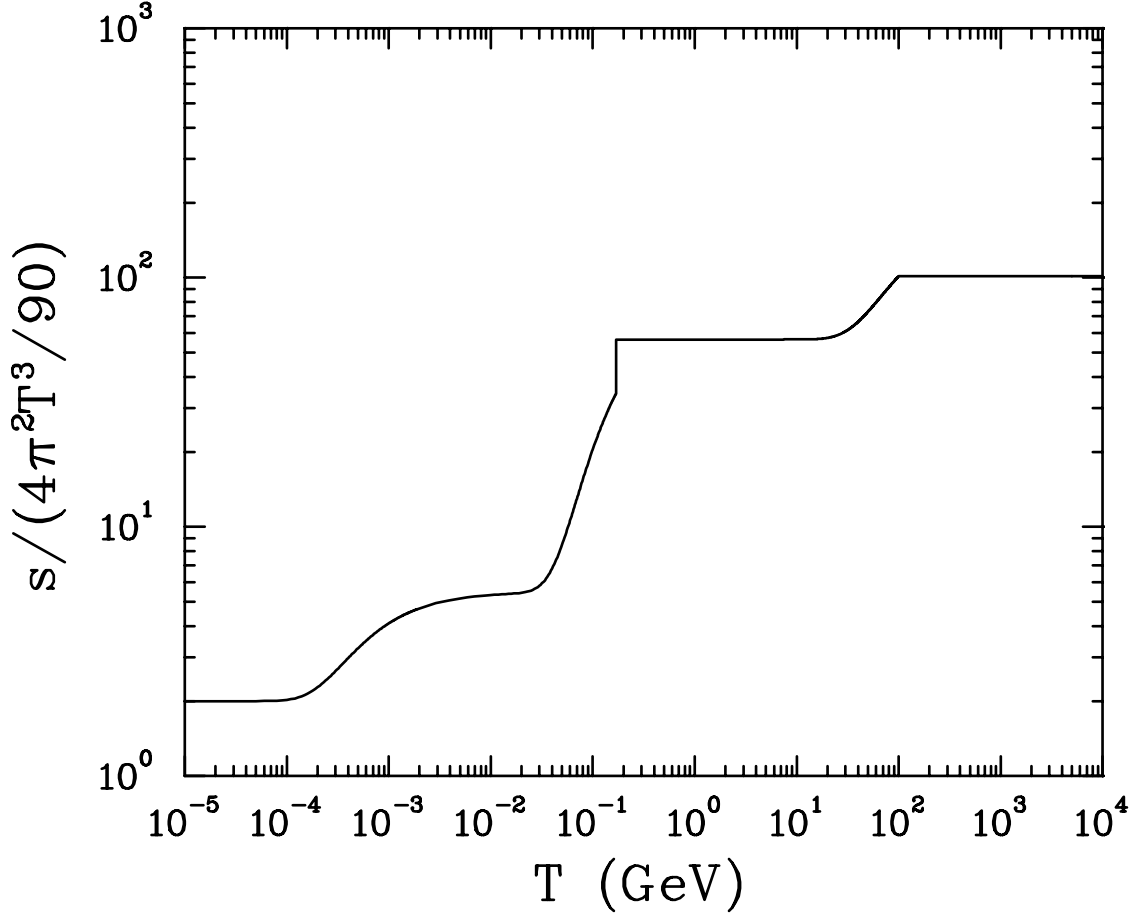


Figure 2.1: Entropy density as a function of temperature, excluding neutrinos and gravitons. It is assumed that the QCD phase transition is first order and the EW phase transition is second order.

calculations or results depend on such details. A word about neutrinos: It is quite possible that they should be considered in approximate equilibrium at temperatures above 100 GeV where the electroweak symmetry is restored. Still there is some uncertainty about this. Since they provide only a few effective degrees of freedom out of more than 100 their neglect should cause negligible error.

Now we turn to the viscosities. The shear viscosity was calculated in [32] for the full standard model in the symmetry restored phase, meaning temperatures above 100 GeV or so, using the relaxation time approximation. The result is

$$\eta(T > 100 \text{ GeV}) = 82.5 T^3 \quad (2.12)$$

when numerical values for coupling constants etc. are put in. The shear viscosity for QCD degrees of freedom only was calculated to leading order in the QCD coupling α_s in [33] to be

$$\eta(\text{QCD}) = \frac{0.342(1 + 1.7N_f)}{(1 + N_f/6)\alpha_s^2 \ln(\alpha_s^{-1})} T^3 \quad (2.13)$$

where N_f is the number of quark flavors whose mass is less than T . An improved calculation for gauge theories was given in [34]; for QCD there is very little difference with [33]. We observe that the ratio of the shear viscosity to the entropy density, as appropriate for the above two cases, is dimensionless and has about the same numerical value in both. Therefore, as a practical matter we assume that the shear viscosity always scales with the entropy density for all temperatures of interest. We take the constant of proportionality from the full standard model cited above:

$$\eta = \frac{82.5}{101.5} \left(\frac{s}{4\pi^2/90} \right). \quad (2.14)$$

There is even less known about the bulk viscosity at the temperatures of interest to us. The bulk viscosity is zero for point particles with no internal degrees of freedom and with local interactions among them. In renormalizable quantum field theories the interactions are not strictly local. In particular, the coupling constants acquire temperature dependence according to the renormalization group. For example, to one loop order the QCD coupling has the functional dependence $\alpha_s \sim 1/\ln(T/\Lambda)$ where Λ is the QCD scale. On account of this dependence the bulk viscosity is nonzero. We estimate that

$$\zeta \approx 10^{-4} \eta \quad (2.15)$$

and this is what we shall use in the numerics.

Overall we have a modestly realistic description of the equation of state and the viscosities that are still a matter of theoretical uncertainty. One needs $s(T), \eta(T), \zeta(T)$ over a huge range of T . Of course, these are some of the quantities one hopes to obtain experimental information on from observations of exploding black holes.

2.4 Numerical Solution and Scaling

Several limiting cases of the relativistic viscous fluid equations were studied in [12]. The most realistic situation used the equation of state $\epsilon = aT^4$, $s = (4/3)aT^3$ and viscosities $\eta = b_S T^3$, $\zeta = b_B T^3$ with the coefficients a , b_S , b_B all constant. A scaling solution, valid at large radii when $\gamma \gg 1$, was found to be $T(r) = T_0(r_0/r)^{2/3}$ and $\gamma(r) = \gamma_0(r/r_0)^{1/3}$. The constants must be related by $36aT_0r_0 = (32b_S + 441b_B)\gamma_0$. This r -dependence of T and γ is exactly what was conjectured by Heckler [10].

It was shown in [12] that if approximate local thermal equilibrium is achieved it can be maintained, at least for the semi-realistic situation described above. The requirement is that the inverse of the local volume expansion rate $\theta = u^\mu{}_{;\mu}$ be comparable to or greater than the relaxation time for thermal equilibrium [30]. Expressed in terms of a local volume element V and proper time τ it is $\theta = (1/V)dV/d\tau$, whereas in the rest frame of the black hole the same quantity can be expressed as $(1/r^2)d(r^2u)/dr$. Explicitly

$$\theta = \frac{7\gamma_0}{3r_0} \left(\frac{r_0}{r}\right)^{2/3} = \frac{7\gamma_0}{3r_0 T_0} T. \quad (2.16)$$

Of prime importance in achieving and maintaining local thermal equilibrium in a relativistic plasma are multi-body processes such as $2 \rightarrow 3$ and $3 \rightarrow 2$, etc. This has been well-known when calculating quark-gluon plasma formation and evolution in high energy heavy ion collisions [35, 36] and has been emphasized in Refs. [9, 10] in the context of black hole evaporation. This is a formidable task in the standard model with its 16 species of particles. Instead three estimates for the requirement that local thermal equilibrium be maintained were made. The first and simplest estimate is to require that the thermal de Broglie wavelength of a massless particle, $1/3T$, be less than $1/\theta$. The second estimate is to require that the Debye screening length for each of the gauge groups in the standard model be less than $1/\theta$. The Debye screening length is the inverse of the Debye screening mass m_n^D where $n = 1, 2, 3$ for the gauge groups $U(1)$, $SU(2)$, $SU(3)$. Generically $m_n^D \propto g_n T$ where g_n is the gauge coupling constant and the coefficient of proportionality is essentially the square root of the number of

charge carriers [37]. For example, for color SU(3) $m_3^D = g_3 \sqrt{1 + N_f/6} T$ where N_f is the number of light quark flavors at the temperature T . The numerical values of the gauge couplings are: $g_1 = 0.344$, $g_2 = 0.637$, and $g_3 = 1.18$ (evaluated at the scale m_Z) [6]. So within a factor of about 2 we have $m^D \approx T$. The third and most relevant estimate is the mean time between two-body collisions in the standard model for temperatures greater than the electroweak symmetry restoration temperature. This mean time was calculated in [32] in the process of calculating the viscosity in the relaxation time approximation. Averaged over all particle species in the standard model one may infer from that paper an average time of $3.7/T$. Taking into account multi-body reactions would decrease that by about a factor of two to four. All three of these estimates are consistent within a factor of 2 or 3. The conclusion to be drawn is that local thermal equilibrium should be achieved when $\theta \lesssim T$. Once thermal equilibrium is achieved it is not lost because θ/T is independent of r . The picture that emerges is that of an imperfect fluid just marginally kept in local equilibrium by viscous forces.

The results quoted above are only valid at large r and for the equation of state $s \propto T^3$. To know the behavior of the solution at non-asymptotic r and for the more sophisticated equation of state and viscosities described in Sec. 2.3 requires a numerical analysis. We have found that the most convenient form of the viscous fluid equations for numerical evaluation are

$$4\pi r^2 \left[\gamma u T s - \frac{4}{3} \eta \gamma u \left(\frac{du}{dr} - \frac{u}{r} \right) - \zeta \gamma u \left(\frac{du}{dr} + \frac{2u}{r} \right) \right] = L \quad (2.17)$$

for energy conservation [from Eq. (2.9)] and

$$\frac{d}{dr} (4\pi r^2 u s) = \frac{4\pi r^2}{T} \left[\frac{8}{9} \eta \left(\frac{du}{dr} - \frac{u}{r} \right)^2 + \zeta \left(\frac{du}{dr} + \frac{2u}{r} \right)^2 \right] \quad (2.18)$$

for entropy flow [from Eq. (2.10)]. Obviously the entropy flux is a monotonically increasing function of r because of dissipation.

Mathematically the above pair of equations apply for all $r > 0$, although physically we should only apply them beyond the Schwarzschild radius r_S . Let us study them

first in the limit $r \rightarrow 0$, which really means the assumption that $v \ll 1$. Then $u \approx v$ and $\gamma \approx 1$. We also consider black hole temperatures greater than T_{EW} so that the equation of state and the viscosities no longer change their functional forms. It is straightforward to check that a power solution satisfies the equations, with

$$\begin{aligned} u(r) &= u_i(r/r_i)^{2/5} \\ T(r) &= T_i(r_i/r)^{3/5} \end{aligned} \quad (2.19)$$

where r_i is some reference radius. If the luminosity and the reference radius are given

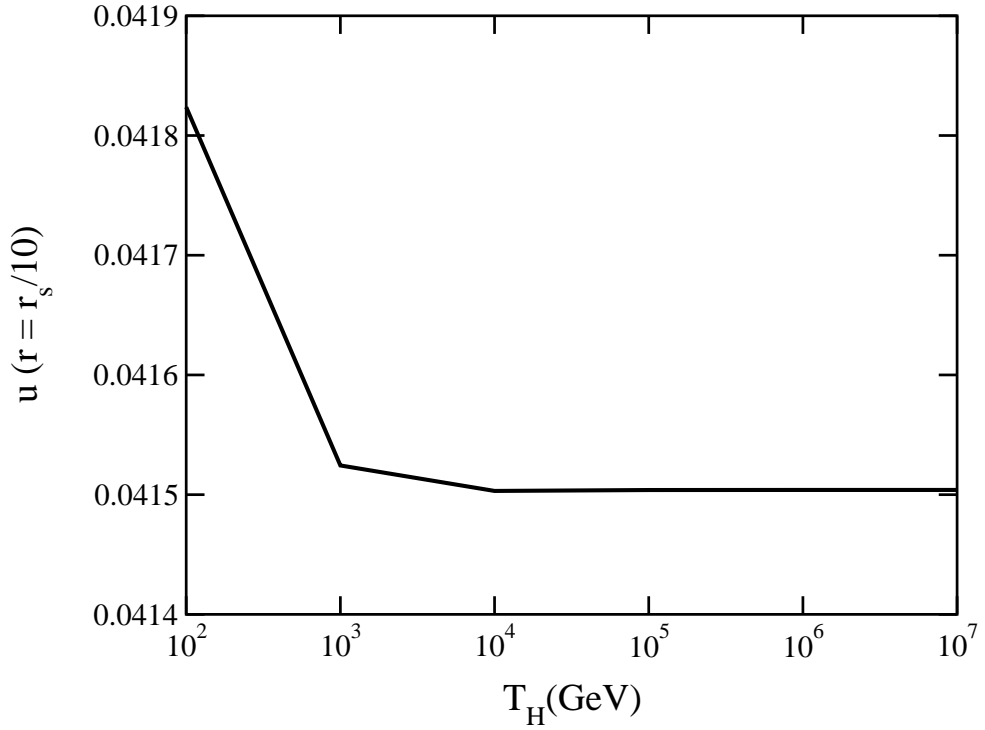


Figure 2.2: The value of $u = v\gamma$ at one-tenth the Schwarzschild radius as determined by numerical solution. The physical applicability of the numerical solution begins at radii greater than r_S .

then u_i and T_i are determined by the fluid equations.

The numerical solution for all radii needs some initial conditions. Typically we

begin the solution at one-tenth the Schwarzschild radius. At this radius the u_i , as determined above, is small enough to serve as a good first estimate. However, it needs to be fine-tuned to give an acceptable solution at large r . For example, at large r there is an approximate but false solution: $T = \text{const}$ with $u \sim r$. The problem is that we need a solution valid over many orders of magnitude of r . If Eq. (2.17) is divided by r^2 and if the right hand side is neglected in the limit $r \rightarrow \infty$ then the left hand side is forced to be zero. We have used both Mathematica and a fourth order Runge-Kutta method with adaptive step-size to solve the equations. They give consistent results. For more details on numerical calculations, see appendix A.

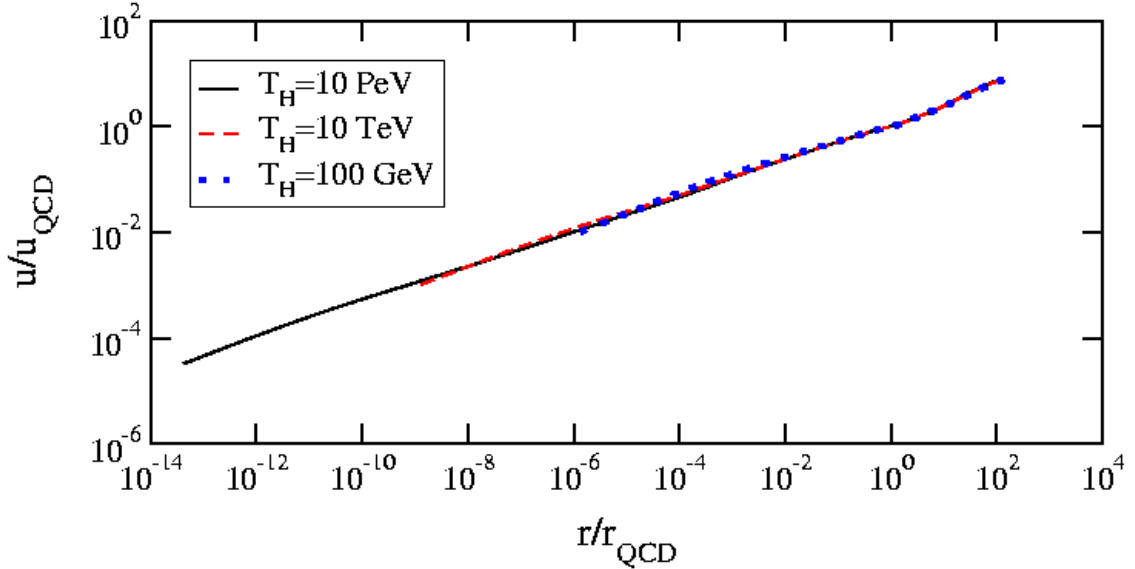


Figure 2.3: The radial dependence of u for three different Hawking temperatures. The curves begin at $r_S/10$ and terminate when the local temperature reaches 10 MeV.

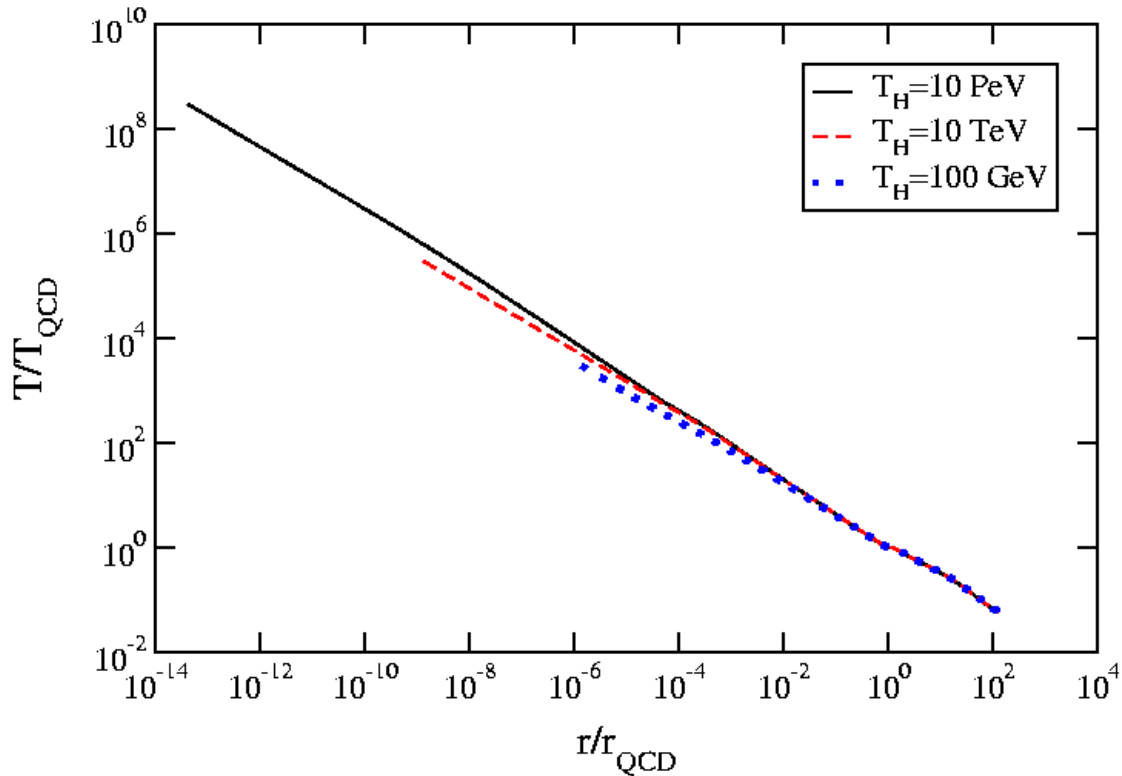


Figure 2.4: The radial dependence of T for three different Hawking temperatures. The curves begin at $r_S/10$ and terminate when the local temperature reaches 10 MeV.

In figure 2.2 we plot $u(r_S/10)$ versus T_H . It is essentially constant for all $T_H > T_{EW}$ with the value of 0.0415. In figure 2.3 we plot the function $u(r)$ versus r for three different black hole temperatures. The radial variable r is expressed in units of its value when the temperature first reaches T_{QCD} , and u is expressed in units of its value at that same radius. This allows us to compare different black hole temperatures. To rather good accuracy these curves seem to be universal as they essentially lie on top of one another. The curves are terminated when the temperature reaches 10 MeV. The function $u(r)$ behaves like $r^{1/3}$ until temperatures of order 100 MeV are reached.

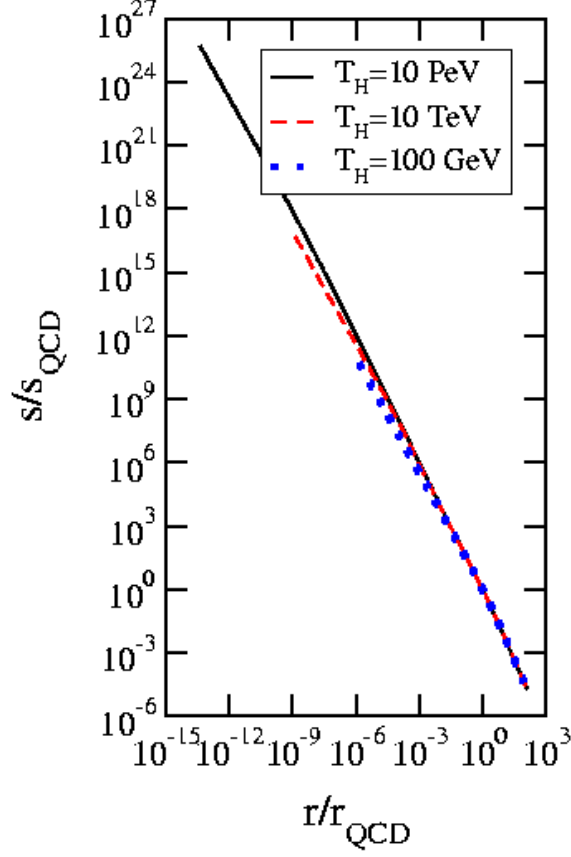


Figure 2.5: The radial dependence of s for three different Hawking temperatures. The curves begin at $r_S/10$ and terminate when the local temperature reaches 10 MeV.

The simple parametrization

$$u(r) = u_S (r/r_S)^{1/3} \quad (2.20)$$

with $u_S = 0.10$ will be very useful when studying radiation from the surface of the fluid.

In figure 2.4 we plot the temperature in units of T_{QCD} versus the radius in units of r_{QCD} for the same three black hole temperatures as in figure 2.3. Again the curves are terminated when the temperature drops to 10 MeV. The curves almost fall on top of one another but not perfectly. The temperature falls slightly slower

than the power-law behavior $r^{-2/3}$ expected on the basis of the equation of state $s = (4/3)aT^3$. The reason is that the effective number of degrees of freedom is falling with the temperature. The entropy density is shown in figure 2.5. It also exhibits an imperfect degree of scaling similar to the temperature.

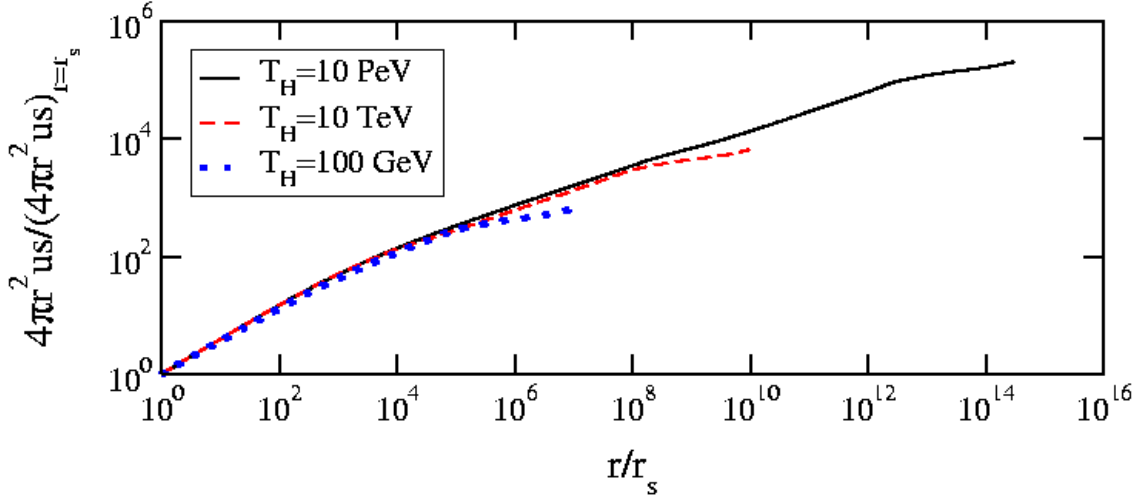


Figure 2.6: The radial dependence of the entropy flow for three different Hawking temperatures. The curves begin at $r_S/10$ and terminate when the local temperature reaches 10 MeV.

Since viscosity plays such an important role in the outgoing fluid we should expect significant entropy production. In figure 2.6 we plot the entropy flow $4\pi r^2 u_s$ as a function of radius for the same three black hole temperatures as in figures 2.3-2.5. It increases by several orders of magnitude. The fluid flow is far from isentropic.

2.5 Onset of Free-Streaming

Eventually the fluid expands so rapidly that the particles composing the fluid lose thermal contact with each other and begin free-streaming as is shown in figure 2.7. In heavy ion physics this is referred to as thermal freeze-out, and in astronomy it is usually associated with the photosphere of a star. In the sections above we argued

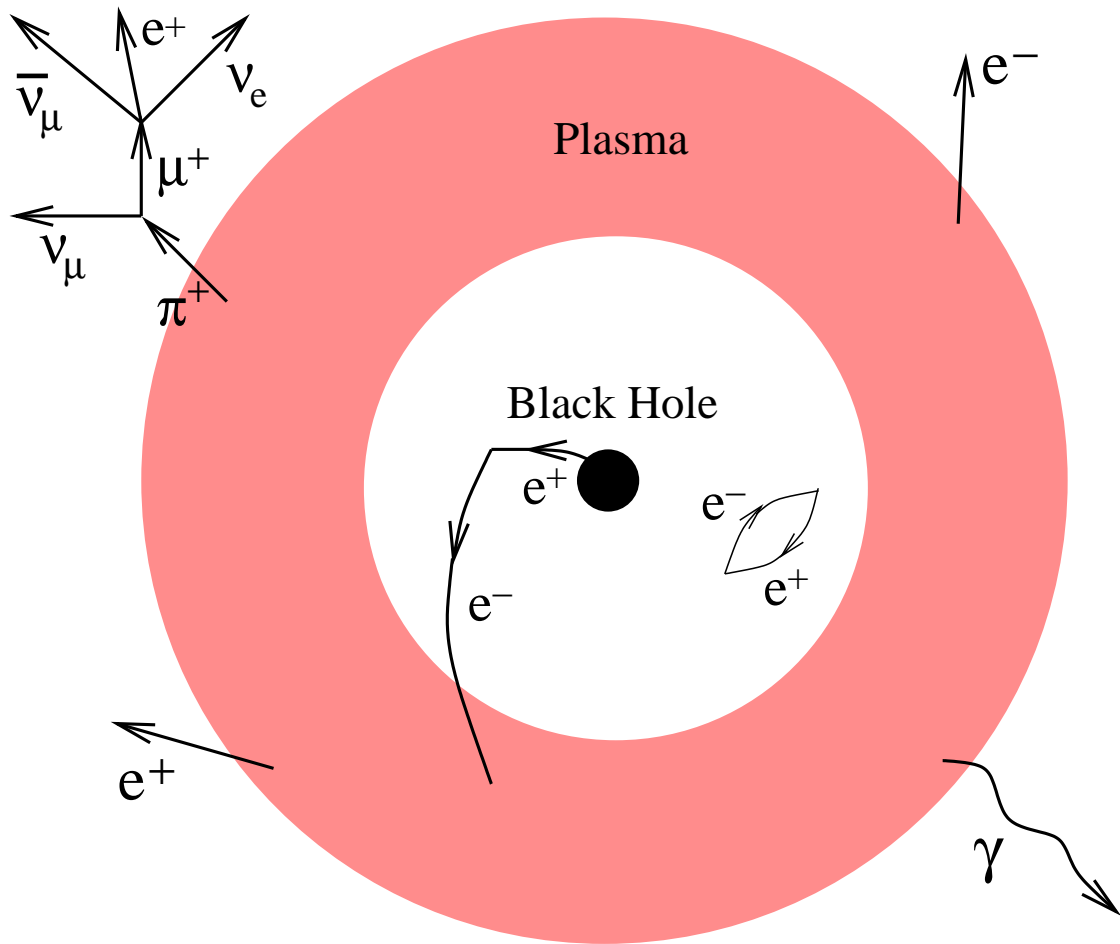


Figure 2.7: Free-streaming of particles at freeze-out surface.

that thermal contact should occur for all particles, with the exception of gravitons and neutrinos, down to temperatures on the order of T_{QCD} . Below that temperature the arguments given no longer apply directly; for example, the relevant interactions

are not those of perturbative QCD.

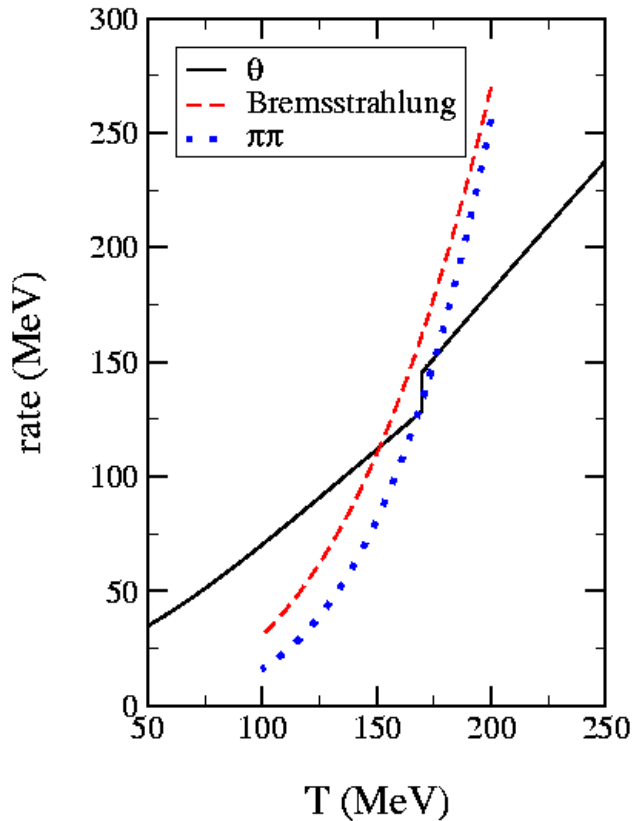


Figure 2.8: The rate for $\pi\pi$ scattering and for the bremsstrahlung reaction $ee \rightarrow ee\gamma$ are compared to the local volume expansion rate. The Hawking temperature is 10 TeV.

Extensive studies have been made of the interactions among hadrons at finite temperature. Prakash *et al.* [38] used experimental information to construct scattering amplitudes for pions, kaons and nucleons and from them computed thermal relaxation rates. The relaxation time for $\pi - \pi$ scattering can be read off from their figures and simply parametrized as

$$\tau_{\pi\pi}^{-1} \approx 16 \left(\frac{T}{100 \text{ MeV}} \right)^4 \text{ MeV} \quad (2.21)$$

which is valid for $100 < T < 200$ MeV. This rate is compared to the volume expansion

rate θ (see Sec. 2.4) in figure 2.8. From the figure it is clear that pions cannot maintain thermal equilibrium much below 160 MeV or so. Since pions are the lightest hadrons and therefore the most abundant at low temperatures, it seems unlikely that other hadrons could maintain thermal equilibrium either.

Heckler has argued vigorously that electrons and photons should continue to interact down to temperatures on the order of the electron mass [9, 10]. Multi-particle reactions are crucial to this analysis. Let us see how it applies to the present situation. Consider, for example, the cross section for $ee \rightarrow ee\gamma$. The energy-averaged cross section is [10]

$$\bar{\sigma}_{\text{brem}} = 8\alpha_{EM}r_0^2 \ln(2E/m_e) \quad (2.22)$$

where m_e is the electron mass, $r_0 = \alpha_{EM}/m_e$ is the classical electron radius, and $E \gg m_e$ is the energy of the incoming electrons in the center-of-momentum frame. (If one computes the rate for a photon produced with the specific energies $0.1E$, $0.25E$, or $0.5E$ the cross section would be larger by a factor 4.73, 2.63, or 1.27, respectively.) The rate using the energy-averaged cross section is

$$\tau_{\text{brem}}^{-1} \approx \left[\frac{3}{\pi^2} \xi(3) T^3 \right] \left[\frac{8\alpha_{EM}^3}{m_e^2} \ln(6T/m_e) \right] \quad (2.23)$$

where we have used the average energy $\langle E \rangle \approx 3T$ for electrons with $m_e \ll T$. This rate is also plotted in figure 2.8. It is large enough to maintain local thermal equilibrium down to temperatures on the order of 140 MeV. Of course, there are other electromagnetic many-particle reactions which would increase the overall rate. On the other hand, as pointed out by Heckler [10], these reactions are occurring in a high density plasma with the consequence that dispersion relations and interactions are renormalized by the medium. If one takes into account only renormalization of the electron mass, such that $m_{eff}^2 \approx m_e^2 + e^2 T^2/3$ when $m_e \ll T$, then the rate would be greatly reduced.

Does this mean that photons and electrons are not in thermal equilibrium at the temperatures we have been discussing? Consider bremsstrahlung reactions in the QCD plasma. There are many $2 \rightarrow 3$ reactions, such as: $q_1 q_2 \rightarrow q_1 q_2 \gamma$, $q_1 \bar{q}_2 \rightarrow q_1 \bar{q}_2 \gamma$,

$gg \rightarrow q\bar{q}\gamma$, and so on. Here the subscripts label the quark flavor, which may or may not be the same. The rate for these can be estimated using known QED and QCD cross sections [39, 40, 41]. Using an effective quark mass given by gT we find that the rate is $\alpha_s T$ with a coefficient of order or larger than unity. Since α_s becomes of order unity near T_{QCD} we conclude that photons are in equilibrium down to temperatures of that order at least. To make the matter even more complicated we must remember that the expansion rate θ is based on a numerical solution of the viscous fluid equations which assume a constant proportionality between the shear and bulk viscosities and the entropy density. Although these proportionalities may be reasonable in QCD and electroweak plasmas at high temperatures they may fail at temperatures below T_{QCD} . The viscosities should be computed using the relaxation times for self-consistency of the transition from viscous fluid flow to free-streaming, which we have not done. For example, the first estimate for the shear viscosity for massless particles with short range interactions is $T^4\tau$ where τ is the relaxation time. For pions we would get $\eta \sim \text{const}$, not $\eta \sim T^3$. As another example, we must realize that the bulk viscosity can become significant when the particles can be excited internally. This is, in fact, the case for hadrons. Pions, kaons and nucleons are all the lowest mass hadrons each of which sits at the base of a tower of resonances [6]. See, for example, [42] and references therein.

In order to do gamma ray phenomenology we need a practical criterion for the onset of free-streaming. We shall assume that this happens suddenly at a temperature T_f in the range 100 to 140 MeV. We shall assume that particles whose mass is significantly greater than T_f have all annihilated, leaving only photons, electrons, muons and pions. In figure 2.9 we plot the freeze-out radius $r_f = r(T_f)$ for $T_f = 100, 120$ and 140 MeV versus the Schwarzschild radius. The fact that r_f increases as T_f decreases is an obvious consequence of energy conservation. More interesting is the power-law scaling: $r_f \sim r_S^{-1/2} \sim T_H^{1/2}$. This scaling can be understood as follows.

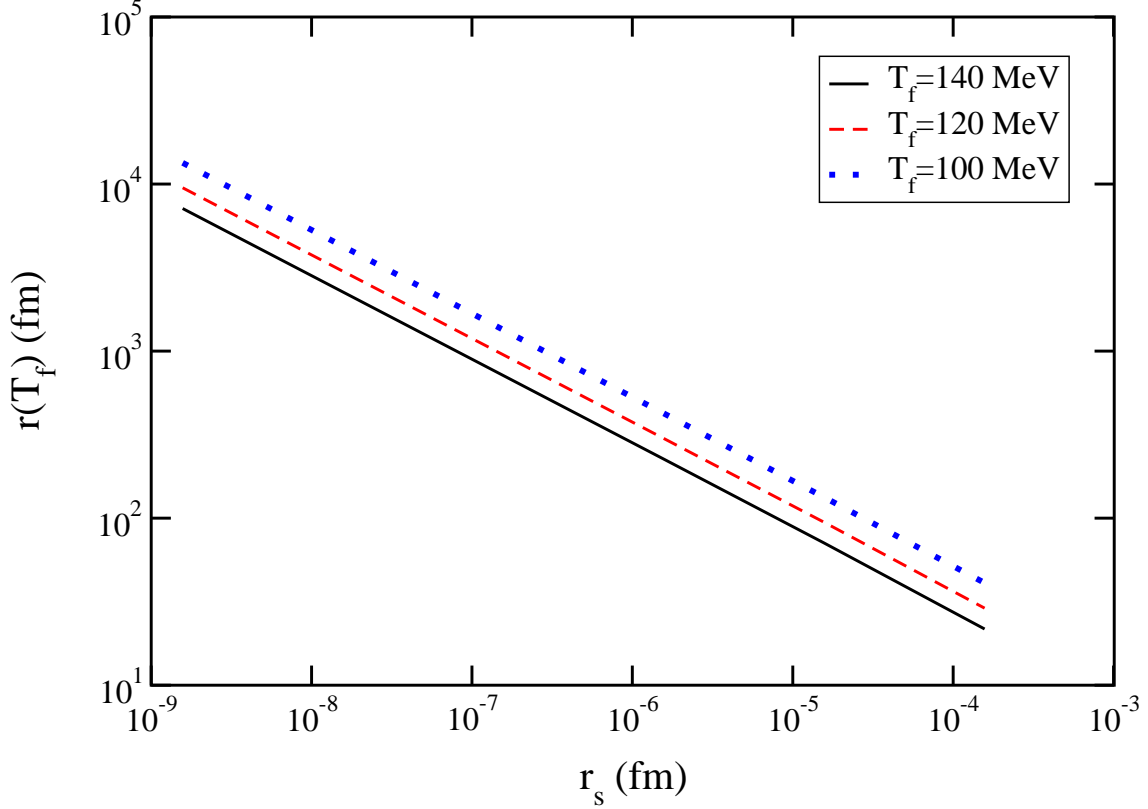


Figure 2.9: The freeze-out or free-streaming radius as a function of the Schwarzschild radius for three different freeze-out temperatures.

The luminosity from the decoupling or freeze-out surface is

$$L_f = 4\pi r_f^2 \left(\frac{2\pi^2}{45} \gamma_f^2 T_f^4 \right) d_f \quad (2.24)$$

where the quantity in parentheses is the surface flux for one massless bosonic degree of freedom and d_f is the total number of effective massless bosonic degrees of freedom. For the particles listed above we have $d_f = 12$. By energy conservation this is to be equated with the Hawking formula for the black hole luminosity,

$$L_h = 64\pi^2 \alpha_h^{eff} T_H^2, \quad (2.25)$$

where α_h^{eff} does not include the contribution from gravitons and neutrinos. Together

with the scaling function for the flow velocity, Eq. (2.20), we can solve for the radius

$$r_f = \frac{2}{\pi} \left(\frac{45\pi\alpha_h^{eff}}{2u_S^2 d_f} \right)^{3/8} \sqrt{\frac{T_H}{T_f^3}} \quad (2.26)$$

and for the boost

$$\gamma_f T_f = 2u_S \left(\frac{45\pi\alpha_h^{eff}}{2u_S^2 d_f} \right)^{1/8} \sqrt{T_f T_H} \approx 0.22 \sqrt{T_f T_H}. \quad (2.27)$$

From these we see that the final radius does indeed scale like the inverse of the square-root of the Schwarzschild radius or like the square-root of the black hole temperature, and that the average particle energy (proportional to $\gamma_f T_f$) scales like the square-root of the black hole temperature. One important observational effect is that the average energy of the outgoing particles is reduced but their number is increased compared to direct Hawking emission into vacuum [9, 10].

2.6 Photon Emission

Photons observed far away from the black hole primarily come from one of two sources. Either they are emitted directly in the form of a boosted black-body spectrum, or they arise from neutral pion decay. We will consider each of these in turn.

2.6.1 Direct photons

Photons emitted directly have a Planck distribution in the local rest frame of the fluid. The phase space density is

$$f(E') = \frac{1}{e^{E'/T_f} - 1}. \quad (2.28)$$

The energy appearing here is related to the energy as measured in the rest frame of the black hole and to the angle of emission relative to the radial vector by

$$E' = \gamma_f (1 - v_f \cos \theta) E. \quad (2.29)$$

No photons will emerge if the angle is greater than $\pi/2$. Therefore the instantaneous distribution is

$$\begin{aligned} \frac{d^2 N_\gamma^{\text{dir}}}{dE dt} &= 4\pi r_f^2 \left(\frac{E^2}{2\pi^2} \right) \int_0^1 d(\cos \theta) \cos \theta f(E, \cos \theta) \\ &\approx -\frac{2r_f^2 T_f E}{\pi \gamma_f} \ln \left(1 - e^{-E/2\gamma_f T_f} \right) \end{aligned} \quad (2.30)$$

where the second equality holds in the limit $\gamma_f \gg 1$. This limit is actually well satisfied for us and is used henceforth.

The instantaneous spectrum can be integrated over the remaining lifetime of the black hole straightforwardly. The radius and boost are both known in terms of the Hawking temperature T_H , and the time evolution of the latter is simply obtained from solving Eq. (2.3). For a black hole that disappears at time $t = 0$ we have

$$T_H(t) = -\frac{1}{8\pi} \left(\frac{m_{\text{P}}^2}{3\alpha_h t} \right)^{1/3}. \quad (2.31)$$

Here α_h is approximately 0.0044 for $T_H > 100$ GeV which includes the contribution from gravitons and neutrinos. Starting with a black hole whose temperature is T_0 we obtain the spectrum

$$\frac{dN_\gamma^{\text{dir}}}{dE} = \frac{360u_S^2}{\pi^5 d_f} \left(\frac{45\pi\alpha_h^{\text{eff}}}{2u_S^2 d_f} \right)^{1/4} \frac{m_{\text{P}}^2 T_f}{E^4} \sum_{n=1}^{\infty} \frac{1}{n} \int_0^{E/2\gamma_f(T_0)T_f} dx x^4 e^{-nx}. \quad (2.32)$$

Here we have ignored the small numerical difference between α_h^{eff} and α_h . In the high energy limit, namely, when $E \gg 2\gamma_f(T_0)T_f$, the summation yields the pure number $4(2\pi^6/315)$. Note the power-law behavior E^{-4} . This has important observational consequences.

2.6.2 π^0 decay photons

The neutral pion decays almost entirely into two photons: $\pi^0 \rightarrow \gamma\gamma$. In the rest frame of the pion the single photon Lorentz invariant distribution is

$$E \frac{d^3 N_\gamma}{d^3 p} = \frac{\delta(E - m_\pi/2)}{\pi m_\pi} \quad (2.33)$$

which is normalized to 2. This must be folded with the distribution of π^0 to obtain the total invariant photon distribution

$$E \frac{d^4 N_\gamma}{d^3 p dt} = \int_{m_\pi}^{\infty} dE_\pi \frac{d^2 N_{\pi^0}}{dE_\pi dt} \frac{1}{\pi m_\pi} \delta \left(\frac{EE_\pi - \mathbf{p} \cdot \mathbf{p}_\pi}{m_\pi} - \frac{m_\pi}{2} \right). \quad (2.34)$$

After integrating over angles we get

$$\frac{d^2 N_\gamma^{\pi^0}}{dE dt} = 2 \int_{E_{\min}}^{\infty} \frac{dE_\pi}{p_\pi} \frac{d^2 N_{\pi^0}}{dE_\pi dt} \quad (2.35)$$

where $E_{\min} = (E^2 + m_\pi^2/4)/E$. In the limit $E \gg m_\pi$ we can approximate $E_{\min} = E$ and evaluate $d^2 N_{\pi^0}/dE_\pi dt$ in the same way as photons. This leads to the relatively simple expression

$$\frac{d^2 N_\gamma^{\pi^0}}{dE dt} = \frac{4r_f^2 T_f^2}{\pi} \sum_{n=1}^{\infty} \frac{1}{n^2} e^{-nE/2\gamma_f T_f}. \quad (2.36)$$

The time-integrated spectrum is computed in the same way as for direct photons

$$\frac{dN_\gamma^{\pi^0}}{dE} = \frac{360u_S^2}{\pi^5 d_f} \left(\frac{45\pi\alpha_h^{eff}}{2u_S^2 d_f} \right)^{1/4} \frac{m_P^2 T_f}{E^4} \sum_{n=1}^{\infty} \frac{1}{n^2} \int_0^{E/2\gamma_f(T_0)T_f} dx x^3 e^{-nx}. \quad (2.37)$$

In the high energy limit, namely, when $E \gg 2\gamma_f(T_0)T_f$, the summation yields the pure number $2\pi^6/315$.

2.6.3 Instantaneous and integrated photon spectra

The instantaneous spectra of high energy gamma rays, arising from both direct emission and from π^0 decay, are plotted in figures 2.10 (for $T_f = 140$ MeV) and 2.11 (for $T_f = 100$ MeV). In each figure there are three curves corresponding to Hawking temperatures of 100 GeV, 1 TeV and 10 TeV. The photon spectra are essentially exponential above a few GeV with inverse slope $2\gamma_f(T_H)T_f \propto \sqrt{T_f T_H}$. If these instantaneous spectra could be measured they would tell us a lot about the equation of state, the viscosities, and how energy is processed from first Hawking radiation to final observed gamma rays. Even the time evolution of the black hole luminosity and temperature could be inferred.

The time integrated spectra for $T_f = 140$ MeV are plotted in figure 2.12 for three initial temperatures T_0 . A black hole with a Hawking temperature of 100 GeV has

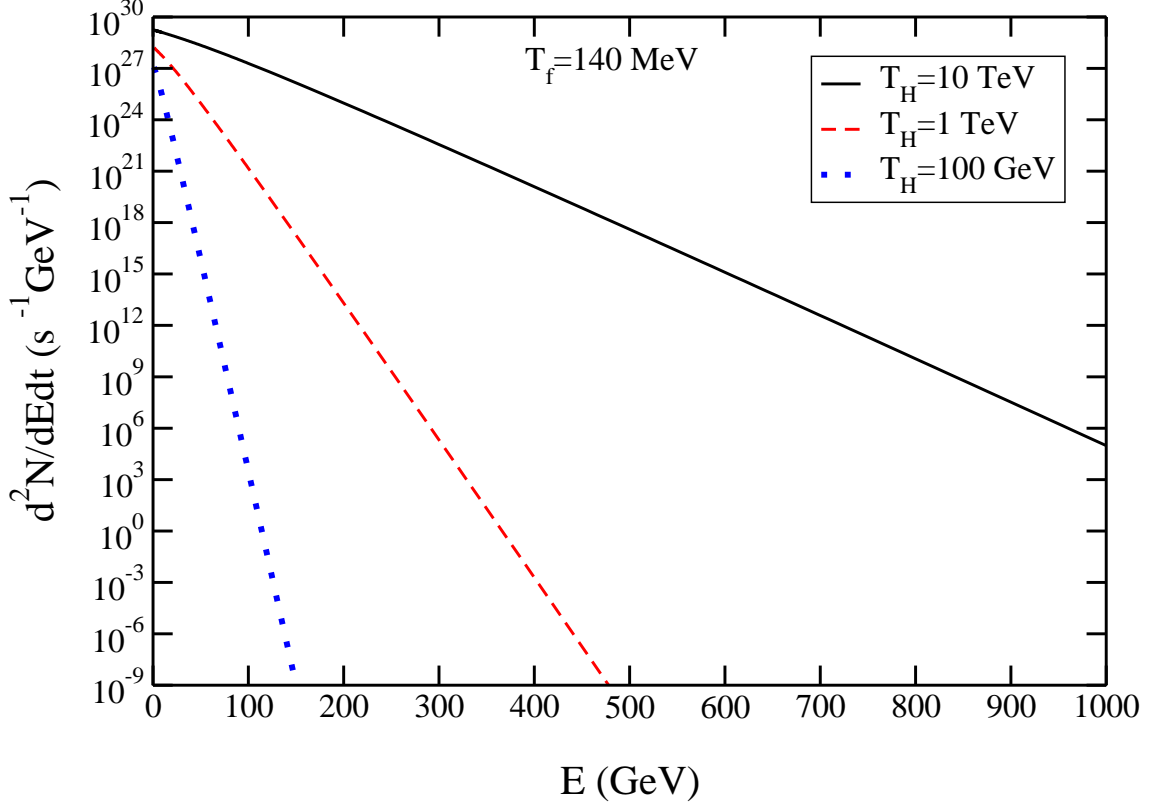


Figure 2.10: The instantaneous gamma ray spectrum for three different Hawking temperatures assuming $T_f = 140 \text{ MeV}$.

5.4 days to live, a black hole with a Hawking temperature of 1 TeV has 7.7 minutes to live, and a black hole with a Hawking temperature of 10 TeV has only 1/2 second to live. The high energy gamma ray spectra are represented by

$$\frac{dN}{dE} = \frac{m_{\text{P}}^2 T_f}{26E^4}. \quad (2.38)$$

It is interesting that the contribution from π^0 decay comprises 20% of the total while direct photons contribute the remaining 80%. The E^{-4} fall-off is the same as that obtained by Heckler [9], whereas Halzen *et al.* [43] and MacGibbon and Carr [8] obtained an E^{-3} fall-off on the basis of direct fragmentation of quarks and gluons with no fluid flow and no photosphere.

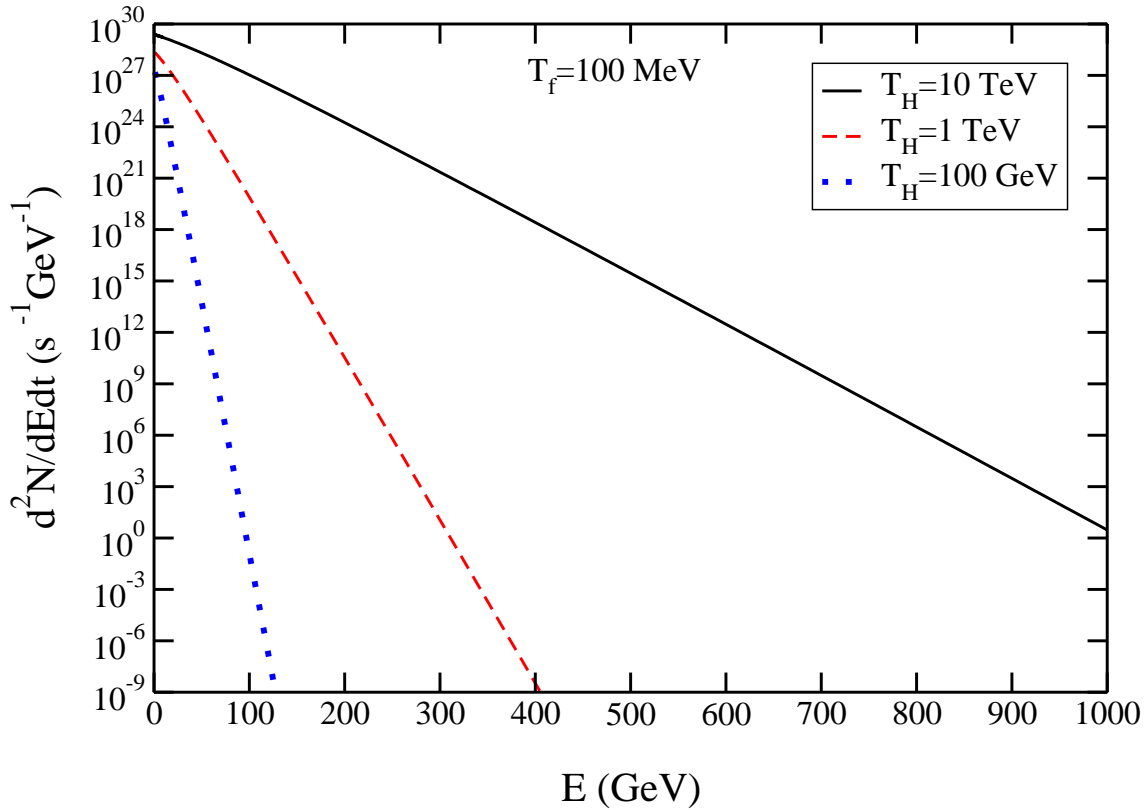


Figure 2.11: Same as figure 9 but with $T_f = 100$ MeV.

2.7 Observability of Gamma Rays

The most obvious way to observe the explosion of a microscopic black hole is by high energy gamma rays. We consider their contribution to the diffuse gamma ray spectrum in Sec. 2.7.1, and in Sec. 2.7.2 we study the systematics of a single identifiable explosion.

2.7.1 Diffuse spectra from the galactic halo

Suppose that microscopic black holes were distributed about our galaxy in some fashion. Unless we were fortunate enough to be close to one so that we could observe

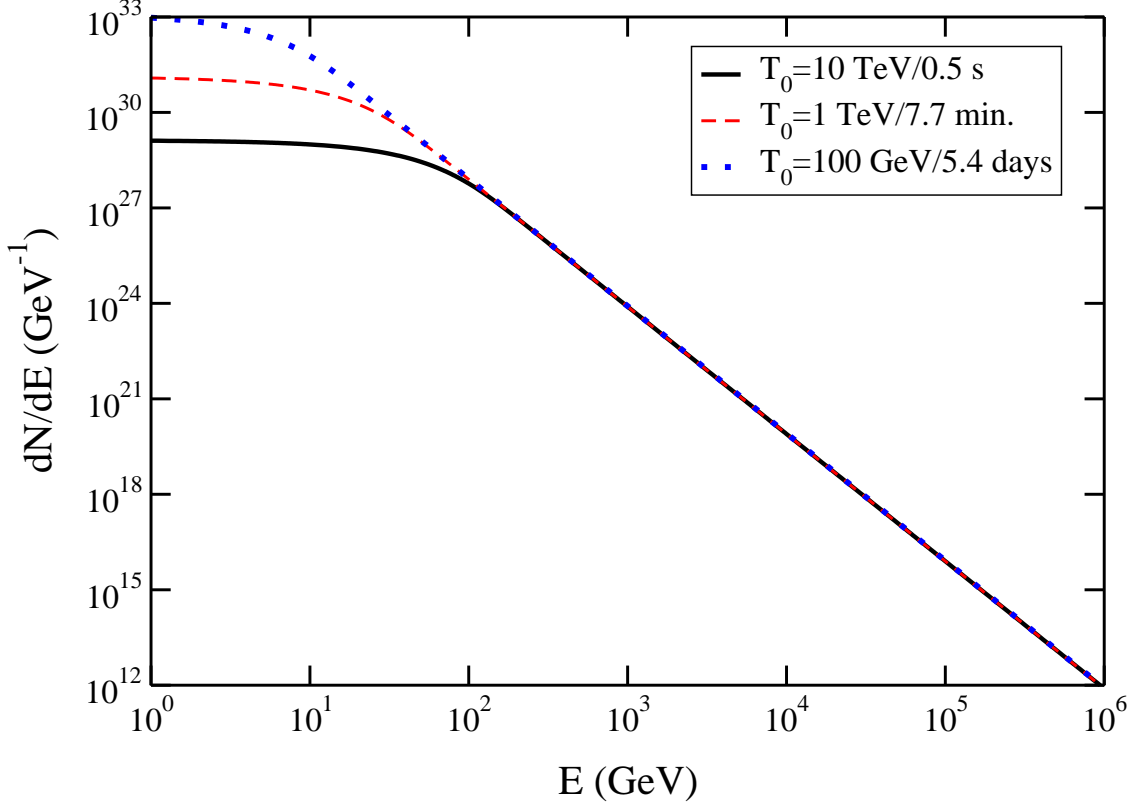


Figure 2.12: The time-integrated gamma ray spectrum starting from the indicated Hawking temperature. Here $T_f = 140$ MeV.

its demise, we would have to rely on their contribution to the diffuse background spectrum of high energy gamma rays.

The flux of photons with energy greater than 1 GeV at Earth can be computed from the results of Sec. 2.6 together with the knowledge of the rate density $\dot{\rho}(\mathbf{x})$ of exploding black holes. It is

$$\frac{d^3 N_{\text{Earth}}}{dE dA dt} = \frac{m_{\text{P}}^2 T_f}{26 E^4} \int d^3 x \frac{\dot{\rho}(\mathbf{x})}{4\pi d^2(\mathbf{x})} e^{-d(\mathbf{x})/\lambda_{\gamma\gamma}(E)} \quad (2.39)$$

where $d(\mathbf{x})$ is the distance from the black hole to the Earth. The exponential decay is due to absorption of the gamma ray by the black-body radiation [44]. The mean free path $\lambda_{\gamma\gamma}(E)$ is highly energy dependent. It has a minimum of about 1 kpc around 1

PeV, and is greater than 10^5 kpc for energies less than 100 TeV.

We need a model for the rate density of exploding black holes. We shall assume they are distributed in the same way as the matter comprising the halo of our galaxy. Thus we take

$$\dot{\rho}(\mathbf{x}) = \dot{\rho}_0 \frac{R_c^2}{x^2 + y^2 + q^2 z^2 + R_c^2} \quad (2.40)$$

where the galactic plane is the $x - y$ plane, R_c is the core radius, and q is a flattening parameter. For numerical calculations we shall take the core radius to be 10 kpc. The Earth is located a distance $R_E = 8.5$ kpc from the center of the galaxy and lies in the galactic plane. Therefore $d^2 = (x - R_E)^2 + y^2 + z^2$.

The last remaining quantity is the normalization of the rate density $\dot{\rho}_0$. This is, of course, unknown since no one has ever knowingly observed a black hole explosion. The first observational limit was determined by Page and Hawking [45]. They found that the local rate density $\dot{\rho}_{\text{local}}$ is less than 1 to 10 per cubic parsec per year on the basis of diffuse gamma rays with energies on the order of 100 MeV. This limit has not been lowered very much during the intervening twenty-five years. For example, Wright [46] used EGRET data to search for an anisotropic high-latitude component of diffuse gamma rays in the energy range from 30 MeV to 100 GeV as a signal for steady emission of microscopic black holes. He concluded that $\dot{\rho}_{\text{local}}$ is less than about 0.4 per cubic parsec per year. (For an alternative point of view on the data see [47].) In our numerical calculations we shall assume a value $\dot{\rho}_0 = 1 \text{ pc}^{-3} \text{ yr}^{-1}$ corresponding to $\dot{\rho}_{\text{local}} \approx 0.58 \text{ pc}^{-3} \text{ yr}^{-1}$. This makes for easy scaling. Estimating the quantity of dark matter in our galaxy as $M_{\text{halo}}/\rho_{0, \text{halo}} = 4.7 \times 10^4 \text{ kpc}^3$ means that we could have up to 47×10^{12} microscopic black hole explosions per year in our galaxy.

Figure 2.13 shows the calculated flux at Earth, multiplied by E^4 . Of course this curve would be flat if it were not for absorption on the microwave background radiation. There is a relative suppression of three orders of magnitude centered between 10^{15} and 10^{16} eV. This means that it is unlikely to observe exploding black holes in the gamma ray spectrum above 10^{14} eV. Even below that energy it is unlikely because they have not been observed at energies on the order of 100 MeV, and the spectrum

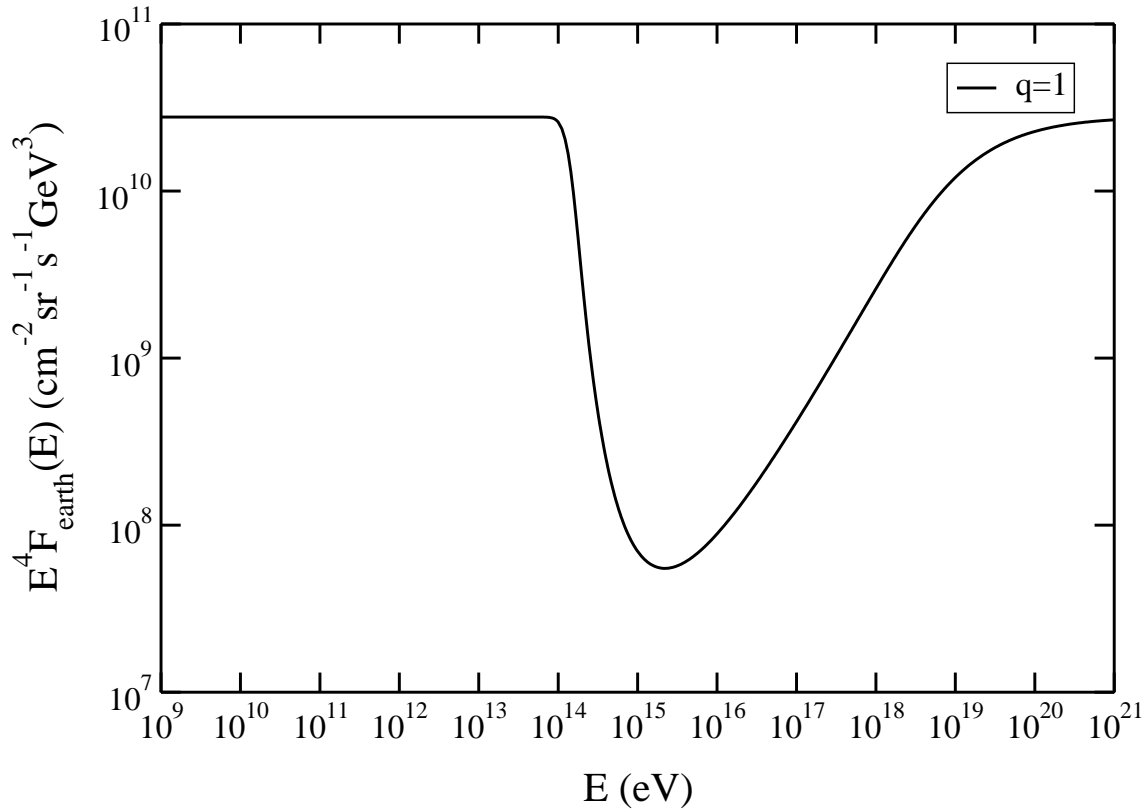


Figure 2.13: The flux of diffuse gamma rays coming from our galactic halo. The normalization is $\dot{\rho}_0 = 1 \text{ pc}^{-3} \text{ yr}^{-1}$. The halo is assumed to be spherically symmetric, $q = 1$; the results for a flattened halo with $q = 2$ are very similar.

falls faster than the primary cosmic ray spectrum $\propto E^{2.7}$. The curve displayed in figure 2.13 assumes a spherical halo, $q = 1$, but there is hardly any difference when the halo is flattened to $q = 2$.

2.7.2 Point source systematics

Given the unfavorable situation for observing the effects of exploding microscopic black holes on the diffuse gamma ray spectrum, we now turn to the consequences for observing one directly. How far away could one be seen? Let us call that distance d_{max} .

We assume that $d_{\max} < \lambda_{\gamma\gamma}$ for simplicity, although that assumption can be relaxed if necessary. Let A_{det} denote the effective area of the detector that can measure gamma rays with energies equal to or greater than E_{\min} . The average number of gamma rays detected from a single explosion a distance d_{\max} away is

$$\langle N_{\gamma}(E > E_{\min}) \rangle = \frac{A_{\text{det}}}{4\pi d_{\max}^2} \int_{E_{\min}}^{\infty} \frac{dN_{\gamma}}{dE} dE = \frac{A_{\text{det}}}{4\pi d_{\max}^2} \frac{m_{\text{P}}^2 T_f}{78 E_{\min}^3}. \quad (2.41)$$

Obviously we should have E_{\min} as small as possible to get the largest number, but it cannot be so small that the simple E^{-4} behavior of the emission spectrum is invalid. See figure 2.12.

A rough approximation to the number distribution of detected gamma rays is a Poisson distribution.

$$P(N_{\gamma}) = \frac{\langle N_{\gamma} \rangle^{N_{\gamma}}}{N_{\gamma}!} e^{-\langle N_{\gamma} \rangle} \quad (2.42)$$

The exact form of the number distribution is not so important. What is important is that when $\langle N_{\gamma}(E > E_{\min}) \rangle > 1$ we should expect to see multiple gamma rays coming from the same point in the sky. Labeling these gamma rays according to the order in which they arrive, 1, 2, 3, etc. we would expect their energies to increase with time: $E_1 < E_2 < E_3 < \dots$. Such an observation would be remarkable, possibly unique, because astrophysical sources normally cool at late times. This would directly reflect the increasing Hawking temperature as the black hole explodes and disappears.

It is interesting to know how the average gamma ray energy increases with time. Using Eqs. (2.30) and (2.36) we compute the average energy of direct photons to be $4\gamma_f T_f \zeta(4)/\zeta(3)$ and the average energy of π^0 decay photons to be one-half that. The ratio of direct to decay photons turns out to be π . Therefore the average gamma ray energy is $3.17\gamma_f(t)T_f$. This average is plotted in figure 2.14 for $10^5 > t > 10^{-5}$ seconds. The average gamma ray energy ranges from about 4 to 160 GeV.

The maximum distance can now be computed. Using some characteristic numbers we find

$$d_{\max} \approx 150 \sqrt{\frac{A_{\text{det}}}{1 \text{ km}^2}} \left(\frac{10 \text{ GeV}}{E_{\min}} \right)^{3/2} \text{ pc}. \quad (2.43)$$

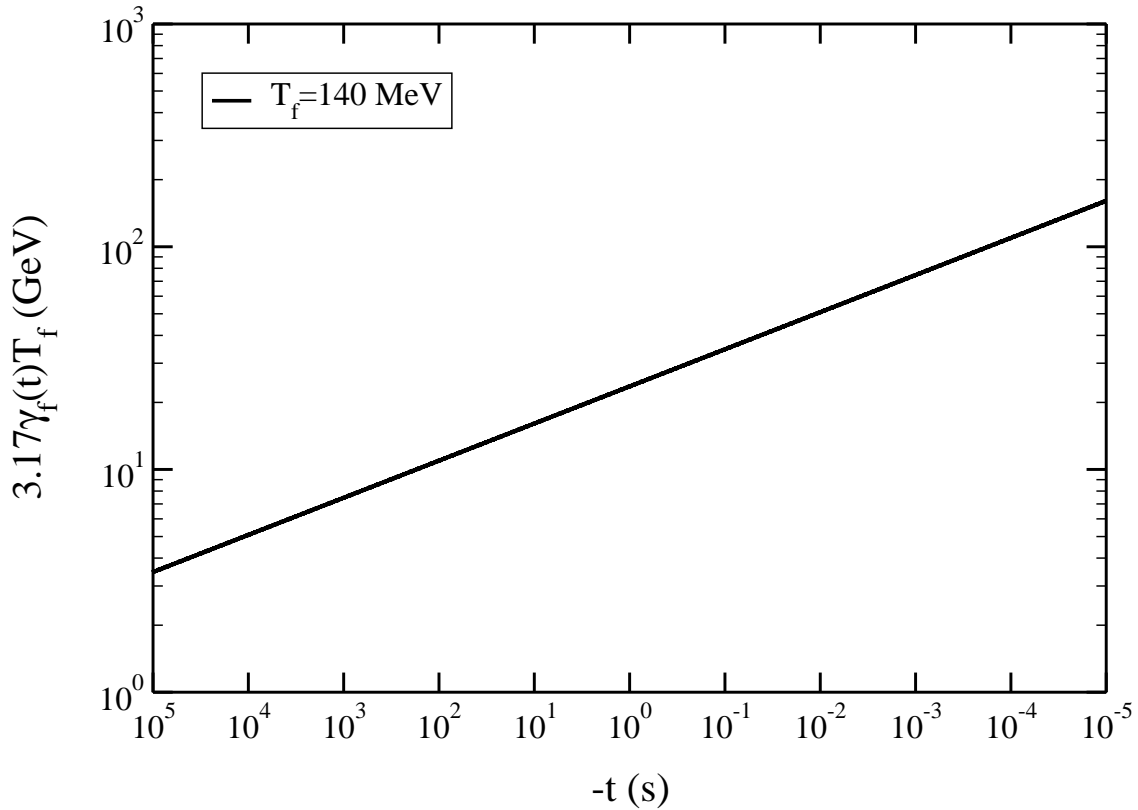


Figure 2.14: The average gamma ray energy as a function of the remaining lifetime of the black hole. The times spanned correspond to approximately $400 \text{ GeV} < T_H < 200 \text{ TeV}$.

If we take the local rate density of explosions to be $0.4 \text{ pc}^{-3} \text{ yr}^{-1}$ then within 150 pc of Earth there would be 5×10^6 explosions per year. These would be distributed isotropically in the sky. Still, it suggests that the direct observation of exploding black holes is feasible if they are near to the inferred upper limit to their abundance in our neighborhood. We should point out that a search for 1 s bursts of ultrahigh energy gamma rays from point sources by CYGNUS has placed an upper limit of $8.5 \times 10^5 \text{ pc}^{-3} \text{ yr}^{-1}$ [48]. However, as we have seen in figure 2.14 and elsewhere, this is not what should be expected if our calculations bear any resemblance to reality. Rather than a burst, the luminosity and average gamma ray energy increase monotonically

over a long period of time.

2.8 Neutrino Emission

In this section we focus on high energy neutrino emission from black holes with Hawking temperatures greater than 100 GeV and corresponding masses less than 10^8 kg. It is at these and higher temperatures that new physics will arise. Such a study is especially important in the context of high energy neutrino detectors under construction or planned for the future. Previous notable studies in this area have been carried out by MacGibbon and Webber [7, 49] and by Halzen, Keszthelyi and Zas [50], who calculated the instantaneous and time-integrated spectra of neutrinos arising from the decay of quark and gluon jets.

The source of neutrinos in the viscous fluid picture is quite varied. Neutrinos should stay in thermal equilibrium, along with all other elementary particles, when the local temperature is above 100 GeV. The reason is that at energies above the electroweak scale of 100 GeV neutrinos should have interaction cross sections similar to those of all other particles. Thus the neutrino-sphere, where the neutrinos decouple, ought to exist where the local temperature falls below 100 GeV. The spectra of these direct neutrinos are calculated in Sec. 2.8.1.

Neutrinos also come from decays involving pions and muons. The relevant processes are (i) a thermal pion decays into a muon and muon-neutrino, followed by the muon decay $\mu \rightarrow e\nu_e\nu_\mu$, and (ii) a thermal muon decays in the same way. The spectra of neutrinos arising from pion decay are calculated in Sec. 2.8.2 while those arising from direct or indirect muon decay are calculated in Sec. 2.8.3.

The spectra from all of these sources are compared graphically in Sec. 2.9. We also compare with the spectra of neutrinos emitted directly as Hawking radiation without any subsequent interactions. The main result is that the time-integrated direct Hawking spectrum falls at high energy as E^{-3} whereas the time-integrated neutrino spectrum coming from a fluid or from pion and muon decays all fall as E^{-4} . Thus

the fluid picture predicts more neutrinos at lower energies than the direct Hawking emission picture. If a microscopic black hole is near enough the instantaneous spectrum could be measured, and its shape and magnitude would provide information on the number of degrees of freedom in the nature on mass scales exceeding 100 GeV.

2.8.1 Directly Emitted Neutrinos

In this section we first review the emission of neutrinos by the Hawking mechanism unmodified by any rescattering. Then we estimate the spectra of neutrinos which rescatter in the hot matter. The last scattering surface should be represented approximately by that radius where the temperature has dropped to 100 GeV. The reason is that neutrinos with energies much higher than that have elastic and inelastic cross sections that are comparable to the cross sections of quarks, gluons, electrons, muons, and tau leptons. Much below that energy the relevant cross sections are greatly suppressed by the mass of the exchanged vector bosons, the W and Z. Furthermore, the electroweak symmetry is broken below temperatures of this order, making it natural to place the last scattering surface there. A much better treatment would require the solution of transport equations for the neutrinos, an effort that is perhaps not yet justified. All the formulas in this section refer to one flavor of neutrino. Our current understanding is that there are three flavors, each available as a particle or antiparticle. The sum total of all neutrinos would then be a factor of 6 larger than the formulas presented here.

Direct neutrinos

The emission of neutrinos by the Hawking mechanism is usually calculated on the basis of detailed balance. It involves a thermal flux of neutrinos incident on a black hole. The Dirac equation is solved and the absorption coefficient is computed. This involves numerical calculations [28, 29, 51]. The number emitted per unit time per

unit energy is given by

$$\frac{d^2 N_\nu^{\text{dir}}}{dE dt} = \frac{\Gamma_\nu}{2\pi} \frac{1}{\exp(E/T_H) + 1}, \quad (2.44)$$

where Γ_ν is an energy-dependent absorption coefficient. There is no simple analytic formula for it. For our purposes it is sufficient to parametrize the numerical results.

A fair representation is given by

$$\Gamma_\nu = \frac{27}{64\pi^2} \frac{E^2}{T_H^2} \left(0.075 + \frac{0.925}{\exp(5 - aE/T_H) + 1} \right), \quad (2.45)$$

and $a \approx 1.607$. The exact expression has very small amplitude oscillations arising from the essentially black disk character of the black hole. The parametrized form does not have these oscillations, but otherwise is accurate to within about 5%.

If there are no new degrees of freedom present in nature, other than those already known, then the time dependence of the black hole mass and temperature are easily found. The relationship between the time and the temperature [Eq. (2.31)] allows us to compute the time-integrated spectrum, starting from the moment when $T_H = T_0$. There is a one-dimensional integral to be done numerically.

$$\frac{dN_\nu^{\text{dir}}}{dE} = \frac{27m_{\text{P}}^2}{16(4\pi)^6 \alpha_h E^3} \int_0^{E/T_0} dx \frac{x^4}{\exp(x) + 1} \left(0.075 + \frac{0.925}{\exp(5 - ax) + 1} \right) \quad (2.46)$$

In the high energy limit, meaning $E \gg T_0$, the upper limit can be taken to infinity with the result

$$\frac{dN_\nu^{\text{dir}}}{dE} \rightarrow \frac{29.9m_{\text{P}}^2}{(4\pi)^6 \alpha_h E^3} \approx \frac{m_{\text{P}}^2}{565E^3}. \quad (2.47)$$

Direct neutrinos from an expanding fluid

Neutrinos emitted from the decoupling surface have a Fermi distribution in the local rest frame of the fluid. The phase space density is

$$f(E') = \frac{1}{e^{E'/T_\nu} + 1}. \quad (2.48)$$

The decoupling temperature of neutrinos is denoted by T_ν . The energy appearing here is related to the energy as measured in the rest frame of the black hole and to

the angle of emission relative to the radial vector by

$$E' = \gamma_\nu(1 - v_\nu \cos \theta)E. \quad (2.49)$$

No neutrinos will emerge if the angle is greater than $\pi/2$. Therefore the instantaneous distribution is

$$\begin{aligned} \frac{d^2 N_\nu^{\text{fluid}}}{dE dt} &= 4\pi r_\nu^2 \left(\frac{E^2}{2\pi^2} \right) \int_0^1 d(\cos \theta) \cos \theta f(E, \cos \theta) = \frac{r_\nu^2 T_\nu}{\pi u_\nu} E \sum_{n=1}^{\infty} \frac{(-1)^{n+1}}{n} \\ &\left\{ \left(1 - \frac{T_\nu}{nu_\nu E} \right) \exp[-nE(\gamma_\nu - u_\nu)/T_\nu] + \frac{T_\nu}{nu_\nu E} \exp[-nE\gamma_\nu/T_\nu] \right\}, \end{aligned} \quad (2.50)$$

where r_ν is the radius of the decoupling surface and $u = v\gamma$. Integration over the energy gives the luminosity (per neutrino).

We need to know how the radius and radial flow velocity at neutrino decoupling depend on the Hawking temperature or, equivalently, the black hole mass; we have already argued that the neutrino temperature at decoupling is about $T_\nu = 100$ GeV. We also know the relation between r_ν and u_ν from Eq. (2.20):

$$r_\nu = \frac{1}{4\pi T_H} \left(\frac{u_\nu}{u_S} \right)^3. \quad (2.51)$$

The final piece of information is to recognize that each type of neutrino will contribute $7/8$ effective bosonic degree of freedom to the total number of effective bosonic degrees of freedom in the energy density of the fluid. After integrating the instantaneous neutrino energy spectrum to obtain its luminosity we equate it with the appropriate fraction of the total luminosity.

$$L_\nu^{\text{fluid}} = \frac{7}{8} \frac{\pi^3 r_\nu^2 T_\nu^4}{90} \frac{3 - v_\nu}{(1 - v_\nu)^3 \gamma_\nu^4} = \frac{7/8}{106.75} L^{\text{Hawking}} \quad (2.52)$$

where

$$L^{\text{Hawking}} = 64\pi^2 \alpha_h^{\text{eff}} T_H^2. \quad (2.53)$$

The number 106.75 counts all effective bosonic degrees of freedom in the standard model excepting gravitons. Here α_h^{eff} does not include the contribution from gravitons. This results in an equation which determines v , equivalently u , in terms of the

Hawking temperature:

$$\frac{(3 - v_\nu)v_\nu^4 u_\nu^2}{(1 - v_\nu)^3} = 2^{13} \frac{45\pi}{427} \alpha_h^{eff} u_S^6 \left(\frac{T_H}{T_\nu}\right)^4 = C \left(\frac{T_H}{T_\nu}\right)^4. \quad (2.54)$$

Numerically the constant $C = 1.14 \times 10^{-5}$.

We are interested in black holes with $T_H > T_\nu = 100$ GeV. The corresponding range of neutrino-sphere flow velocities corresponds to $0.2 < u_\nu < \infty$. There is no simple analytical expression for the solution to Eq. (2.54) for this wide range of the variable. At asymptotically high temperatures the left side has the limit $16u_\nu^8$. For intermediate values the left side may be approximated by $22u_\nu^7$. We approximate the left side by the former for $u_\nu > 11/8$ and by the latter for $0.2 < u_\nu < 11/8$. Thus

$$u_\nu = \left(\frac{CT_H^4}{22T_\nu^4}\right)^{1/7} \quad \text{for } u_\nu < 11/8 \quad (2.55)$$

$$u_\nu = \left(\frac{CT_H^4}{16T_\nu^4}\right)^{1/8} \quad \text{for } u_\nu > 11/8. \quad (2.56)$$

This approximation is valid to better than 20% within the range mentioned.

The time-integrated spectrum can be calculated on the basis of Eqs. (2.50), (2.31), (2.51) and either (2.54), which is exact, or with the approximation of (2.55-56) which results in

$$\begin{aligned} \frac{dN_\nu^{\text{fluid}}}{dE} &= \frac{m_p^2 T_\nu E}{2^{13} \pi^6 \alpha_h u_S^6} \sum_{n=1}^{\infty} (-1)^{n+1} \\ &\times \left\{ \left(\frac{C}{22T_\nu^4}\right)^{5/7} \int_{T_0}^{T_\star} \frac{dT_H}{T_H^{22/7}} \frac{\exp[-n\frac{E}{T_\nu}(\gamma_1 - u_1)]}{n} \right. \\ &+ \frac{T_\nu}{E} \left(\frac{C}{22T_\nu^4}\right)^{4/7} \int_{T_0}^{T_\star} \frac{dT_H}{T_H^{26/7}} \left(\frac{\exp[-n\frac{E}{T_\nu}\gamma_1]}{n^2} - \frac{\exp[-n\frac{E}{T_\nu}(\gamma_1 - u_1)]}{n^2} \right) \\ &+ \left(\frac{C}{16T_\nu^4}\right)^{5/8} \int_{T_\star}^{\infty} \frac{dT_H}{T_H^{7/2}} \frac{\exp[-n\frac{E}{T_\nu}(\gamma_2 - u_2)]}{n} \\ &\left. + \frac{T_\nu}{E} \left(\frac{C}{16T_\nu^4}\right)^{4/8} \int_{T_\star}^{\infty} \frac{dT_H}{T_H^4} \left(\frac{\exp[-n\frac{E}{T_\nu}\gamma_2]}{n^2} - \frac{\exp[-n\frac{E}{T_\nu}(\gamma_2 - u_2)]}{n^2} \right) \right\}, \quad (2.57) \end{aligned}$$

where $T_\star = 2(\frac{11}{8})^2 T_\nu / C^{1/4}$. What is interesting here is the high energy limit, $E \gg 10T_\nu = 1$ TeV. This is determined wholly by the first of the two exponentials in Eq.

(2.50) with the coefficient of 1. Using also Eqs. (2.31), (2.51) and (2.55) we find the limit

$$\frac{dN_\nu^{\text{fluid}}}{dE} \rightarrow \frac{4185\zeta(6)C^{1/4}m_{\text{P}}^2T_\nu}{854\pi^5 E^4} \approx \frac{m_{\text{P}}^2T_\nu}{1040E^4}. \quad (2.58)$$

Here we have ignored the small numerical differences between α_h^{eff} and α_h . This E^{-4} spectrum is characteristic of all neutrino sources in the viscous fluid description of the microscopic black hole wind.

2.8.2 Neutrinos from Pion Decay

Muon-type neutrinos will come from the decays of charged pions, namely $\pi^+ \rightarrow \mu^+ \nu_\mu$ and $\pi^- \rightarrow \mu^- \bar{\nu}_\mu$. In what follows we calculate the spectrum of muon neutrinos; the spectrum for muon anti-neutrinos is of course identical.

In the rest frame of the decaying pion the muon and the neutrino have momentum q determined by energy and momentum conservation.

$$m_\pi = q + \sqrt{m_\mu^2 + q^2} \quad (2.59)$$

Numerically $q = 0.2134m_\pi$. In the pion rest frame the spectrum for the neutrino, normalized to one, is

$$E' \frac{d^3 N_\nu^\pi}{d^3 p'} = \frac{\delta(E' - q)}{4\pi q}. \quad (2.60)$$

The Lorentz invariant rate of emission is obtained by folding together the spectrum with the rate of emission of π^+ .

$$E \frac{d^4 N_\nu^\pi}{d^3 p dt} = \int_{m_\pi}^\infty dE_\pi \left(\frac{d^2 N_\pi}{dE_\pi dt} \right) \frac{1}{4\pi q} \delta\left(\frac{EE_\pi - \mathbf{p} \cdot \mathbf{p}_\pi}{m_\pi} - q \right) \quad (2.61)$$

The spectrum of pions is computed in the same way as the spectrum of direct neutrinos from the expanding fluid in Sec. 2.8.1 but with one difference and one simplification. The difference is that the pion has a Bose distribution as opposed to the Fermi distribution of the neutrino. The simplification is that the fluid at pion decoupling has a highly relativistic flow velocity with $u_f \approx \gamma_f \gg 1$. The analog to Eq. (2.50) is

$$\frac{d^2 N_\pi}{dE_\pi dt} = -\frac{r_f^2 T_f p_\pi}{\pi \gamma_f} \ln\left(1 - e^{-E_\pi/2\gamma_f T_f}\right). \quad (2.62)$$

The instantaneous energy spectrum of the neutrino is reduced to a single integral.

$$\frac{d^2 N_\nu^\pi}{dE dt} = -\frac{m_\pi T_f r_f^2}{2\pi q \gamma_f} \int_{E_{\min}}^{\infty} dE_\pi \ln \left(1 - e^{-E_\pi/2\gamma_f T_f} \right) \quad (2.63)$$

Here $E_{\min} = m_\pi(E^2 + q^2)/2Eq$ is the minimum pion energy that will produce a neutrino with energy E . We are interested only in high energy neutrinos with $E \gg m_\pi$, in which case $E_{\min} = m_\pi E/2q$ is an excellent approximation. The integral can also be expressed as an infinite summation

$$\frac{d^2 N_\nu^\pi}{dE dt} = \frac{m_\pi r_f^2 T_f^2}{\pi q} \sum_{n=1}^{\infty} \frac{1}{n^2} \exp \left(-\frac{nm_\pi E}{4\gamma_f T_f q} \right) \quad (2.64)$$

When $E \gg \gamma_f T_f$ only the first term in the summation in Eq. (2.64) is important.

The instantaneous spectrum is easily integrated over time because the flow velocity at pion decoupling is highly relativistic. The spectrum arising from the last moments when the Hawking temperature exceeds T_0 is

$$\frac{dN_\nu^\pi}{dE} = \frac{64u_s^4 q^3}{\pi^6 \alpha_h m_\pi^3} \left(\frac{45\pi \alpha_h^{eff}}{2u_s^2 d_f} \right)^{5/4} \frac{m_{\text{P}}^2 T_f}{E^4} \sum_{n=1}^{\infty} \frac{1}{n^2} \int_0^{m_\pi E/4\gamma_f(T_0)T_f q} dx x^3 e^{-nx}. \quad (2.65)$$

In the limit that $E \gg \gamma_f(T_0)T_f$ the upper limit on the integral may be taken to infinity. After ignoring the small numerical difference between α_h^{eff} and α_h , we can express the result in terms of the constant C as:

$$\frac{dN_\nu^\pi}{dE} \rightarrow \frac{464\pi}{427} \left(\frac{q}{m_\pi} \right)^3 \left(\frac{203C}{2d_f} \right)^{1/4} \frac{m_{\text{P}}^2 T_f}{E^4} \approx \frac{m_{\text{P}}^2 T_f}{300E^4}. \quad (2.66)$$

This is much smaller than the direct neutrino emission from the fluid because the neutrino decoupling temperature T_ν is much greater than the pion decoupling temperature T_f . Here α_h^{eff} does not include gravitons and neutrinos.

2.8.3 Neutrinos from Muon Decay

Muons can be emitted directly or indirectly by the weak decay of pions: $\pi^- \rightarrow \mu^- \nu_e \bar{\nu}_\mu$ plus the charge conjugated decay. Both sources contribute to the neutrino spectrum.

The invariant distribution of the electron neutrino (to be specific) in the rest frame of the muon is

$$E' \frac{d^3 N_{\nu_e}}{d^3 p'} = \frac{4}{\pi m_\mu^4} (3m_\mu - 4E') E' \quad (2.67)$$

where the electron mass has been neglected in comparison to the muon mass. This distribution is used in place of the delta-function distribution of Eq. (2.60) for both direct and indirect muons, as evaluated in the following two subsections.

Neutrinos from direct muons

The instantaneous spectrum of ν_e , $\bar{\nu}_e$, ν_μ or $\bar{\nu}_\mu$ arising from muons in thermal equilibrium until the decoupling temperature of T_f can be computed by folding together the spectrum of muons together with the decay spectrum of neutrinos in the same way as Eq. (2.61) was obtained. Using Eqs. (2.62) and (2.67) results in

$$\begin{aligned} \frac{d^2 N_\nu^{\text{dir } \mu}}{dE dt} &= \frac{2r_f^2 T_f E}{3\pi\gamma_f} \sum_{n=1}^{\infty} \left\{ -\text{Ei} \left(-\frac{nE}{2\gamma_f T_f} \right) \left[9 \frac{nE}{2\gamma_f T_f} + 2 \left(\frac{nE}{2\gamma_f T_f} \right)^2 \right] \right. \\ &\quad \left. + \exp \left(-\frac{nE}{2\gamma_f T_f} \right) \left[\frac{10\gamma_f T_f}{nE} - 7 - 2 \frac{nE}{\gamma_f T_f} \right] \right\}, \end{aligned} \quad (2.68)$$

where Ei is the exponential-integral function. In the high energy limit, defined here by $E \gg 2\gamma_f T_f$, the spectrum simplifies to

$$\frac{d^2 N_\nu^{\text{dir } \mu}}{dE dt} = \frac{2r_f^2 T_f E}{3\pi\gamma_f} \exp \left(-\frac{E}{2\gamma_f T_f} \right). \quad (2.69)$$

The time-integrated spectrum can be calculated in a fashion analogous to that followed in Sec. 2.8.2. Thus

$$\begin{aligned} \frac{dN_\nu^{\text{dir } \mu}}{dE} &= \frac{16u_s^4}{3\pi^6\alpha_h} \left(\frac{45\pi\alpha_h^{eff}}{2u_s^2 d_f} \right)^{5/4} \frac{m_{\text{P}}^2 T_f}{E^4} \\ &\quad \times \sum_{n=1}^{\infty} \int_0^{E/2\gamma_f(T_0)T_f} \left\{ -\text{Ei} \left(-\frac{nE}{2\gamma_f T_f} \right) \left[9 \frac{nE}{2\gamma_f T_f} + 2 \left(\frac{nE}{2\gamma_f T_f} \right)^2 \right] \right. \\ &\quad \left. + \exp \left(-\frac{nE}{2\gamma_f T_f} \right) \left[\frac{10\gamma_f T_f}{nE} - 7 - 2 \frac{nE}{\gamma_f T_f} \right] \right\}. \end{aligned} \quad (2.70)$$

In the high energy limit this simplifies to

$$\frac{dN_\nu^{\text{dir } \mu}}{dE} \rightarrow \frac{11745}{488\pi^5 d_f} [225\zeta(7) - 217\zeta(6)] \left(\frac{203C}{2d_f} \right)^{1/4} \frac{m_{\text{P}}^2 T_f}{E^4} \approx \frac{m_{\text{P}}^2 T_f}{250E^4}. \quad (2.71)$$

Neutrinos from indirect muons

The spectrum of neutrinos coming from the decay of muons which themselves came from the decay of pions proceeds exactly as in the previous subsection, but with the replacement of the direct muon energy spectrum by the indirect muon energy spectrum. In the rest frame of the pion the muon distribution is

$$E' \frac{d^3 N_\mu^\pi}{d^3 p'} = \frac{\sqrt{m_\mu^2 + q^2}}{4\pi q^2} \delta(p' - q), \quad (2.72)$$

which is the finite mass version of Eq. (2.60). Folding together this spectrum with the spectrum of pions (2.62) yields the spectrum of indirect muons.

$$\frac{d^2 N_\mu^\pi}{dE dt} = \frac{m_\pi r_f^2 T_f^2}{\pi q} \sum_{n=1}^{\infty} \frac{1}{n^2} \exp\left(-\frac{nm_\pi E}{4\gamma_f T_f \sqrt{m_\mu^2 + q^2}}\right) \quad (2.73)$$

This spectrum is now folded with the decay distribution of neutrinos to obtain

$$\begin{aligned} \frac{d^2 N_\nu^{\text{indir } \mu}}{dE dt} &= \frac{m_\pi r_f^2 T_f^2}{3\pi q} \sum_{n=1}^{\infty} \frac{1}{n^2} \left\{ \text{Ei}(-nx) \left(5 - \frac{27}{6} n^2 x^2 - \frac{2}{3} n^3 x^3 \right) \right. \\ &\quad \left. - \left(-\frac{19}{6} + \frac{23}{6} nx + \frac{2}{3} n^2 x^2 \right) e^{-nx} \right\}_{x_-}^{x_+} \end{aligned} \quad (2.74)$$

where

$$x_\pm = \frac{m_\pi E}{2\gamma_f T_f} \left[\frac{(m_\mu^2 + q^2)^{1/2} \pm q}{m_\mu^2} \right]. \quad (2.75)$$

The high energy limit $E \gg \gamma_f T_f$ is

$$\frac{d^2 N_\nu^{\text{indir } \mu}}{dE dt} \rightarrow \frac{m_\pi r_f^2 T_f^2}{3\pi q} \left[\frac{e^{-x_-}}{x_-^2} - \frac{e^{-x_+}}{x_+^2} \right]. \quad (2.76)$$

The integral over time can be done in the usual way. The resulting expression is

$$\begin{aligned} \frac{dN_\nu^{\text{indir } \mu}}{dE} &= \frac{4u_s^4}{3\pi^6 \alpha_h m_\pi^3 q} \left(\frac{45\pi \alpha_h^{eff}}{2u_s^2 d_f} \right)^{5/4} \frac{m_p^2 T_f}{E^4} \\ &\quad \times \sum_{n=1}^{\infty} \frac{1}{n^2} \left\{ \left(\frac{m_\mu^2}{(m_\mu^2 + q^2)^{1/2} - q} \right)^4 \int_0^{x_0^-} dx_- x_-^3 \right. \end{aligned}$$

$$\begin{aligned}
& \left[\exp(-nx_-) \left(-\frac{19}{6} + \frac{23}{6}nx_- + \frac{4}{6}n^2x_-^2 \right) - Ei(-nx_-) \left(5 - \frac{27}{6}n^2x_-^2 - \frac{4}{6}n^3x_-^3 \right) \right] \\
& - \left(\frac{m_\mu^2}{(m_\mu^2 + q^2)^{1/2} + q} \right)^4 \int_0^{x_{0+}} dx_+ x_+^3 \\
& \left[\exp(-nx_+) \left(-\frac{19}{6} + \frac{23}{6}nx_+ + \frac{4}{6}n^2x_+^2 \right) - Ei(-nx_+) \left(5 - \frac{27}{6}n^2x_+^2 - \frac{4}{6}n^3x_+^3 \right) \right] \Bigg\}, \tag{2.77}
\end{aligned}$$

where $x_{0\pm} = x_\pm(T_0)$. The high energy limit is simple and of the familiar form $1/E^4$.

$$\frac{dN_\nu^{\text{indir } \mu}}{dE} \rightarrow \frac{174\pi}{2989d_f} \left(\frac{203C}{2d_f} \right)^{1/4} \frac{\sqrt{m_\mu^2 + q^2} (m_\mu^2 + 2q^2) m_P^2 T_f}{m_\pi^3 E^4} \approx \frac{m_P^2 T_f}{1250E^4} \tag{2.78}$$

2.9 Comparison of Neutrino Sources

In this section we compare the different sources of neutrinos that were computed in the previous sections. All the figures presented display one type of neutrino or anti-neutrino. That type should be clear from the context. For example, equal numbers of ν_e , $\bar{\nu}_e$, ν_μ , $\bar{\nu}_\mu$, ν_τ , and $\bar{\nu}_\tau$ are produced as Hawking radiation and by direct emission by the fluid at the neutrino decoupling temperature T_ν . Only electron and muon type neutrinos are produced by muon decay, and only muon type neutrinos by pion decay. These differences could help to distinguish the decay of a microscopic black hole from other neutrino sources if one happened to be within a detectable distance.

The instantaneous spectra are displayed in figure 2.15 for a Hawking temperature of 1 TeV corresponding to a black hole mass of 10^7 kg and a lifetime of 7.7 minutes. The instantaneous spectra for a Hawking temperature of 10 TeV corresponding to a black hole mass of 10^6 kg and a lifetime of 0.5 seconds are displayed in figure 2.16. There are several important features of these spectra. One feature is that the spectrum of direct neutrinos emitted by the fluid, at the decoupling temperature of $T_\nu = 100$ GeV, peaks at a lower energy than the spectrum of neutrinos that would be emitted directly as Hawking radiation. The peaks are located approximately at $\sqrt{T_\nu T_H}$ for the fluid and at $5T_H$ for the Hawking neutrinos. The reason is that the

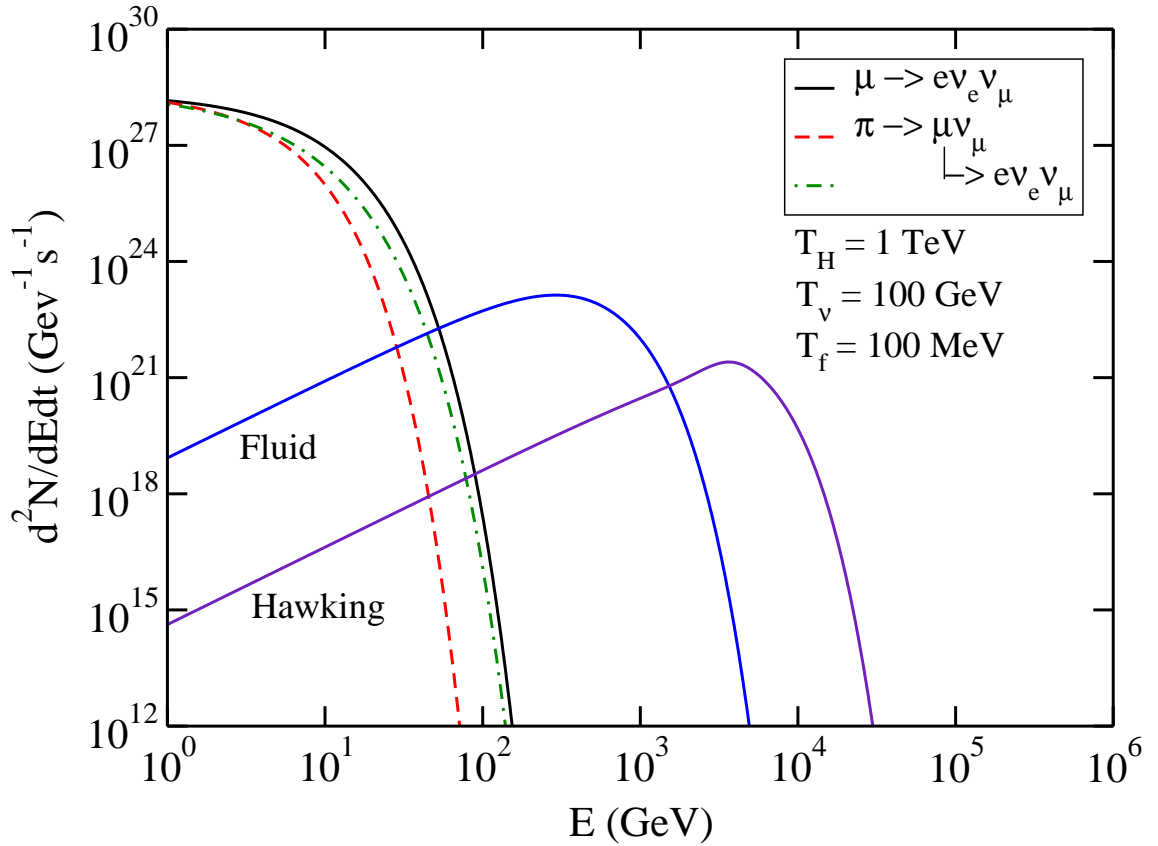


Figure 2.15: The instantaneous direct neutrino spectra emerging from the fluid with neutrino-sphere located at $T_\nu = 100$ GeV compared to the direct Hawking radiation. Also shown are neutrinos arising from pion, direct muon and indirect muon decays at a decoupling temperature of $T_f = 100$ MeV. Here the black hole temperature is $T_H = 1$ TeV. All curves are for one flavor of neutrino or anti-neutrino.

viscous flow degrades the average energy of particles composing the fluid, but the number of particles is greater as a consequence of energy conservation. In the viscous fluid picture of the black hole explosion direct neutrinos are emitted as Hawking radiation without any rescattering when $T_H < T_\nu$, whereas when $T_H > T_\nu$ they are assumed to rescatter and then be emitted from the neutrino-sphere located at T_ν . It is incorrect to add the two curves shown in these figures. In reality, of course, it would be better to use neutrino transport equations to describe what happens when $T_H \approx T_\nu$. That is beyond the scope of this thesis, and perhaps worth doing only if and when there is observational evidence for microscopic black holes.

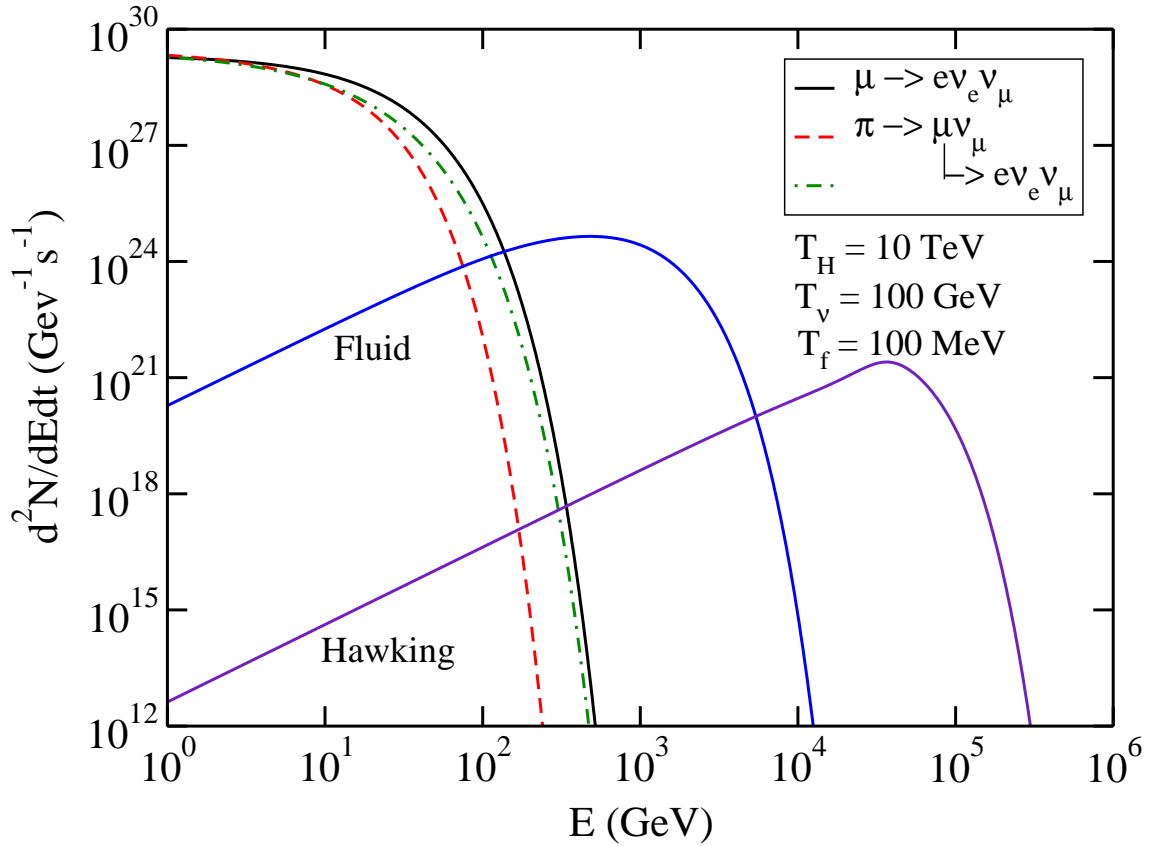


Figure 2.16: Same as figure 2.15 but with $T_H = 1$ TeV.

Here we would like to investigate the discontinuity in the transition from Hawking radiation to neutrino emission from fluid. In order to see the discontinuity, we plot the instantaneous direct neutrino spectra emitted by the fluid and Hawking radiation in figures 2.17, 2.18 and 2.19 for black hole temperatures of 100, 110 and 120 GeV. As one can see, the difference in the slope of both process at high energy reaches a minimum when the black hole temperature is around $T_H = 110$ GeV (figure 2.18). We also calculate the total number of neutrinos per unit time for these three graphs numerically. For $T_H = 100$ GeV

$$\begin{aligned} \frac{dN_\nu^{\text{dir}}}{dt} &\approx 4.13 \times 10^{29}, \\ \frac{dN_\nu^{\text{fluid}}}{dt} &\approx 5.45 \times 10^{29}. \end{aligned} \quad (2.79)$$

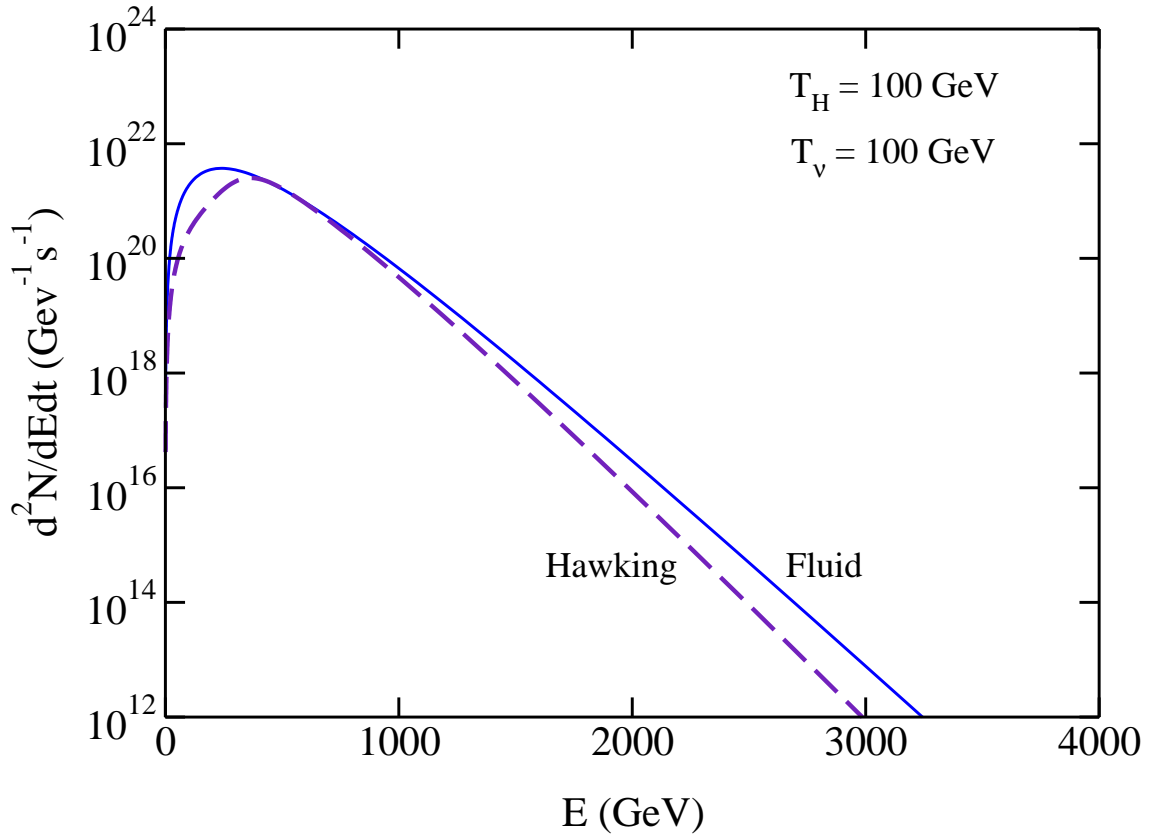


Figure 2.17: The instantaneous direct neutrino spectra emerging from the fluid with neutrino-sphere located at $T_\nu = 100$ GeV compared to the direct Hawking radiation. Both curves are for one flavor of neutrino or anti-neutrino.

For $T_H = 110$ GeV

$$\begin{aligned} \frac{dN_\nu^{\text{dir}}}{dt} &\approx 1.84 \times 10^{29}, \\ \frac{dN_\nu^{\text{fluid}}}{dt} &\approx 2.34 \times 10^{29}. \end{aligned} \quad (2.80)$$

For $T_H = 120$ GeV

$$\begin{aligned} \frac{dN_\nu^{\text{dir}}}{dt} &\approx 2.18 \times 10^{29}, \\ \frac{dN_\nu^{\text{fluid}}}{dt} &\approx 2.69 \times 10^{29}. \end{aligned} \quad (2.81)$$

In this energy range the total number of emitted neutrinos from both process is roughly the same. Therefore if the transition from Hawking radiation to fluid emission

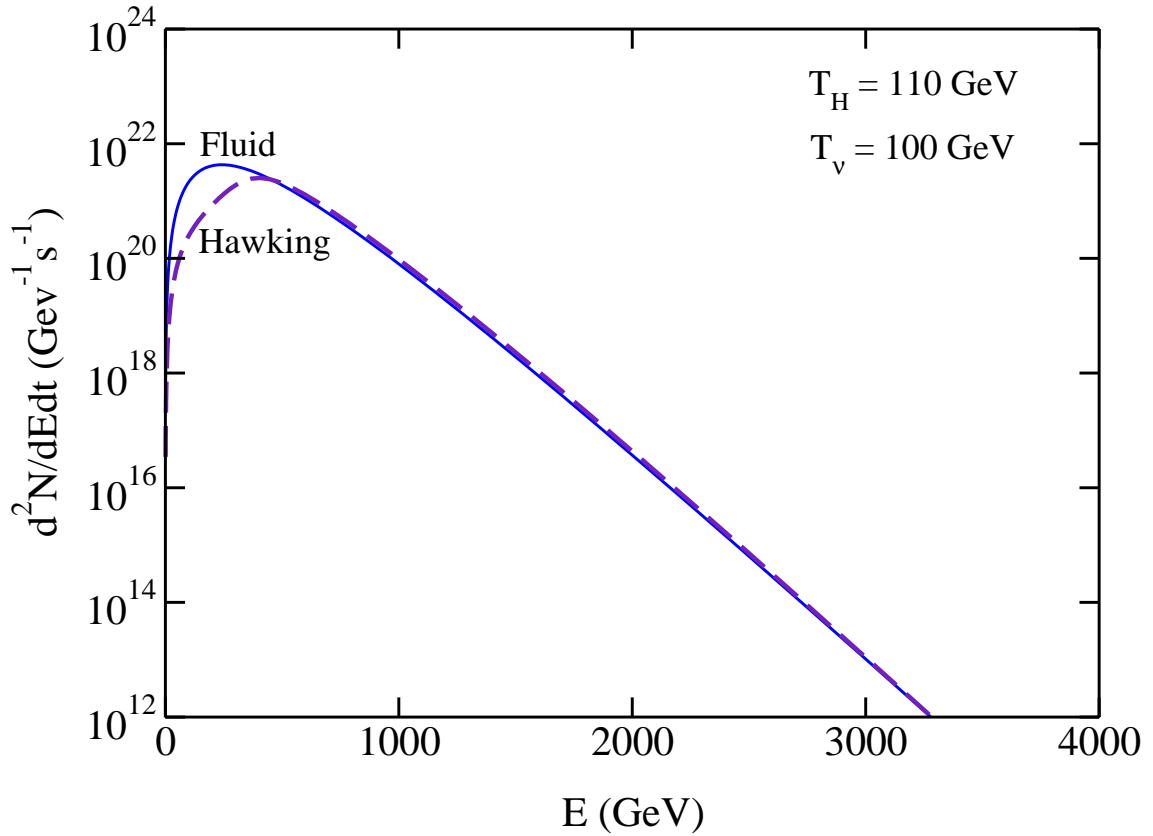


Figure 2.18: Same as figure 2.17 but with $T_H = 110$ GeV.

happens when T_H is around 100 GeV the discontinuity will be small, otherwise the discontinuity is big.

Another feature of figures 2.15 and 2.16 to note is that the average energy of neutrinos arising from pion and muon decay is much less than that of directly emitted neutrinos. Again, the culprit is viscous fluid flow degrading the average energy of particles, here the pion and muon, until the time of their decoupling at $T_f \approx 100$ MeV. On the other hand their number is greatly increased on account of energy conservation. The average energies of the neutrinos are somewhat less than their parent pions and muons because energy must be shared among the decay products. The spectrum of muon-neutrinos coming from the decay $\pi \rightarrow \mu\nu$ is the softest because the pion and muon masses are very close, leaving very little energy for the neutrino.

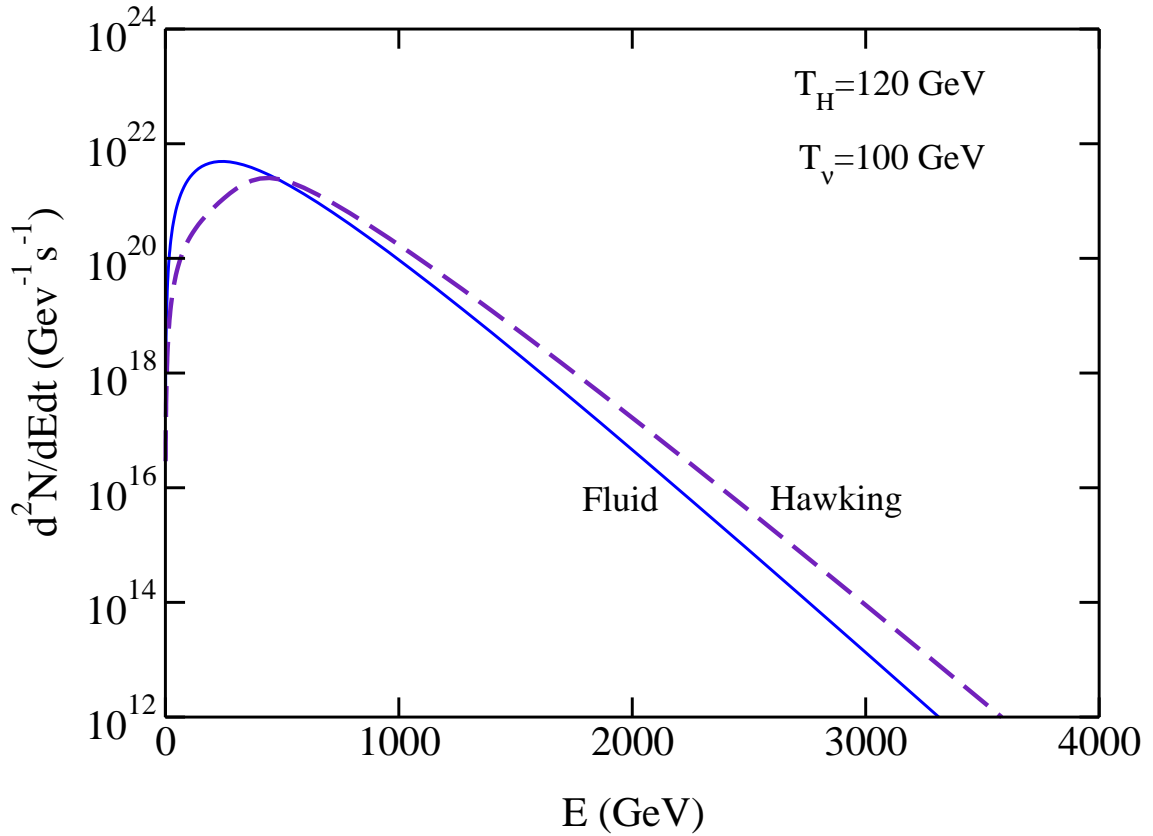


Figure 2.19: Same as figure 2.17 but with $T_H = 120$ GeV.

The time-integrated spectra, starting at the moment when the Hawking temperature is 1 and 10 TeV, are shown in figures 2.20 and 2.21, respectively. The relative magnitudes and average energies reflect the trends seen in figures 2.15 and 2.16. At high energy the Hawking spectrum is proportional to E^{-3} while all the others are proportional to E^{-4} , as was already pointed out in the previous sections. Obviously the greatest number of neutrinos by far are emitted at energies less than 100 GeV. The basic reason is that only about 5% of the total luminosity of the black hole is emitted directly as neutrinos. About 32% goes into neutrinos coming from pion and muon decay, about 24% goes into photons, with most of the remainder going into electrons and positrons.

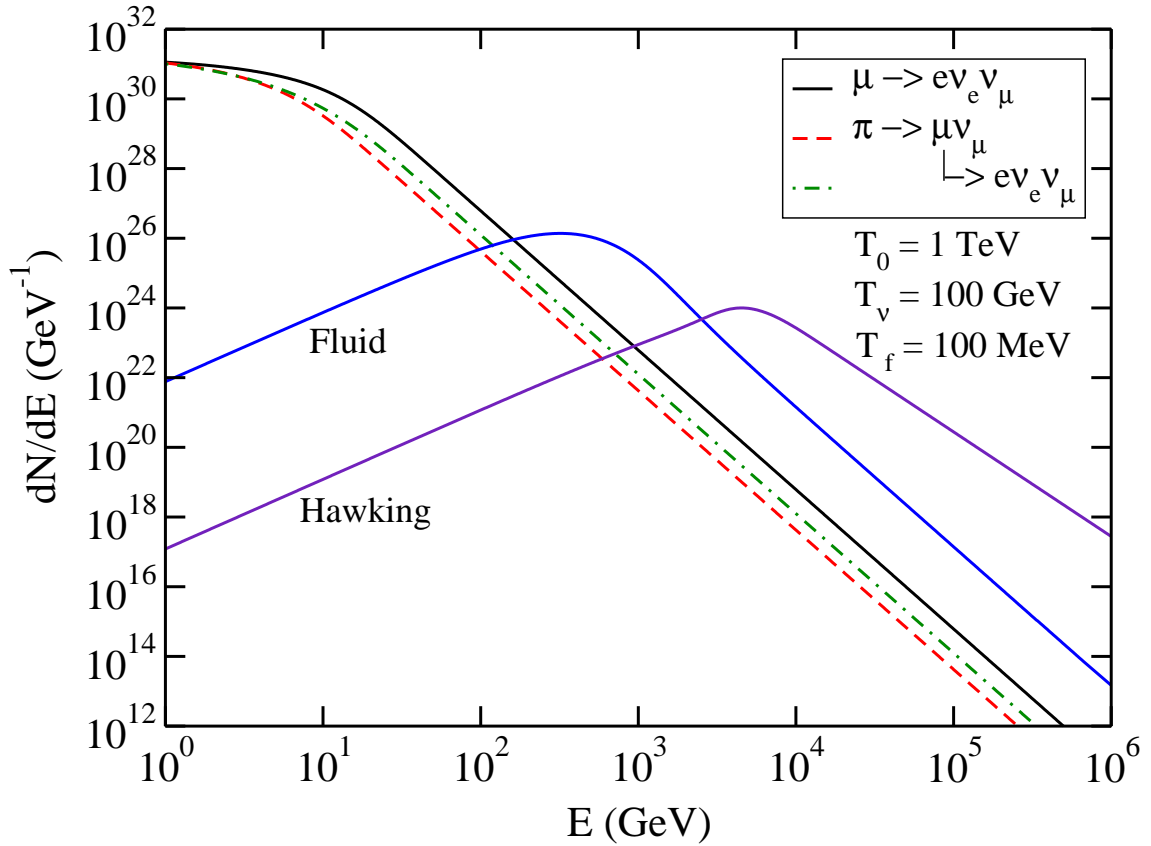


Figure 2.20: The time integrated neutrino spectra emerging from a microscopic black hole. Here the calculation begins when the black hole temperature is $T_0 = 1$ TeV. Either the direct Hawking radiation of neutrinos or the direct neutrino emission from a neutrino-sphere at a temperature of 100 GeV should be used. All curves are for one species of neutrino or anti-neutrino.

2.10 Observability of the Neutrino Flux

We now turn to the possibility of observing neutrinos from a microscopic black hole directly. Obviously this depends on a number of factors, such as the distance to the black hole, the size of the neutrino detector, the efficiency of detecting neutrinos as a function of neutrino type and energy, how long the detector looks at the black hole before it is gone, and so on.

For the sake of discussion, let us assume that one is interested in neutrinos with energy greater than 10 GeV and that the observational time is the last 7.7 minutes of the black hole's existence when its Hawking temperature is 1 TeV and above. As

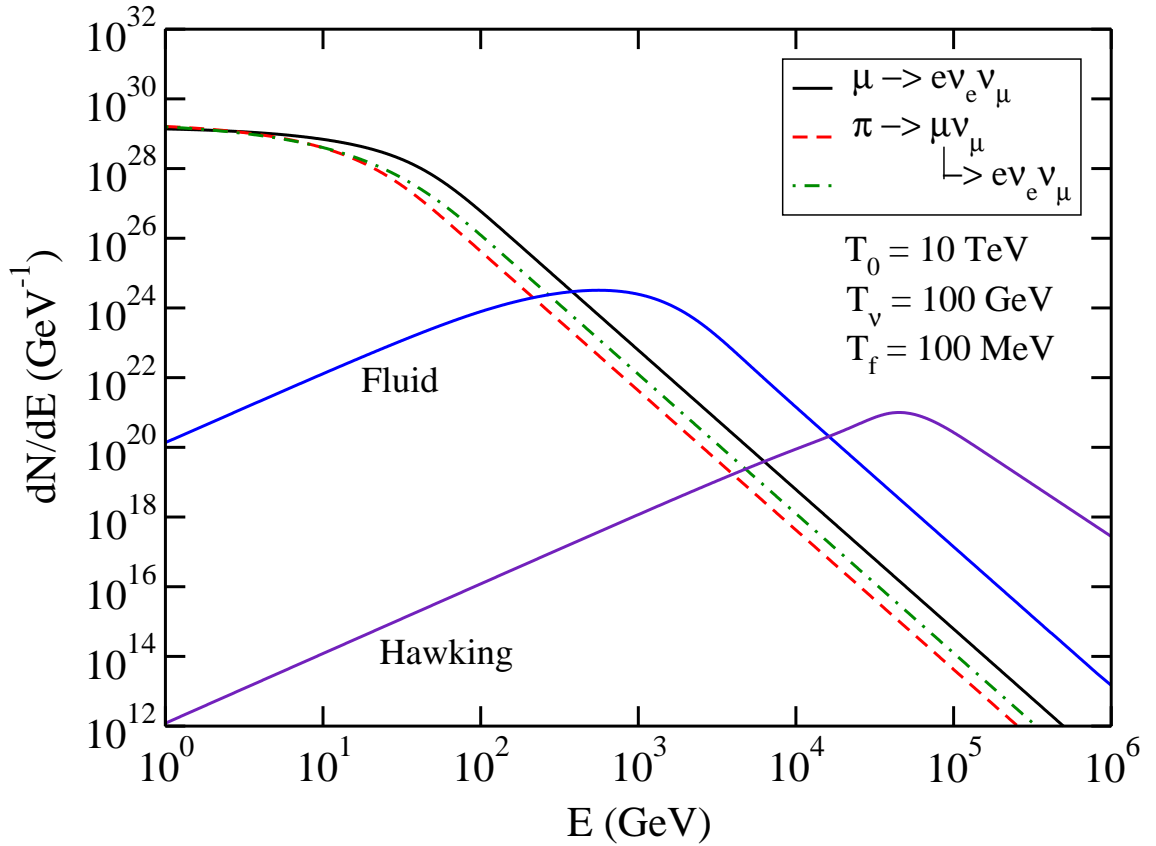


Figure 2.21: Same as figure 2.20 but with $T_0 = 10$ TeV.

may be seen from figure 2.20, most of the neutrinos will come from the decay of directly emitted muons. Integration of Eq. (2.71) from $E_{\min} = 10$ GeV to infinity, and multiplying by 4 to account for both electron and muon type neutrinos and anti-neutrinos, results in the total number of

$$N_\nu = \frac{4}{750} \frac{m_{\text{P}}^2 T_f}{E_{\min}^3} \approx 8 \times 10^{31}. \quad (2.82)$$

This does not take into account neutrinos directly emitted from the fluid. For $E_{\min} = 1$ TeV, for example, Eq. (2.58) should be used in place of Eq. (2.71) (see figure 2.20), and taking into account tau-type neutrinos too then yields a total number of about 3×10^{28} . For an exploding black hole located a distance d from Earth the number of neutrinos per unit area is

$$N_\nu(E > 10 \text{ GeV}) = 6700 \left(\frac{1 \text{ pc}}{d} \right)^2 \text{ km}^{-2}, \quad (2.83)$$

$$N_\nu(E > 1 \text{ TeV}) = 2.5 \left(\frac{1 \text{ pc}}{d} \right)^2 \text{ km}^{-2}. \quad (2.84)$$

Although the latter luminosity is smaller by three orders of magnitude, it has two advantages. First, 1/3 of that luminosity comes from tau-type neutrinos. Unlike electron and muon-type neutrinos, the tau-type is not produced by the decays of pions produced by interactions of high energy cosmic rays with matter or with the microwave background radiation. Hence it would seem to be a much more characteristic signal of exploding black holes than any other cosmic source (assuming no oscillations between the tau-type and the other two species). Second, the tau-type neutrinos come from near the neutrino-sphere, thus probing physics at a temperature of order 100 GeV much more directly than the other types of neutrinos.

What is the local rate density $\dot{\rho}_{\text{local}}$ of exploding black holes? This is, of course, unknown since no one has ever knowingly observed a black hole explosion. The first observational limit was determined by Page and Hawking [45]. They found that the local rate density is less than 1 to 10 per cubic parsec per year on the basis of diffuse gamma rays with energies on the order of 100 MeV. This limit has not been lowered very much during the intervening twenty-five years. For example, Wright [46] used EGRET data to search for an anisotropic high-latitude component of diffuse gamma rays in the energy range from 30 MeV to 100 GeV as a signal for steady emission of microscopic black holes. He concluded that $\dot{\rho}_{\text{local}}$ is less than about 0.4 per cubic parsec per year. If the actual rate density is anything close to these upper limits the frequency of a high energy neutrino detector seeing a black hole explosion ought to be around one per year.

Chapter 3

Cosmic Shells

In this chapter we investigate numerical solutions to the combined field equations of gravity and a scalar field with a potential which has two non-degenerate minima. The absolute minimum of the potential is the true vacuum and the other minimum is the false vacuum. This potential is shown in figure 3.1. The true vacuum of the potential is at f_2 and the false vacuum is at f_1 . The two minima are separated by a barrier.

3.1 Shell Solutions in Static Coordinates

Consider a scalar field coupled to gravity with the Lagrangian

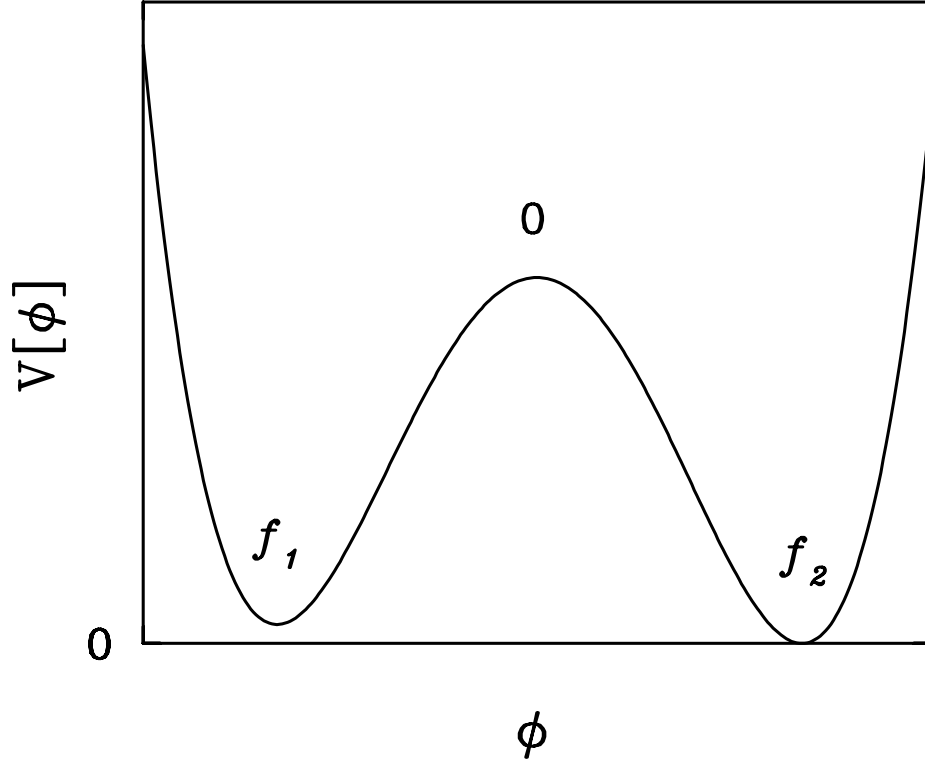
$$\mathcal{L} = \frac{1}{16\pi G} R + \frac{1}{2}\phi_{;\mu}\phi^{;\mu} - V[\phi] \quad (3.1)$$

where the potential $V[\phi]$ has two minima at f_1 and f_2 separated by a barrier. See figure 3.1.

We look for spherically symmetric configurations in which the metric of space-time is written as

$$ds^2 = -\frac{H}{p^2}dt^2 + \frac{dr^2}{H} + r^2(d\theta^2 + \sin^2\theta d\varphi^2) . \quad (3.2)$$

The functions ϕ , H , and p depend only on r and t . A tetrad basis is chosen, in a

Figure 3.1: The potential $V[\phi]$.

region $H > 0$, as

$$e_0 = \frac{\sqrt{H}}{p} dt, \quad e_1 = \frac{1}{\sqrt{H}} dr, \quad e_2 = r d\theta, \quad e_3 = r \sin \theta d\varphi. \quad (3.3)$$

The components of the energy-momentum tensor in the tetrad basis, $T_{ab} = e_a^\mu e_b^\nu T_{\mu\nu}$, are

$$\begin{aligned} T_{00} &= \frac{1}{2} \left(\frac{p^2}{H} \dot{\phi}^2 + H \phi'^2 \right) + V[\phi] \\ T_{11} &= \frac{1}{2} \left(\frac{p^2}{H} \dot{\phi}^2 + H \phi'^2 \right) - V[\phi] \\ T_{22} = T_{33} &= \frac{1}{2} \left(\frac{p^2}{H} \dot{\phi}^2 - H \phi'^2 \right) - V[\phi] \\ T_{01} &= -p \dot{\phi} \phi'. \end{aligned} \quad (3.4)$$

Here dots and primes indicate t and r derivatives, respectively.

The scalar field satisfies

$$p \frac{\partial}{\partial t} \left(\frac{p}{H} \dot{\phi} \right) - \frac{p}{r^2} \frac{\partial}{\partial r} \left(\frac{r^2 H}{p} \phi' \right) + V'[\phi] = 0. \quad (3.5)$$

We introduce the integrated mass function $M(t, r)$ by

$$H = 1 - \frac{2GM}{r} . \quad (3.6)$$

The Einstein equations are

$$M = \int_0^r 4\pi r^2 dr T_{00} , \quad (3.7)$$

$$\frac{p'}{p} = -4\pi Gr \left\{ \frac{p^2}{H^2} \dot{\phi}^2 + \phi'^2 \right\} , \quad (3.8)$$

$$\frac{\dot{H}}{H} = -8\pi Gr \dot{\phi} \phi' , \quad (3.9)$$

$$\frac{p}{2} \left\{ \frac{\partial}{\partial t} \left(\frac{p\dot{H}}{H^2} \right) + \frac{\partial}{\partial r} \left(\frac{H'}{p} - \frac{2Hp'}{p^2} \right) \right\} + \frac{1-H}{r^2} = 4\pi G \left(\frac{p^2}{H} \dot{\phi}^2 - H\phi'^2 \right) . \quad (3.10)$$

One of the equations, Eq. (3.10), is redundant as it follows from Eqs. (3.5), (3.7), (3.8), and (3.9).

We shall seek static solutions for which the set of equations reduces to

$$\phi''(r) + \Gamma_{\text{eff}}(r)\phi'(r) = \frac{1}{H} V'[\phi] , \quad (3.11)$$

$$M(r) = \int_0^r 4\pi r^2 dr \left\{ \frac{1}{2} H\phi'^2 + V[\phi] \right\} , \quad (3.12)$$

where

$$\begin{aligned} \Gamma_{\text{eff}} &\equiv \frac{2}{r} - \frac{p'}{p} + \frac{H'}{H} , \\ \frac{p'}{p} &= -4\pi Gr\phi'^2 . \end{aligned} \quad (3.13)$$

Equation (3.11) can be interpreted as an equation for a particle with a coordinate ϕ and time r . Except for a factor $1/H$ this particle moves in a potential $U[\phi] = -V[\phi]$. The coefficient $\Gamma_{\text{eff}}(r)$ represents time (r) dependent friction.

The potential $V[\phi]$ is supposed to have two minima at f_1 and f_2 . We are looking for a solution which starts at $\phi \sim f_1$, moves close to f_2 , and comes back to f_1 at $r = \infty$. The particle's potential $U[\phi]$ has two maxima. The particle begins near the top of one hill, rolls down into the valley and up the other hill, turns around and rolls down and then back up to the top of the original hill. This is impossible in flat space,

as Γ_{eff} is positive-definite so that the particle's energy dissipates and it cannot climb back to its starting point.

In the presence of gravity the situation changes. The non-vanishing energy density can make H a decreasing function of r so that Γ_{eff} becomes negative. The energy lost by the particle during the initial rolling down can be regained on the return path by negative friction, or thrust. Indeed, this happens.

Let us set up the problem more precisely. We take a quartic potential with $f_1 < 0 < f_2$;

$$\begin{aligned} V'[\phi] &= \lambda\phi(\phi - f_1)(\phi - f_2) , \\ V[\phi] &= \frac{\lambda}{4}(\phi - f_2)\left\{\phi^3 - \frac{1}{3}(f_2 + 4f_1)\phi^2 - \frac{1}{3}f_2(f_2 - 2f_1)(\phi + f_2)\right\} . \end{aligned} \quad (3.14)$$

Here $V[f_2] = 0$, and $V[0]$ is a local maximum for the barrier separating the two minima. Define $f = (|f_1| + f_2)/2$ and $\Delta f = f_2 - |f_1|$. In case $\Delta f > 0$, $\phi = f_1$ corresponds to a false vacuum with the energy density $\epsilon = V[f_1] = \frac{2}{3}\lambda f^3 \Delta f > 0$, whereas $\phi = f_2$ corresponds to a true vacuum with a vanishing energy density. As we shall discuss in detail below, the positivity of the energy density ϵ plays an important role for the presence of shell structure, but the vanishing $V[f_2]$ is not essential as we see below. In a more general potential it could be that $V[f_2] > V[f_1]$.

We look for solutions with ϕ starting at the origin $r = 0$ very close to f_1 . There is only one parameter to adjust: $\phi_0 \equiv \phi(0)$. The behavior of a solution near the origin is given by

$$\begin{aligned} \phi &= \phi_0 + \phi_2 r^2 + \dots , & \phi_2 &= \frac{1}{6} V'[\phi_0] , \\ p &= 1 + p_4 r^4 + \dots , & p_4 &= -4\pi G \phi_2^2 , \\ M &= m_3 r^3 + \dots , & m_3 &= \frac{4\pi}{3} V[\phi_0] , \\ H &= 1 - 2Gm_3 r^2 + \dots . \end{aligned} \quad (3.15)$$

Given ϕ_0 the equations determine the behavior of a configuration uniquely. For most values of ϕ_0 the corresponding configurations are unacceptable. As r increases, $\phi(r)$ either approaches 0 (the local maximum of $V[\phi]$) after oscillation, or comes back to

cross f_1 and continues to decrease. Other than the two trivial solutions, corresponding to the false and true vacua, we have found a new type of solution.

There are four parameters in the model, one of which, the gravitational constant $G = m_{\text{P}}^{-2}$, sets the scale. The other three are λ , f_1 , and f_2 or, equivalently, the three dimensionless quantities f/m_{P} , $\Delta f/f$, and λ . We have explored only a limited region of the parameter space. The moduli space of solutions depends critically on f/m_{P} and $\Delta f/f$. The λ dependence can be absorbed by rescaling. The solution $\phi(r; \lambda)$ to Eqs. (3.6), (3.11)-(3.13) for a given λ is related to the solution for $\lambda = 1$ by $\phi(r; \lambda) = \phi(\sqrt{\lambda}r; 1)$. We shall see that nontrivial solutions appear as f/m_{P} becomes small.

If $\phi_0 < f_1$, $\phi(r)$ monotonically decreases as the radius increases. On the way $H(r)$ goes to zero at a finite radius r_m . $\phi'(r)$ may or may not diverge there. To describe most general solutions the metric is written as [52]

$$ds^2 = -Q(\rho)dt^2 + \frac{d\rho^2}{Q(\rho)} + R(\rho)^2(d\theta^2 + \sin^2 d\varphi^2) \quad , \quad (3.16)$$

which is related to Eq. (3.2) by

$$R = r \quad , \quad Q = \frac{H}{p^2} \quad , \quad \frac{d\rho}{dr} = \pm \frac{1}{|p|} \quad . \quad (3.17)$$

If $Q(\rho)$ tends to zero linearly in ρ , the space-time has a nondegenerate Killing horizon, while if $Q(\rho)$ tends smoothly to a nonzero value, there is a bag of gold solution studied by Volkov *et al.* [52] in the context of Einstein-Yang-Mills equations.

As

$$|p(r)| = \exp \left\{ -4\pi G \int_0^r dr \, r \phi'^2 \right\} \quad , \quad (3.18)$$

p can vanish at r_m and $Q(\rho)$ can approach a nonzero value there if ϕ' diverges fast enough. In this case $dR/d\rho = 0$. In other words, as ρ increases, $R(\rho)$ reaches a maximum R_{max} at $\rho(r_m)$ and starts to decrease. Eventually $R(\rho)$ becomes zero at ρ_{max} . This would lead to a bag-of-gold solution. It is not clear whether such solutions exist in the scalar model under discussion [53].

Suppose instead that $f_1 < \phi_0 < 0$ and ϕ_0 is not too close to f_1 . In the particle analogue, the particle starts to roll down the hill under the action of $U[\phi] = -V[\phi]$.

It approaches $\phi = 0$, and oscillates around it. In the meantime $H(r)$ crosses zero. We are not interested in this type of solution either.

Now suppose that ϕ_0 is very close to, but still greater than, f_1 : $\phi(0) = f_1 + \delta\phi(0)$ with $0 < \delta\phi(0)/f \ll 1$. A schematic of the resulting solution is displayed in figures 3.2 and 3.3. We divide space into three regions in the static coordinates: region I ($0 \leq r < R_1$), region II ($R_1 < r < R_2$), and region III ($R_2 < r$). It turns out that $\phi(r)$ varies little from f_1 in regions I and III so that the equation of motion for ϕ may be linearized in those regions. In region II the field deviates strongly and the full set of nonlinear equations must be solved numerically. This is the region in which we shall find shell structure. $H(r)$ deviates from the de Sitter value significantly. In region III the space-time is approximately de Sitter again. $H(r)$ crosses zero at r_H where $p(r)$ remains positive. Consequently $Q(\rho)$ in Eq. (3.16) also crosses zero linearly so that the space-time has a horizon.

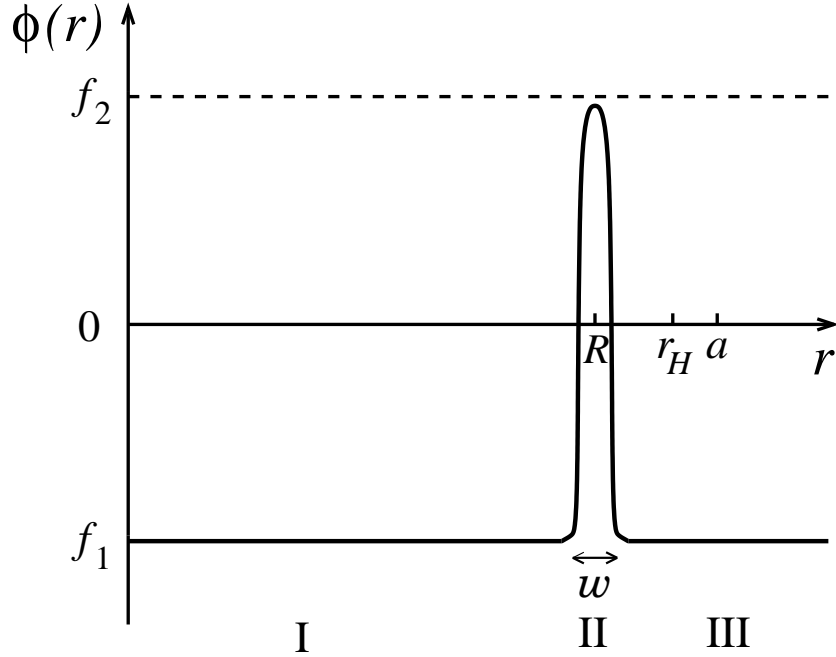


Figure 3.2: Schematic behavior of $\phi(r)$.

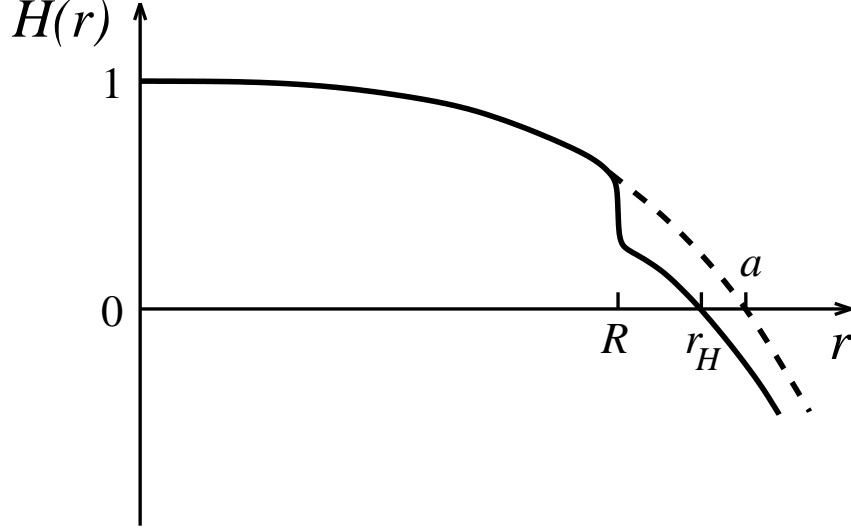


Figure 3.3: Schematic behavior of $H(r)$.

In region I the space-time is approximately de Sitter:

$$T_{00} = \epsilon, \quad H = 1 - \frac{r^2}{a^2}, \quad a = \sqrt{\frac{3}{8\pi G\epsilon}}, \quad p = 1. \quad (3.19)$$

The equation for $\phi(r)$ can be linearized with $\phi(r) = f_1 + \delta\phi(r)$. In terms of $z \equiv r^2/a^2$,

$$\left\{ z(1-z) \frac{d^2}{dz^2} + \left(\frac{3}{2} - \frac{5}{2}z \right) \frac{d}{dz} - \frac{1}{4}\omega^2 a^2 \right\} \delta\phi = 0, \quad (3.20)$$

where $\omega^2 = V''[f_1]$. This is Gauss' hypergeometric equation. The solution which is regular at $r = 0$ is

$$\delta\phi(r) = \delta\phi(0) \cdot F\left(\frac{3}{4} + i\kappa, \frac{3}{4} - i\kappa, \frac{3}{2}; z\right), \quad (3.21)$$

where

$$\kappa = \frac{1}{2}\sqrt{\omega^2 a^2 - \frac{9}{4}}, \quad \omega^2 a^2 = \frac{9m_{\text{P}}^2}{8\pi f \Delta f} \left(1 - \frac{\Delta f}{2f}\right). \quad (3.22)$$

We shall soon see that a solution with shell structure appears for $\omega a \gg 1$ with a particular choice of $\delta\phi(0)$. The ratio of $\delta\phi'(r)$ to $\delta\phi(r)$ is given by

$$\frac{\delta\phi'(r)}{\delta\phi(r)} = \frac{4r}{3a^2} \left(\kappa^2 + \frac{9}{16} \right) \frac{F\left(\frac{7}{4} + i\kappa, \frac{7}{4} - i\kappa, \frac{5}{2}; z\right)}{F\left(\frac{3}{4} + i\kappa, \frac{3}{4} - i\kappa, \frac{3}{2}; z\right)} \equiv \frac{2r}{a^2} J(z). \quad (3.23)$$

The deviation from f_1 at the origin, $\delta\phi(0)$, needs to be very small for an acceptable solution. The behavior of the hypergeometric function for $\kappa \gg 1$ and $0 < z < 1$ is given by [54]

$$F(a + i\kappa, a - i\kappa, c; z) \sim \frac{\Gamma(c)}{2\sqrt{\pi}} \kappa^{\frac{1}{2}-c} z^{-\frac{c}{2}+\frac{1}{4}} (1-z)^{\frac{c}{2}-\frac{1}{4}-a} \exp\left\{2\kappa \sin^{-1} \sqrt{z}\right\}. \quad (3.24)$$

The ratio $\delta\phi(r)/\delta\phi(0)$ grows exponentially as r increases like $(4\kappa)^{-1} z^{-1/2} (1-z)^{-1/4} \exp\left\{2\kappa \sin^{-1} \sqrt{z}\right\}$. At the end of region I, $\delta\phi/|f_1|$ needs to be very small for the linearization to be valid. The ratio of $F'(z)$ to $F(z)$, $J(z)$ in Eq. (3.23), is given by

$$J(z) = \frac{\kappa}{\sqrt{z(1-z)}} \quad \text{for } \kappa \gg 1, \quad 0 < z < 1. \quad (3.25)$$

In region II, $\phi(r)$ varies substantially and the nonlinearity of the equations plays an essential role. In this region the equations must be solved numerically. With fine tuning of the value of $\delta\phi(R_1)$ nontrivial shell solutions will be found.

The algorithm is the following. First $\delta\phi(R_1)$ is chosen and $\delta\phi'(R_1)$ is evaluated by Eqs. (3.23) and (3.25). To the order in which we work the metric is $H(R_1) = 1 - (R_1/a)^2$ and $p(R_1) = 1$. With these boundary conditions Eqs. (3.11) and (3.12) are numerically solved.

The behavior of solutions in region II is displayed in figure 3.4. When the specific values of the input parameters are chosen to be $\lambda = 0.01$, $f/m_P = 0.002$, and $\Delta f/f = 0.002$, then the output parameters are $a/l_P = 2.365 \times 10^7$, $\kappa = 3.344 \times 10^3$, $R_1/l_P = 1.76104695 \times 10^7$ and $\delta\phi(R_1)/m_P = 10^{-5}$. (Here l_P is the Planck length.) The field $\phi(r)$ approaches f_1 for $r > R_2$. In the numerical integration $\delta\phi(R_1)$ is kept fixed while R_1 is varied. Fine tuning to the ninth digit is necessary. If R_1 is taken to be slightly bigger then $\phi(r)$ starts to deviate from f_1 in the negative direction as r increases. If R_1 is taken to be slightly smaller then $\phi(r)$ starts to deviate from f_1 in

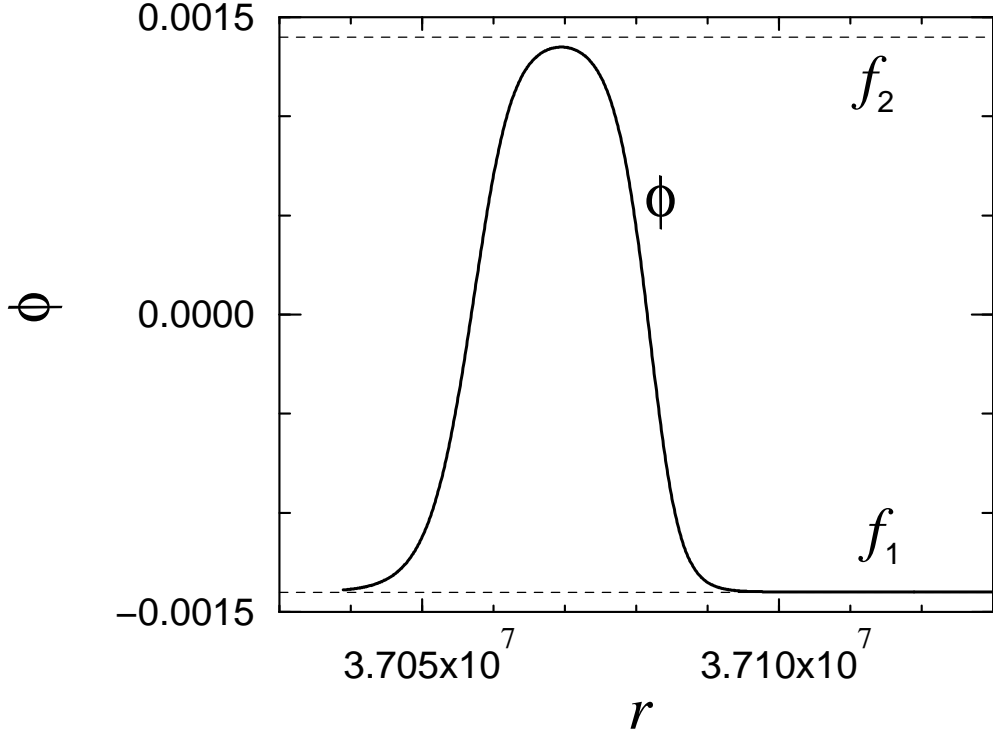


Figure 3.4: $\phi(r)$ of a solution with $f/m_{\text{P}} = 1.40 \times 10^{-3}$, $\Delta f/f = 0.002$, $\lambda = 0.01$. ϕ and r are in the units of m_{P} and l_{P} , respectively. The maximum value of ϕ is smaller than $f_2 \sim 0.0014 \cdot m_{\text{P}}$.

the positive direction, heading for f_2 as r increases. With just the right value the space-time becomes nearly de Sitter outside the shell. The value of $\delta\phi$ at the origin ($r = 0$) is found from Eq. (3.21) to be 1.40×10^{-2440} , which explains why one cannot numerically integrate $\phi(r)$ starting from $r = 0$.

The behavior of the solution in region III is easily inferred. From the numerical integration in region II both $H_2 = H(R_2)$ and $p_2 = p(R_2)$ are determined. In region III the metric can be written in the form

$$\begin{aligned} H(r) &= 1 - \frac{2G\tilde{M}}{r} - \frac{r^2}{a^2} \\ p(r) &= p_2 . \end{aligned} \tag{3.26}$$

Here \tilde{M} is the mass ascribable to the shell. Once T_{00} vanishes $H(r)$ must take this form. The value of \tilde{M} may be determined numerically by fitting Eq. (3.26) just outside the shell. The location of the horizon, r_H , is determined by $H(r_H) = 0$. The

field $\phi(r)$ remains very close to f_1 in region III.

At this point due caution is required to continue the solution because the static coordinates defined in Eq. (3.2) do not cover the whole of space-time. The global structure of the space-time and of the solutions is worked out in Sec. 3.4 where different coordinates are employed.

The solutions we found have shell structure at a radius R whose width w is very small. The radius R is smaller than the horizon radius r_H , but is of the same order as a . In the next section we shall see that R becomes smaller as f becomes smaller, but remains of order a even in the $f \rightarrow 0$ limit. This implies that the shell structure is cosmic in size.

An estimate of the order of magnitude of w as well as the conditions necessary for the existence of the cosmic shell are obtained by a simple argument. Return to Eq. (3.11),

$$H\phi'' + \left(\frac{2H}{r} + H'\right)\phi' + 4\pi GrH\phi^3 = V'[\phi]. \quad (3.27)$$

In the shell region (region II, $r \sim R$) of typical solutions, H is of order one and drops sharply. In Eq. (3.27) the $2H/r$ term is negligible compared with the H' term. The remaining terms, $H\phi''$, $H'\phi'$, and $V'[\phi]$ are all of the same order of magnitude so that $f/w^2 \sim \lambda f^3$ or

$$w \sim \frac{1}{\sqrt{\lambda f}}. \quad (3.28)$$

Hence the thickness of the shell is determined by the parameters in the scalar field potential. The radius R is smaller than but of the same order as a . The solutions exist only if H' , which is negative, dominates over $4\pi GrH\phi^2$. In other words $w^{-1} > 4\pi GR(f/w)^2$. Making use of $R \sim a$, $a^2 = 9/(16\pi G\lambda f^3 \Delta f)$ and Eq. (3.28), one finds

$$4\pi \left(\frac{f}{m_{\text{P}}}\right)^2 < \frac{w}{a} \sim \frac{4\sqrt{\pi}}{3} \frac{\sqrt{f\Delta f}}{m_{\text{P}}} \ll 1$$

$$\frac{\Delta f}{f} > 3\sqrt{\pi} \left(\frac{f}{m_{\text{P}}}\right)^2. \quad (3.29)$$

We shall see in the next section that these relations are satisfied in the solutions obtained numerically.

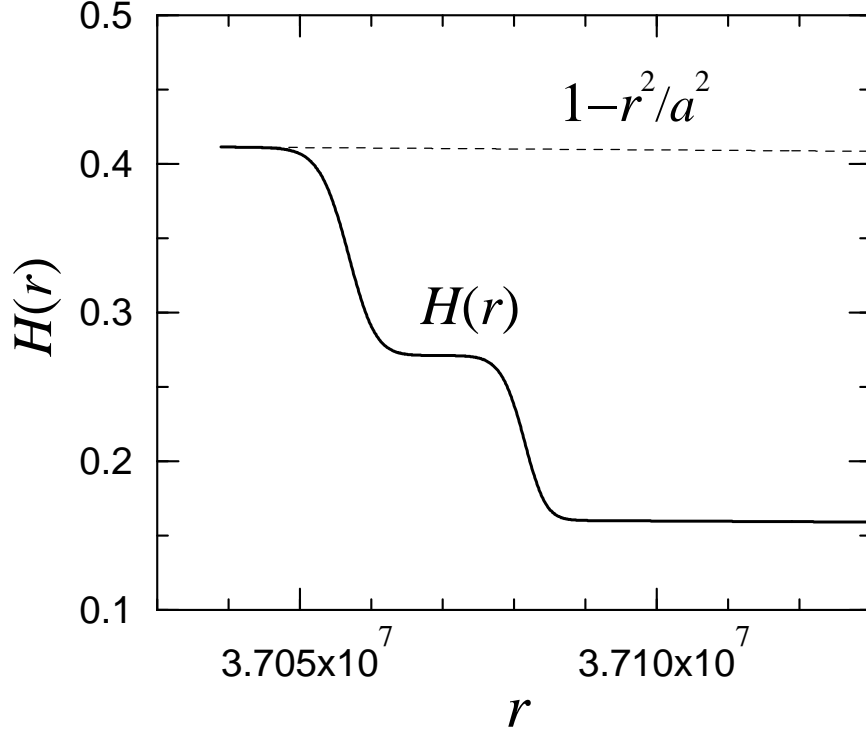


Figure 3.5: $H(r)$ of a solution with $f/m_{\text{P}} = 1.40 \times 10^{-3}$, $\Delta f/f = 0.002$, $\lambda = 0.01$. $H(r)$ decreases in two steps in the shell region. $H(r)$ in the de Sitter space ($= 1 - r^2/a^2$) is plotted in a dotted line.

3.2 Numerical Analysis of the Nonlinear Regime

In the preceding section we solved the linearized field equation for $\phi(r)$ in regions I and III where the deviation from f_1 is small, and we sketched the behavior in the nonlinear region II where the shell structure appears. In this section we present numerical results for region II. As discussed in the preceding section the boundary between regions I and II, located at the matching radius R_1 , is rather arbitrary, subject only to the condition that the linearization is accurate up to that radius. Precise tuning is necessary for the pair R_1 and $\delta\phi(R_1)$ to obtain a solution to all the equations. Technically it is easier to keep $\delta\phi(R_1)$ fixed and adjust the matching radius R_1 . If R_1 is chosen too small ϕ comes back toward, but cannot reach, f_1 . What happens is that ϕ eventually oscillates around $\phi = 0$ as r increases. If R_1 is chosen too large ϕ comes back to f_1 at finite r to roll over it and continues to decrease.

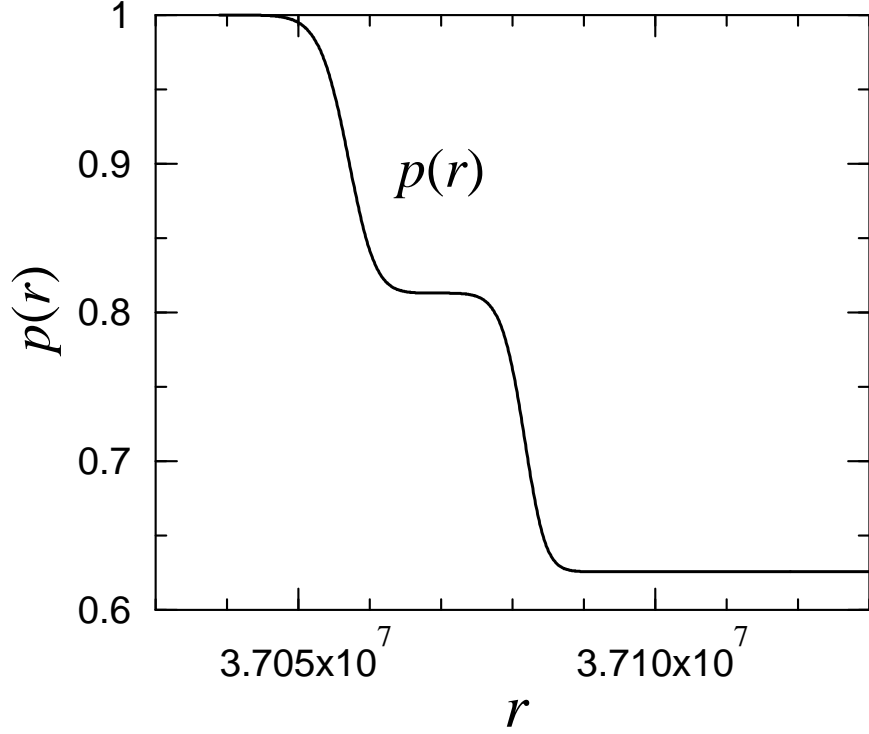


Figure 3.6: $p(r)$ of a solution with $f/m_{\text{P}} = 1.40 \times 10^{-3}$, $\Delta f/f = 0.002$, $\lambda = 0.01$. $p(r)$ decreases in two steps, from 1 to 0.6256, in the shell region.

For each sufficiently small value of $\delta\phi$ chosen as the matching value there exists a desired solution with $R_1 = R_c$. The critical value R_c can be determined numerically to arbitrary accuracy.

One example of such a solution is displayed in figure 3.4 for the parameters $f/m_{\text{P}} = 1.40 \times 10^{-3}$, $\Delta f/f = 0.002$, $\lambda = 0.01$ and $\delta\phi(R_1) = 1.0 \times 10^{-5}$. The matching radius R_1 is fine-tuned to ten digits: $R_1/l_{\text{P}} \sim 3.7038855228 \times 10^7$. The shell is very thin compared to the radius of the shell, lying in the region $3.704 \times 10^7 \leq r/l_{\text{P}} \leq 3.710 \times 10^7$.

In the shell region both $H(r)$ and $p(r)$ decrease in a two-step fashion. See figures 3.5 and 3.6. Inside and outside the shell $H(r)$ is given by Eqs. (3.19) and (3.26), whereas $p(r)$ assumes the constant values 1 and 0.6256, respectively.

The change is induced by the non-vanishing energy-momentum tensor components $T_{00} = -T_{22} = -T_{33}$ and T_{11} . They are displayed in figures 3.7 and 3.8. The energy

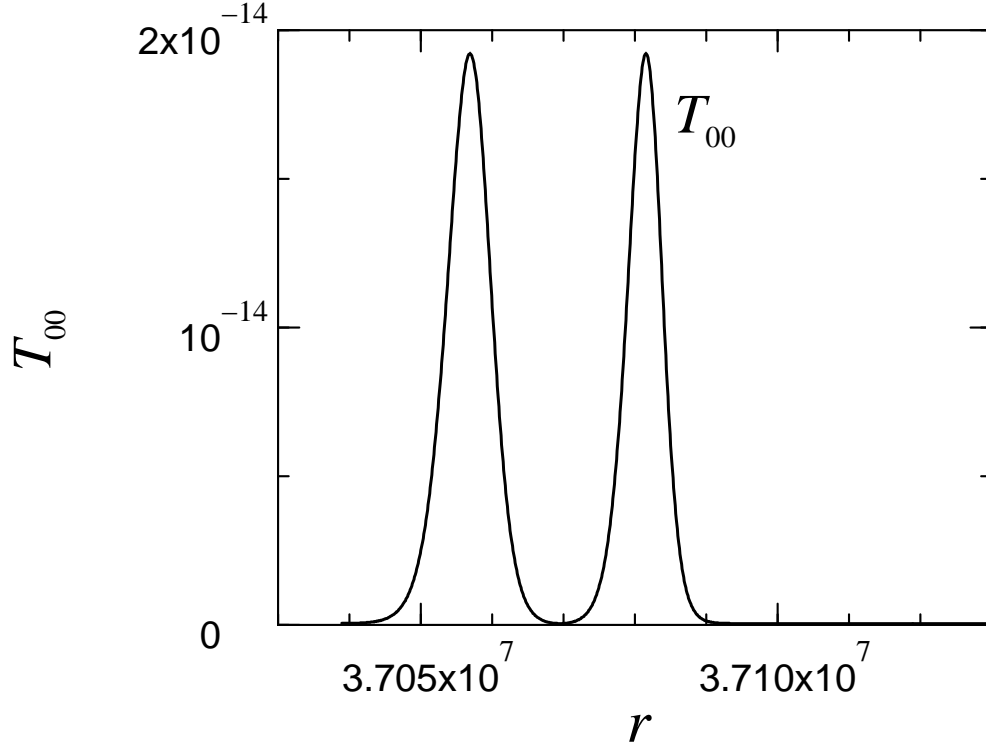


Figure 3.7: The energy density T_{00} for a shell solution with $f/m_{\text{P}} = 1.40 \times 10^{-3}$, $\Delta f/f = 0.002$, $\lambda = 0.01$. T_{00} and r are in the units of m_{P}^4 and l_{P} , respectively. The energy density is localized in the two shells over the de Sitter background.

density T_{00} has two sharp peaks associated with the rapid variation of ϕ . The radial pressure T_{11} , on the other hand, steps up quickly, remains constant within the shell, and then steps down again. The value of T_{11} is very small ($\sim 5 \times 10^{-17} m_{\text{P}}^4$) compared with the maximum value of T_{00} ($\sim 2 \times 10^{-14} m_{\text{P}}^4$). The contributions of the kinetic energy, $\frac{1}{2}H\dot{\phi}^2$, and potential energy, $V[\phi]$, almost cancel each other.

In this example $\phi(r)$ makes a bounce transition $f_1 \rightarrow f_2 \rightarrow f_1$ once. As the numerical value of f becomes smaller than $0.002m_{\text{P}}$ a new type of solution with double bounces $f_1 \rightarrow f_2 \rightarrow f_1 \rightarrow f_2 \rightarrow f_1$ emerge. One example is displayed in figure 3.9.

The spectrum of the shell solutions depends on the parameter f . In figure 3.10 R/a , r_H/a , and R/r_H are plotted as functions of f . (Finding the solution numerically becomes extremely difficult as f becomes smaller.) There are several features to be

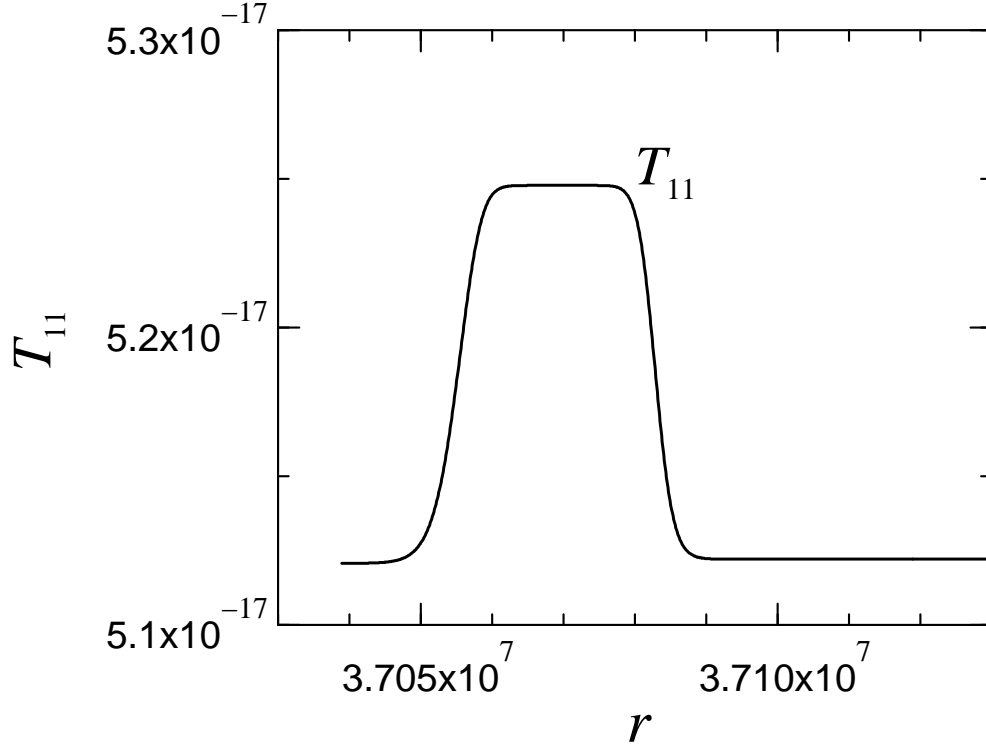


Figure 3.8: The radial pressure T_{11} for a shell solution with $f/m_{\text{P}} = 1.40 \times 10^{-3}$, $\Delta f/f = 0.002$, $\lambda = 0.01$. T_{11} and r are in the units of m_{P}^4 and l_{P} , respectively. The pressure is higher and constant between the two shells.

noted. First, with fixed values of λ and $\Delta f/f$ solutions exist only for $f < f_{\text{max}}$. For example, with $\lambda = 0.01$ and $\Delta f/f = 0.002$ we find that $f_{\text{max}} \sim 0.006$. Second, as f goes to 0, $r_{\text{H}}/a \rightarrow 1$ and $R/a \rightarrow 0.8$. The relative size R/a of the shell remains of order one even in the $f \rightarrow 0$ limit. Third, as f decreases shell solutions with multiple bounces become possible. We cannot determine how many times ϕ can bounce inside the horizon because the numerical evaluation becomes extremely difficult when $f/m_{\text{P}} < 0.001$.

In the potential we are analyzing, $\phi = f_1$ and $\phi = f_2$ correspond to the false and true vacua, respectively. For the existence of shell solutions the fact $V[f_1] > V[f_2]$ is not crucial, however. In the example displayed in figure 3.4, for instance, $\phi(r)$ swings from $\phi(0) \sim f_1$ to $\phi_{\text{max}} < f_2$, and returns to f_1 . Numerically $V[\phi_{\text{max}}] > V[\phi(0)]$. As we are solving classical differential equations, only the form of the potential $V[\phi]$

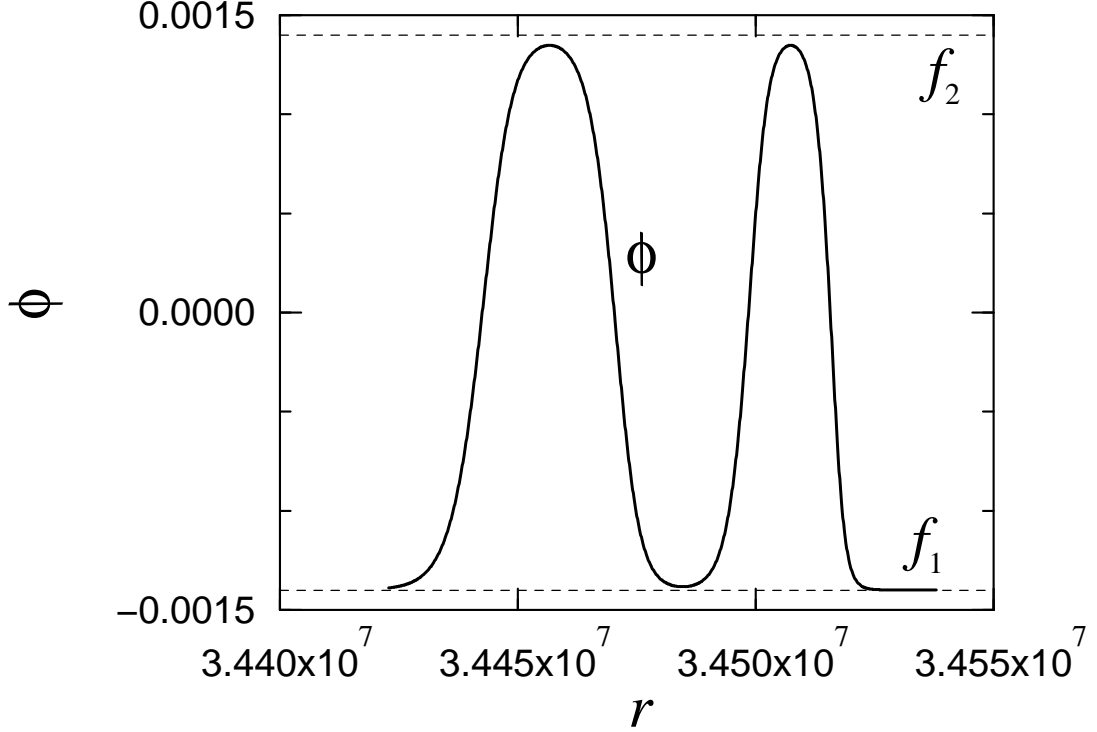


Figure 3.9: A solution with double bounces with $f/m_{\text{P}} = 1.40 \times 10^{-3}$, $\Delta f/f = 0.002$, $\lambda = 0.01$. A solution with multiple bounces appears at a smaller shell radius than a solution with a single bounce.

between f_1 and ϕ_{max} is relevant. The form of the potential for $\phi > \phi_{\text{max}}$ does not matter. The second minimum can be higher than the first one; $V[f_1] < V[f_2] < V[\phi_{\text{max}}]$. Before concluding this section we would like to add that we have found no solution in which ϕ makes a transition from f_1 to f_2 as r varies from 0 to ∞ .

3.3 Global Structure of the Space-Time and Solutions

In the preceding section we found novel solutions to a theory with a scalar field coupled to gravity in static coordinates. The static coordinates in Eq. (3.2), however, do not cover all of space-time. In this section we construct coordinates which allow for an extension of the solution to the full space-time manifold. These coordinates are

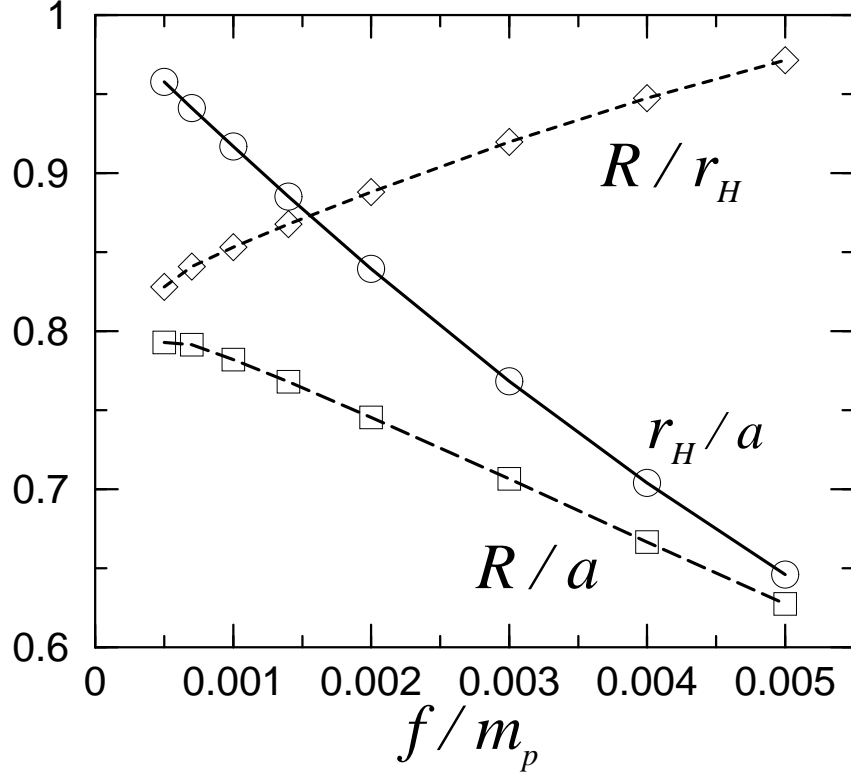


Figure 3.10: The f -dependence of the shell solutions. $\lambda = 0.01$ and $\Delta f/f = 0.002$ are fixed. R , r_H , and a are the radius of the shell, the horizon length where $H(r)$ vanishes, and the horizon length in the de Sitter space, respectively. The ratios of various pairs are plotted. Circles, squares, and diamonds correspond to data points obtained.

smooth across the horizon. First we illustrate the construction with de Sitter space, and then consider the more general case which is applied to the shell solution.

The $R^1 \times S^3$ metric of the de Sitter space is given by

$$ds^2 = a^2 \left[-d\tau^2 + \cosh^2 \tau \left(d\chi^2 + \sin^2 \chi d\Omega^2 \right) \right]. \quad (3.30)$$

One may regard the de Sitter space as a hypersurface in the five-dimensional Minkowski spacetime constrained by the condition

$$y_1^2 + y_2^2 + y_3^2 + y_4^2 = a^2 + y_0^2. \quad (3.31)$$

The metric (3.30) and hypersurface (3.31) cover the entire de Sitter space, whereas the static metric covers only half of the space. Furthermore, the static metric has a

coordinate singularity at $r = a$.

The relationship among these coordinate systems are easily found. The S^3 metric (3.30) can be transformed to a metric conformal to the static Einstein universe,

$$\begin{aligned} ds^2 &= \frac{a^2}{\cos^2 \eta} \left[-d\eta^2 + d\chi^2 + \sin^2 \chi d\Omega^2 \right] \\ \eta &= \frac{\pi}{2} - 2 \tan^{-1}(e^{-\tau}), \quad -\frac{\pi}{2} \leq \eta \leq \frac{\pi}{2}. \end{aligned} \quad (3.32)$$

Suppressing S^2 , or θ and ϕ variables, one can map the whole de Sitter space to a square region in the χ - η coordinates. Null geodesics are given by straight lines at 45 degree angles.

The static and hypersurface coordinates are related by

$$\begin{aligned} y_0 &= \begin{cases} \sqrt{a^2 - r^2} \sinh \frac{t}{a} & \text{for } r < a \\ \sqrt{r^2 - a^2} \cosh \frac{t}{a} & \text{for } r > a \end{cases} \\ y_1 &= r \cos \theta \\ y_2 &= r \sin \theta \cos \phi \\ y_3 &= r \sin \theta \sin \phi \\ y_4 &= \begin{cases} \sqrt{a^2 - r^2} \cosh \frac{t}{a} & \text{for } r < a \\ \sqrt{r^2 - a^2} \sinh \frac{t}{a} & \text{for } r > a \end{cases} \end{aligned} \quad (3.33)$$

Similarly, Eqs. (3.31) and (3.32) are related by

$$\begin{aligned} y_0 &= a \tan \eta \\ y_1 &= a \sec \eta \sin \chi \cos \theta \\ y_2 &= a \sec \eta \sin \chi \sin \theta \cos \phi \\ y_3 &= a \sec \eta \sin \chi \sin \theta \sin \phi \\ y_4 &= a \sec \eta \cos \chi. \end{aligned} \quad (3.34)$$

The region inside the cosmological horizon ($r < a$, $-\infty < t < \infty$) in the static metric corresponds to the left quadrant in the conformal metric ($0 \leq \chi \leq \frac{1}{2}\pi$, $|\eta| < \pi/2 - \chi$) with the relations

$$\begin{aligned}\frac{r}{a} &= \frac{\sin \chi}{\cos \eta} \\ \frac{t}{a} &= \frac{1}{2} \ln \frac{\cos \chi + \sin \eta}{\cos \chi - \sin \eta}.\end{aligned}\quad (3.35)$$

Similarly, the region outside the cosmological horizon ($r > a$, $-\infty < t < \infty$) in the static metric corresponds to the upper quadrant in the conformal metric ($0 \leq \chi \leq \pi$, $|\eta| > \chi - \frac{1}{2}\pi$) with the relations

$$\begin{aligned}\frac{r}{a} &= \frac{\sin \chi}{\cos \eta} \\ \frac{t}{a} &= \frac{1}{2} \ln \frac{\sin \eta + \cos \chi}{\sin \eta - \cos \chi}.\end{aligned}\quad (3.36)$$

See figure 3.11.

For the general static metric given by Eq. (3.2), with $H = H(r)$ and $p = p(r)$, the construction of the conformal coordinates analogous to Eq. (3.32) proceeds as follows. We suppose that $H(r)$ has a single zero at r_H whereas $p(r) > 0$. The new radial coordinate is defined by

$$r_*(r) = \begin{cases} \int_0^r dr' \frac{p(r')}{H(r')} & \text{for } r < r_H \\ \int_\infty^r dr' \frac{p(r')}{H(r')} & \text{for } r > r_H. \end{cases}\quad (3.37)$$

It has a logarithmic singularity at r_H , diverging there as $r_* \sim -\frac{1}{2}b \ln |r - r_H|$ where $b = -2p(r_H)/H'(r_H) > 0$. New coordinates are introduced by

$$\begin{aligned}\tan u &= +e^{+t/b} e^{-r_*/b} \\ \tan v &= \mp e^{-t/b} e^{-r_*/b}.\end{aligned}\quad (3.38)$$

$$= \frac{H}{2p^2} \left(1 \pm \cosh \frac{2r_*}{b}\right) \quad \text{for } \begin{cases} r \leq r_H \\ r \geq r_H \end{cases} . \quad (3.39)$$

The static metric covers the region interior to the bounding lines $u = 0$, $u + v = \frac{1}{2}\pi$, and $u - v = \frac{1}{2}\pi$. The horizon in the static metric, $r = r_H$, corresponds to the single point $u = v = 0$. The function F is non-vanishing and finite there as $e^{2r_*/b} \sim 1/|r - r_H|$. In the u - v coordinates the metric is regular on $u = 0$ so that the extension to the region $u < 0$ can be made, whereas the static metric covers only half of the space.

Applied to the de Sitter space we find

$$r_H = b = a , \quad e^{-r_*/b} = \left| \frac{a - r}{a + r} \right|^{1/2} , \quad F = 1 , \quad (3.40)$$

and the metric (3.32) is recovered by

$$\eta = u + v , \quad \chi = v - u + \frac{\pi}{2} . \quad (3.41)$$

The shell solution found in the preceding sections can be extended to the entire space-time. In the region III ($R_2 < r$) defined in the static metric $H(r)$ is given by Eq. (3.26), and the location of the horizon is determined by $H(r_H) = 0$. In region III, $\delta\phi(r)$ is very small so that its equation of motion can be linearized. We divide region III into two; region IIIa ($R_2 < r < 2r_H - R_2$) and region IIIb ($r > 2r_H - R_2$). In region IIIa, $H(r)$ can be approximated by

$$H(r) \sim A \left(1 - \frac{r^2}{r_H^2}\right) , \quad (3.42)$$

where

$$A = \frac{1}{2} \left(\frac{3r_H^2}{a^2} - 1 \right) . \quad (3.43)$$

The coefficient A has been chosen such that both Eqs. (3.26) and (3.42) have the same slope $H'(r_H)$ at the horizon. In the examples described in Sec. 3.3, errors caused by Eq. (3.42) are less than 15% in region IIIa. Now we write the linearized version of Eq. (3.11) in terms of $y = 1 - (r^2/r_H^2)$,

$$\left\{ y(1-y) \frac{d^2}{dy^2} + \left(1 - \frac{5}{2}y\right) \frac{d}{dy} - \left(\tilde{\kappa}^2 + \frac{9}{16}\right) \right\} \delta\phi = 0$$

$$A\left(\tilde{\kappa}^2 + \frac{9}{16}\right) = \kappa^2 + \frac{9}{16} = \frac{1}{4}\omega^2 a^2. \quad (3.44)$$

Since $\delta\phi(r)$ must be regular at $r = r_H$ ($y = 0$), the solution is

$$\delta\phi(r) = \delta\phi(r_H) \cdot F\left(\frac{3}{4} + i\tilde{\kappa}, \frac{3}{4} - i\tilde{\kappa}, 1; y\right). \quad (3.45)$$

The normalization $\delta\phi(r_H)$ must be such that $\delta\phi(r)$ matches at $r = R_2$ with the value determined by numerical integration in region II. Essentially $\delta\phi(r)$ decreases exponentially when $R_2 < r < r_H$.

Near $r = R_2$ the hypergeometric function behaves as

$$F\left(\frac{3}{4} + i\tilde{\kappa}, \frac{3}{4} - i\tilde{\kappa}, 1; y\right) \sim \frac{1}{2\sqrt{\pi\tilde{\kappa}}} y^{-1/4} (1-y)^{-1/2} \exp\left\{2\tilde{\kappa} \sin^{-1} \sqrt{y}\right\} \quad (3.46)$$

so that

$$\frac{\delta\phi'(r)}{\delta\phi(r)} = -\frac{2r}{r_H^2} \cdot \frac{\tilde{\kappa}}{\sqrt{y(1-y)}}. \quad (3.47)$$

The value of the right-hand side of Eq. (3.47) at $r = R_2$ can be compared with the value obtained by direct numerical integration in region II. In one example with $f/m_P = 2 \times 10^{-3}$, $\Delta f/f = 2 \times 10^{-3}$, $\lambda = 0.01$, $R_2 = 1.765 \times 10^7$, $a = 2.365 \times 10^7$, $r_H = 1.985 \times 10^7$, $\kappa = 3344$, and $\tilde{\kappa} = 4481$. The numerical value for $\delta\phi'(R_2)/\delta\phi(R_2)$ is -0.000848 , whereas the value from Eq. (3.47) is -0.000985 . With the uncertainty in the value of $\tilde{\kappa}$ caused by the approximation (3.42) taken into account, one may conclude that the agreement is rather good. To gauge the difficulty of determining the solution numerically for all values of r , we note that $\delta\phi(r_H) \sim 10^{-1850} \cdot \delta\phi(R_2)$.

The most important observation is that the solution $\phi(r)$ is regular at the horizon, $r = r_H$, though the static metric (t, r, θ, ϕ) is not: $r = r_H$ in the static metric is a coordinate singularity. As seen above, $r = r_H$ corresponds to $u = v = 0$ in the conformal metric (3.39) which is non-singular. Near the horizon $\tan u \tan v \sim r - r_H$ so that

$$\phi = f_1 + \delta\phi(r_H) \left\{ 1 - \frac{2}{r_H} \left(\tilde{\kappa}^2 + \frac{9}{16} \right) uv + \dots \right\}. \quad (3.48)$$

Furthermore, as $\tan u \tan v = e^{-2r_*(r)/b}$, the static solution $\phi(u, v)$ depends only on $\tan u \tan v$ in the entire space-time. This implies that

$$\phi(-u, -v) = \phi(u, v). \quad (3.49)$$

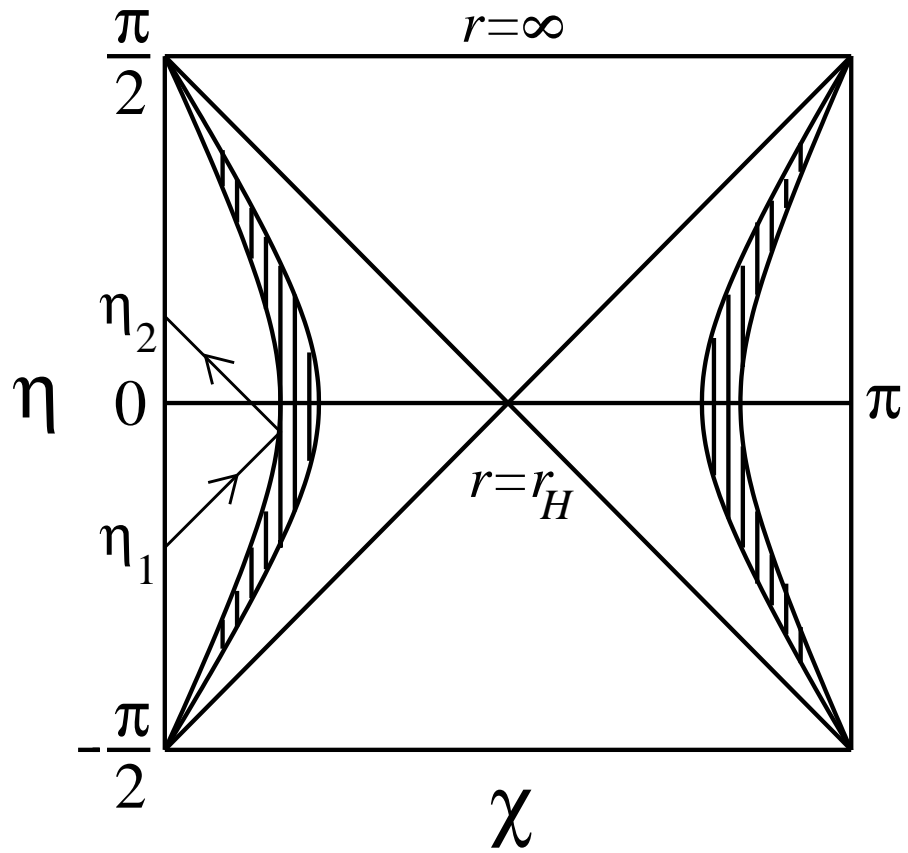


Figure 3.12: Global structure of the shell solution in the conformal coordinates. The mirror image appears in the other hemisphere.

In the η - χ coordinates (S^3 metric) defined by Eq. (3.41)

$$\phi(\eta, \chi) = \phi(-\eta, \pi - \chi) = \phi(\eta, \pi - \chi) . \quad (3.50)$$

This relation shows that there is a mirror image of the shell structure in the other hemisphere in the S^3 metric. See figure 3.12. The shaded regions in the figure represent the shells. The size of the shells is invariant, as is obvious in the static coordinates. In the S^3 or conformal metric an observer at the center ($\chi = 0$ or π) sends a light signal toward the shell. Another observer at the shell, upon receiving the signal from the center, sent a signal back to the observer at the center. The total elapsed time, in terms of the proper time of the observer at the center $a\tau$ where τ is

related to η by Eq. (3.32) at $\chi = 0$, is $a \ln(a + R)/(a - R)$, independent of when the signal is emitted initially, as straightforward manipulations show.

Finally, in the region outside the horizon in the static metric, or in the upper or lower quadrant in the Penrose diagram, $\delta\phi(r)$ decays as $r^{-3/2}$. The proof goes as follows. For $r \gg r_H$, $H \sim 1 - (r^2/a^2)$, so that $\delta\phi(r)$ satisfies Eq. (3.20). Hence it is a linear combination of $u_1 = F(\frac{3}{4} + i\kappa, \frac{3}{4} - i\kappa, \frac{3}{2}; z)$ and $u_2 = z^{-1/2}F(\frac{1}{4} + i\kappa, \frac{1}{4} - i\kappa, \frac{1}{2}; z)$.

These can be written as

$$\begin{aligned} \begin{bmatrix} u_1 \\ u_2 \end{bmatrix} &= \begin{bmatrix} \frac{1}{2}\Gamma(\frac{3}{4} - i\kappa)^{-2} \\ \Gamma(\frac{1}{4} - i\kappa)^{-2} \end{bmatrix} \frac{\sqrt{\pi}\Gamma(-2i\kappa)}{(-z)^{(3/4)+i\kappa}} F\left(\frac{3}{4} + i\kappa, \frac{1}{4} + i\kappa, 1 + 2i\kappa; \frac{1}{z}\right) \\ &+ \begin{bmatrix} \frac{1}{2}\Gamma(\frac{3}{4} + i\kappa)^{-2} \\ \Gamma(\frac{1}{4} + i\kappa)^{-2} \end{bmatrix} \frac{\sqrt{\pi}\Gamma(+2i\kappa)}{(-z)^{(3/4)-i\kappa}} F\left(\frac{3}{4} - i\kappa, \frac{1}{4} - i\kappa, 1 - 2i\kappa; \frac{1}{z}\right). \end{aligned} \quad (3.51)$$

From this one can write

$$\phi \sim f_1 + A \left(\frac{a}{r}\right)^{3/2} \sin\left(2\kappa \ln \frac{r}{a} + \delta\right) \quad (3.52)$$

when $r \gg r_H$.

3.4 False Vacuum Decay

If the region inside the shell is in a false vacuum state one should consider its quantum decay to the true vacuum state. The lifetime of the false vacuum may be determined semiclassically using the methods of Coleman *et al.* without [57] or with [19] gravity taken into account. The rate per unit volume for making a transition from the false vacuum to the true vacuum is expressed as

$$\frac{\Gamma}{V} = Ae^{-B/\hbar}[1 + \mathcal{O}(\hbar)] \quad (3.53)$$

where Planck's constant has been used here to emphasize the semiclassical nature of the tunneling rate. For the potential being used in this paper we find the $O(4)$, Euclidean space, bounce action (neglecting gravity) to be

$$B_0 = \frac{36\pi^2}{\lambda} \left(\frac{f}{\Delta f}\right)^3 \quad (3.54)$$

where the radius of the critical size bubble which nucleates the transition is

$$\rho_c = \frac{3}{\Delta f} \sqrt{\frac{2}{\lambda}}. \quad (3.55)$$

For any sensible estimate of the coefficient A the lifetime of the false vacuum will exceed the present age of the universe when the condition

$$\lambda \left(\frac{\Delta f}{f} \right)^3 < 1 \quad (3.56)$$

is satisfied. This calculation is based on the thin wall approximation, which is valid when the critical radius is large compared to the coherence length of the potential, namely, $1/\sqrt{|V''|}$. This condition translates into

$$\Delta f \ll 6f. \quad (3.57)$$

With gravity included the bounce action is

$$B = \frac{B_0}{[1 + (\rho_c/2R)^2]^2}. \quad (3.58)$$

Gravitational effects are negligible when $\rho_c < R$. When this condition is not fulfilled the shell radius is too small to accommodate even a single nucleation bubble and therefore nucleation is further suppressed.

Chapter 4

Summary

The increasing energy of the gamma rays and neutrinos emitted by exploding microscopic black holes and the disappearance of such point sources in a certain period of time are unique characteristics because astrophysical sources normally cool at late times. This would directly reflect the increasing Hawking temperature as the black hole explodes and disappears. We should emphasize in particular the usefulness of distinguishing between the electron and muon-type neutrinos and the tau-type ones. The latter are much less likely to be produced by high energy cosmic rays. If the rate density of exploding microscopic black holes in our vicinity is anywhere close to the current limit based on gamma rays, it should be possible to observe them with present and planned large astrophysical neutrino detectors. Observation of high energy neutrinos, especially in conjunction with high energy gamma rays, may provide a window on physics well beyond the TeV scale. The results of this research will bear directly on the observational program on astroparticle physics that involves gamma ray detectors such as Milagro and neutrino detectors such as AMANDA and IceCube, as well as detectors for ultra high energy cosmic rays, such as Auger, to observe and detect possible signals of microscopic black holes.

Still, there is much work to be done in determining whether the matter surrounding a black hole can reach and maintain thermal equilibrium. The previous calculations should be improved by including the effect of gravity, which was neglected in the

calculation, which may lead to corrections of up to 10%. The equation of state should be improved, and the viscosities computed using the relaxation times for self-consistency of the transition from viscous fluid flow to free streaming. Also, there should be a more fundamental investigation of the relaxation times starting from the microscopic interactions. Our next step is to calculate the flux of other particles such as antiprotons and positrons radiated by microscopic black holes in order to help the observation of these black holes. Positrons and antiprotons are expected to freeze out at a temperature around 100 MeV. Another worthwhile project is to carry out cascade simulations of the spherically expanding matter around the microscopic black hole at a level of sophistication comparable to that of high energy heavy ion collisions. This project is much more complicated than the cascade simulation in heavy ion collision, though, because we need to deal with a much wider range of energies and particles involved in exploding microscopic black holes.

The study of microscopic black holes might well lead to great advancements in fundamental physics. Because the highest temperatures in the universe exist in the vicinity of microscopic black holes, matter at extremely high temperatures can be studied, and physics beyond the four dimensional Standard Model and above the electroweak scale can be tested. In addition, because it is believed that baryon number is violated at high temperatures, the study of microscopic black holes could possibly answer the question of why our universe became matter-dominated. Because microscopic black holes explode, they are an ideal model for studying the Big Bang and the birth of our universe. Finally, the study of microscopic black holes will help us to determine whether they are the source of the highest energy cosmic rays. The origin of these cosmic rays is still one of the biggest mysteries today. Observation and experimental detection of microscopic black holes with satellite and ground based neutrino observatories may lead to a novel paradigm for understanding new sources of the highest energy cosmic and gamma rays in the Universe. Observation and experimental detection of microscopic black holes will be one of the great challenges in the new millennium.

In the second part of this thesis we have reported the discovery of shell-like solutions to the combined field equations of gravity and a scalar field with a double-minima potential. These solutions exist in a space that is asymptotically de Sitter. The range of parameters which allow such solutions are very broad. If anything like these structures exist in nature they most likely would have been created in the early universe and are therefore cosmological. We know of no other way to produce them.

To make matters interesting, let us suppose that the cosmological constant suggested by recent observations of distant Type Ia supernovae [58] arises from the universe actually being in a false vacuum state. A best fit to all cosmological data [59] reveals that the present energy density of the universe has the critical value of $\epsilon_c = 3H_0^2/8\pi G$, with one-third of it consisting of ordinary matter and two-thirds of it contributed by the cosmological constant. Suppose that the cosmological constant arises from a potential of the form we have been analyzing. Then with a present value of the Hubble constant of $H_0 = 65 \text{ km/s}\cdot\text{Mpc}$ we find that

$$a = \sqrt{\frac{3}{2}} \frac{1}{H_0} = 1.7 \times 10^{26} \text{ m} \quad (4.1)$$

and so

$$\left(\lambda f^3 \Delta f\right)^{1/4} = 2.4 \times 10^{-3} \text{ eV} . \quad (4.2)$$

This is a constraint on the parameters of the potential, λ , f and Δf . Although they cannot be determined individually from this data, we can place limits on them such that a shell structure might arise. Recalling (3.29) we find

$$\begin{aligned} f &< 30\lambda^{-1/6} \text{ MeV} , \\ w &> 6.3\lambda^{-1/3} \text{ fm} . \end{aligned} \quad (4.3)$$

This is pure speculation of course. A cosmological constant, if it exists, may have its origins elsewhere. But if it does arise from a false vacuum, a variety of questions immediately present themselves. Is ϕ a new field, not present in the standard model of particle physics, whose only purpose is this? Where does the energy scale of 2.4 meV come from? Why should $V[\phi]$ have a global minimum of 0, especially when

quantum mechanical fluctuations are taken into account? To these questions we have no answers.

Appendix A

Numerical Calculations

In the numerical calculations of Eqs. (2.11), (2.13), (2.14), (2.17) and (2.18), we use the unitless variables $t = T/T_H$ and $x = r/r_s$. In terms of these unitless variables, we can rewrite the equations as

$$s_t = \frac{4\pi^2}{90} t^3 \begin{cases} 101.5, & t_{EW} \leq t, \\ 56.5 + 45 e^{-(t_{EW}-t)/t}, & t_{QCD} \leq t < t_{EW}, \\ 2 + 3.5 e^{-\frac{m_e/T_h}{t}} + 27.25 e^{-(t_{QCD}-t)/t}, & t < t_{QCD}, \end{cases} \quad (\text{A.1})$$

$$\eta_t = \frac{82.5}{\frac{4}{3} \frac{\pi^2}{30} 101.5} s_t, \quad (\text{A.2})$$

$$\xi_t = 10^{-4} \eta_t, \quad (\text{A.3})$$

$$\gamma_t s_t - \frac{4}{3} (4\pi) \eta_t \gamma u \left(\frac{du}{dx} - \frac{u}{x} \right) - (4\pi) \zeta_t \gamma u \left(\frac{du}{dx} + \frac{2u}{x} \right) = \frac{4\pi L/T_H^2}{x^2}, \quad (\text{A.4})$$

and

$$\frac{d}{dx} (x^2 u s_t) = 4\pi \frac{x^2}{t} \left[\frac{8}{9} \eta_t \left(\frac{du}{dx} - \frac{u}{x} \right)^2 + \zeta \left(\frac{du}{dx} + \frac{2u}{x} \right)^2 \right] \quad (\text{A.5})$$

where $s_t = s/T_H^3$, $\eta_t = \eta/T_H^3$ and $\xi_t = \xi/T_H^3$. Here $L = 64\pi^2 \alpha_h T_H^2$ where $\alpha_h = 4.43 \times 10^{-4}$ includes neutrinos and gravitons. In the case of calculating gamma ray spectra, gravitons and neutrinos should be ignored since gravitons never contribute to the fluid and neutrinos freeze-out at a temperature around 100 GeV. In the case of calculating neutrino spectra, only gravitons need to be ignored for direct neutrinos which freeze-out at 100 GeV. For the indirect neutrinos both gravitons and neutrinos

need to be ignored. In our calculations these small numerical differences in α_h have been neglected.

In order to find the asymptotic behavior of u and t in the limit where $x \rightarrow 0$, we look for a behavior of the form $u = Ax^\alpha$ and $t = Bx^\beta$ with $\gamma \approx 1$. For black holes with temperatures greater than $T_{EW} = 100$ GeV, we can write the equation of state as

$$s_t = \frac{4}{3}at^3, \quad \eta_t = b_S t^3 \quad \text{and} \quad \xi_t = b_B t^3, \quad (\text{A.6})$$

where $a = \frac{\pi^2}{30}101.5$, $b_S = 82.5$ and $b_B = b_S \times 10^{-4}$. The best solution in the small x limit is

$$\begin{aligned} \alpha &= \frac{2}{5}, \\ \beta &= -\frac{3}{5}, \\ A &= \frac{5a}{\pi(8b_S + 144b_B)} \left\{ \frac{4\pi L}{T_H^2} \right. \\ &\quad \times \left. \left(\frac{4}{3}a + 4\pi\left(\frac{4}{5}b_S - \frac{12}{5}b_B\right)\frac{5a}{\pi(8b_S + 144b_B)} \right)^{-1} \left(\frac{5a}{\pi(8b_S + 144b_B)} \right)^{-1} \right\}^{1/5}, \end{aligned}$$

and

$$\begin{aligned} B &= \left\{ \frac{4\pi L}{T_H^2} \left(\frac{4}{3}a + 4\pi\left(\frac{4}{5}b_S - \frac{12}{5}b_B\right)\frac{5a}{\pi(8b_S + 144b_B)} \right)^{-1} \right. \\ &\quad \times \left. \left(\frac{5a}{\pi(8b_S + 144b_B)} \right)^{-1} \right\}^{1/5}. \end{aligned} \quad (\text{A.7})$$

Typical numerical values for u and t in this limit are $u = 0.105715x^{2/5}$ and $t = 1.31521x^{-3/5}$.

In order to find the asymptotic behavior of u and t in the limit where $x \rightarrow \infty$, we again look for solutions of the form $u = Ax^\alpha$ and $t = Bx^\beta$ with $\gamma \approx u$. In this limit the equation of state can be written in the same form as in Eqn. (A.6), where $a = \frac{\pi^2}{30}2$, $b_S = 82.5\frac{2}{101.5}$ and $b_B = b_S \times 10^{-4}$. The asymptotic solution in the large x

limit is

$$\begin{aligned}\alpha &= \frac{1}{3}, \\ \beta &= -\frac{2}{3}, \\ A &= \frac{9a}{\pi(32b_S + 441b_B)} \left\{ \frac{4\pi L}{T_H^2} \right. \\ &\quad \times \left. \left(\frac{4}{3}a + 4\pi\left(\frac{8}{9}b_S - \frac{7}{3}b_B\right)\frac{9a}{\pi(32b_S + 441b_B)} \right)^{-1} \left(\frac{9a}{\pi(32b_S + 441b_B)} \right)^{-2} \right\}^{1/6},\end{aligned}$$

and

$$\begin{aligned}B &= \left\{ \frac{4\pi L}{T_H^2} \left(\frac{4}{3}a + 4\pi\left(\frac{8}{9}b_S - \frac{7}{3}b_B\right)\frac{9a}{\pi(32b_S + 441b_B)} \right)^{-1} \right. \\ &\quad \times \left. \left(\frac{9a}{\pi(32b_S + 441b_B)} \right)^{-2} \right\}^{1/6}.\end{aligned}\tag{A.8}$$

The typical numerical values for u and t in this limit are $u = 0.184460x^{1/3}$ and $t = 5.09763x^{-2/3}$.

To solve Eqs. (A.1)-(A.5) we use a 4th order vector Runge-Katta method. In our program we apply a shooting type method to find the numerical solution over a wide range of x such that u has the correct asymptotic behavior when $x \rightarrow \infty$. In the program this is done by comparing the numerical solution for u to its correct asymptotic behavior at large x . The initial value of t at $x = 0.1$ is fixed and the initial value of u at $x = 0.1$ is changed by the program until the correct solution is obtained. In order to check the validity of the numerical solution, we calculate $4\pi r^2 T^{0r}/L$ using finite difference method. The result, which is very close to 1 over a wide range of x , is plotted in figure A.1 for a black hole temperature of 10 TeV. For more information see the numerical recipes `mbhwind.c` and `subroutinewind.h` attached to this thesis.

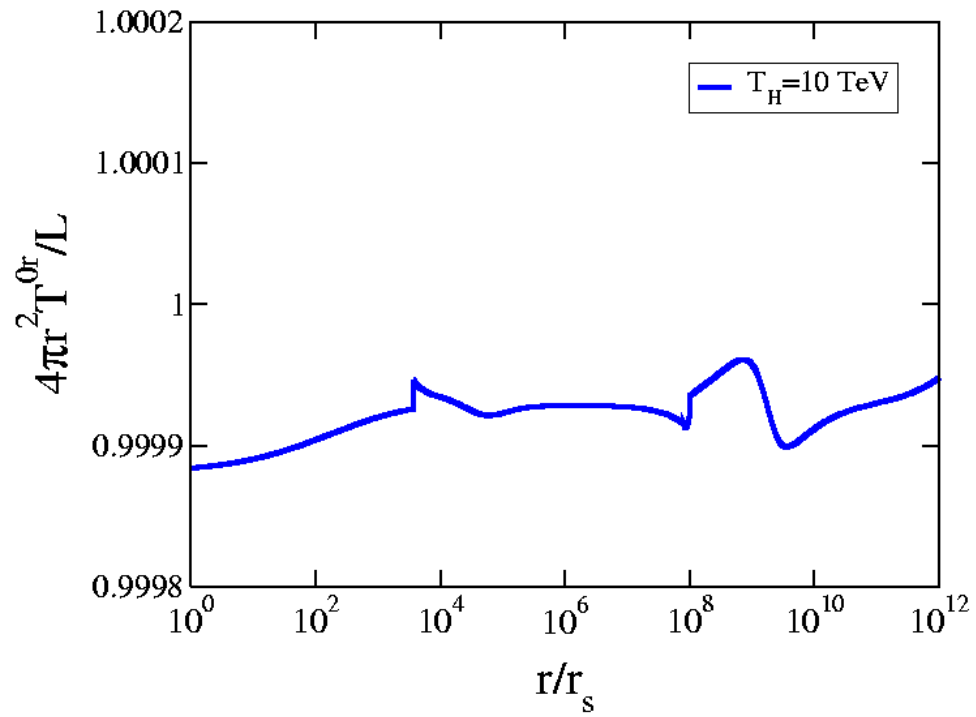


Figure A.1: $4\pi r^2 T^{0r}/L$ as a function of r/r_s for a black hole temperature of 10 TeV. The curve begins at r_s and terminates when the local temperature reaches $T = m_e$.

References

- [1] R. Daghigh and J. Kapusta, Phys. Rev. D **65**, 064028 (2002);
- [2] R. G. Daghigh, J. I. Kapusta, astro-ph/021157 (2002);
- [3] Y. Hosotani, T. Nakajima, R. G. Daghighg and J. I. Kapusta, r-qc/0112079 (2001);
- [4] S. W. Hawking, Nature (London) **248**, 30 (1974); Commun. Math. Phys. **43**, 199 (1975).
- [5] B. J. Carr and J. H. MacGibbon, Phys. Rep. **307**, 141 (1998).
- [6] Particle Data Group: *Review of Particle Physics*, Eur. Phys. J. **C3**, 1 (1998).
- [7] J. H. MacGibbon and B. R. Webber, Phys. Rev. D **41**, 3052 (1990).
- [8] J. H. MacGibbon and B. J. Carr, Astrophys. J. **371**, 447 (1991).
- [9] A. F. Heckler, Phys. Rev. Lett. **78**, 3430 (1997).
- [10] A. F. Heckler, Phys. Rev. D **55**, 480 (1997).
- [11] J. Cline, M. Mostoslavsky, and G. Servant, Phys. Rev. D **59**, 063009 (1999).
- [12] J. I. Kapusta, Phys. Rev. Lett. **86**, 1670 (2001).
- [13] L. P. Csernai, *Introduction to Relativistic Heavy Ion Collisions* (John Wiley & Sons, Chichester, England, 1994)
- [14] J. Bjoraker and Y. Hosotani, Phys. Rev. Lett. **84**, 1853 (2000);
J. Bjoraker and Y. Hosotani, Phys. Rev. D **62**, 43513 (2000);
Y. Hosotani, gr-qc/0103069, to appear in J. Math. Phys.
- [15] E. Radu, gr-qc/0109015.
- [16] D. V. Gal'tsov, hep-th/0112038.
- [17] S. Deser, Phys. Lett. B **64**, 463 (1976).

- [18] R. Bartnik and J. McKinnon, Phys. Rev. Lett. **61**, 141 (1988);
H. Künzle and A. Masood-ul-Alam, J. Math. Phys. **31**, 928 (1990);
J. A. Smoller, A. G. Wasserman, S. T. Yau and J. B. McLeod, Comm. Math. Phys. **143**, 115 (1991);
J. A. Smoller and A. G. Wasserman,, *ibid.* **151**, 303 (1993);
M. S. Volkov, N. Straumann, G. Lavrelashvili, M. Huesler and O. Brodbeck, Phys. Rev. D **54**, 7243 (1996).
- [19] S. Coleman and F. De Luccia, Phys. Rev. D **21**, 3305 (1980).
- [20] R. G. Daghigh, J. I. Kapusta, and Y. Hosotani, gr-qc/0008006 (2000);
- [21] D. V. Gal'tsov and J. P. S. Lemos, Class. Quant. Grav. **18**, 1715 (2001).
- [22] K. A. Bronnikov, Phys. Rev. D**64**, 064013 (2001);
K. A. Bronnikov and G. N. Shikin, gr-qc/0109027.
- [23] K. Maeda, K. Sato, M. Sasaki and H. Kodama, Phys. Lett. **B108**, 98 (1982);
K. Sato, H. Kodama, M. Sasaki and K. Maeda, *ibid.* 103 (1982).
- [24] K. Sato, M. Sasaki, H. Kodama, and K. Maeda, Prog. Theoret. Phys. **65**, 1443 (1981);
H. Kodama, M. Sasaki, K. Sato, and K. Maeda, *ibid.* **66**, 2052 (1981);
H. Kodama, M. Sasaki, and K. Sato, *ibid.* **68**, 1979 (1982);
K. Sato, *ibid.* **66**, 2287 (1981).
- [25] S. K. Blau, E. I. Guendelman and A. H. Guth, Phys. Rev. D **35**, 1747 (1987);
E. Fahri, A. H. Guth, and J. Guven, Nucl. Phys. **B339**, 417 (1990).
- [26] A preliminary result has been reported in
Y. Hosotani, Soryushiron Kenkyu **103**, E91 (2001); hep-th/0104006.
- [27] I. G. Dymnikova, Phys. Lett. **B472**, 33 (2000); gr-qc/0010016.
- [28] D. N. Page, Phys. Rev. D **13**, 198 (1976); *ibid.* **14**, 3260 (1976); **16**, 2402 (1977).
- [29] N. Sanchez, Phys. Rev. D **18**, 1030 (1978); the coefficient was extracted from figure 5 of this paper to within about 5% accuracy.
- [30] C. W. Misner, K. S. Thorne, and J. A. Wheeler, *Gravitation* (W. H. Freeman and Company, San Francisco, 1973).
- [31] J. I. Kapusta and K. A. Olive, Phys. Lett. **B209**, 295 (1988).

- [32] M. E. Carrington and J. I. Kapusta, Phys. Rev. D **47**, 5304 (1993).
- [33] G. Baym, H. Monien, C. J. Pethick, and D. G. Ravenhall, Phys. Rev. Lett. **64**, 1867 (1990).
- [34] P. Arnold, G. D. Moore, and L. G. Yaffe, J. High Energy Phys. **11**, 001 (2000).
- [35] K. Kinder-Geiger, Phys. Rep. **258**, 237 (1995).
- [36] S.M.H. Wong, Phys. Rev. C **54**, 2588 (1996).
- [37] J. I. Kapusta, *Finite Temperature Field Theory* (Cambridge University Press, Cambridge, England, 1989).
- [38] M. Prakash, M. Prakash, R. Venugopalan and G. Welke, Phys. Rep. **227**, 321 (1993).
- [39] J. M. Jauch and F. Rohrlich, *The Theory of Electrons and Photons*, (Springer-Verlag, New York, 1975).
- [40] E. Haug, Z. Naturforsch. Teil A **30**, 1099 (1975).
- [41] R. Cutler and D. Sivers, Phys. Rev. D **17**, 196 (1978).
- [42] S. Weinberg, *Gravitation and Cosmology*, (John Wiley & Sons, New York, 1972), p. 57.
- [43] F. Halzen, E. Zas, J. H. MacGibbon and T. C. Weekes, Nature (London) **353**, 807 (1991).
- [44] R. J. Gould and G. Schreder, Phys. Rev. Lett. **16**, 252 (1966).
- [45] D. N. Page and S. W. Hawking, Astrophys. J. **206**, 1 (1976).
- [46] E. L. Wright, Astrophys. J. **459**, 487 (1996).
- [47] D. B. Cline, Astrophys. J. **501**, L1 (1998).
- [48] D. E. Alexandreas, *et al.*, Phys. Rev. Lett. **71**, 2524 (1993).
- [49] J. H. MacGibbon, *ibid.* **44**, 376 (1991).
- [50] F. Halzen, B. Keszthelyi and E. Zas, Phys. Rev. D **52**, 3239 (1995).
- [51] W. G. Unruh, Phys. Rev. D **14**, 3251 (1976).
- [52] M. S. Volkov, N. Straumann, G. Lavrelashvili, M. Heusler, and O. Brodbeck, Phys. Rev. D **54**, 7243 (1996).
- [53] C. Lechner, S. Husa, and P.C. Aichelburg, Phys. Rev. D **62**, 044047 (2000).

- [54] Bateman Manuscript Project, vol. 1. §2.3.2, page 77.
- [55] M. D. Kruskal, Phys. Rev. **119**, 1743 (1960);
G. Szekeres, Publ. Mat. Debrecen **7**, 285 (1960).
- [56] G. W. Gibbons and S. W. Hawking, Phys. Rev. D **15**, 2738 (1977).
- [57] S. Coleman, Phys. Rev. D **15**, 2929 (1977); **16**, 1248(E) (1977);
C. G. Callan and S. Coleman, *ibid.* **16**, 1762 (1977).
- [58] A. G. Riess *et al.*, Astron. J. **116**, 1009 (1998);
P. M. Garnavich *et al.*, Astrophys. J. **509**, 74 (1998);
S. Perlmutter *et al.*, Astrophys. J. **517**, 565 (1999).
- [59] N. A. Bahcall, J. P. Ostriker, S. Perlmutter and P. J. Steinhardt, Science **284**, 1481 (1999).